Title
Using X-ray Thomson Scattering to Measure Plasma Conditions in Warm Dense Matter Experiments on the OMEGA Laser

Author
Saunders, Alison Marie-Anne

Publication Date
2018

Peer reviewed|Thesis/dissertation

Using X-ray Thomson Scattering to Measure Plasma Conditions in Warm Dense Matter Experiments on the OMEGA Laser

by

Alison Marie-Anne Saunders

A dissertation submitted in partial satisfaction of the
requirements for the degree of
Doctor of Philosophy

in

Physics

in the

Graduate Division

of the

University of California, Berkeley

Committee in charge:

Professor Roger W. Falcone, Co-chair
Doctor Tilo Döppner, Co-chair
Professor Barbara Jacak
Professor Raymond Jeanloz

Spring 2018

Using X-ray Thomson Scattering to Measure Plasma Conditions in Warm Dense Matter Experiments on the OMEGA Laser

Alison Marie-Anne Saunders

Abstract

Using X-ray Thomson Scattering to Measure Plasma Conditions in Warm Dense Matter Experiments on the OMEGA Laser

by

Alison Marie-Anne Saunders

Doctor of Philosophy in Physics

University of California, Berkeley

Professor Roger W. Falcone, Co-chair

Doctor Tilo Döppner, Co-chair

High energy density physics (HEDP) is an emerging field that seeks to investigate the properties of matter at extreme conditions. High energy density conditions occur in materials with pressures exceeding 1 Mbar, or pressures that exceed Earth's atmospheric pressure by a factor of more than a million. A regime of HEDP of particular interest is warm dense matter (WDM) physics, which describes the behavior of materials at near solid densities and 10's of eV temperatures. WDM occurs in astrophysical objects, such as giant planets and brown dwarfs, and is also generated in inertial confinement fusion (ICF) experiments. X-ray Thomson scattering (XRTS) offers a powerful tool to probe the equation of state of WDM. XRTS spectra consist of two components: elastically scattered photons with the frequency of the original x-ray source and inelastically scattered photons that are down-shifted in frequency. The Compton-shifted profile of inelastically scattered x-rays can be analyzed to return the sample's electron density and electron temperature. The ratio of elastically to inelastically scattered x-rays relates to the number of tightly bound versus free electrons, and thus reflects the ionization state.

This thesis discusses the results of XRTS experiments on WDM performed at the OMEGA Laser facility. The first experiment presents and discusses XRTS results from 1 mm diamond spheres. The scattering spectra show evidence of higher ionization than predicted by several commonly-applied ionization models. A second experiment analyzed the contributions to elastic scattering from a small argon impurity in imploding beryllium capsules. The experiment found that less than 1 at.% of argon significantly affects the elastic scattering signal strength, and concluded that impurities in a sample should be considered before drawing conclusions from elastic scattering signals. The final experiment uses XRTS to measure the electron temperature and ionization state in isochorically heated materials used in ion stopping power experiments. The results from these experiments demonstrate the power of XRTS to measure ionization in WDM to benchmark theoretical modeling.

To Austin

Research in high pressure physics can cause stress and strain, but you help me remember where life's true value lies. Thank you for reminding me that sparkly diamonds only exist because they, too, were once under pressure.

Contents

List of Figures

Acknowledgments

As it should be with any five year project, there are far too many people to thank to make this section anywhere close to succinct. I first want to thank my advisor, Roger, for being a relentless force of good throughout my Ph.D. I never doubted that Roger had anything but my best interests at heart, and I always found his advice and commentary to be thoughtful and accurate. I appreciated Roger's patient and direct management style and will work to adopt his techniques and perspectives in the future. Secondly, I want to thank my Livermore advisor, Tilo, who taught me everything I know about x-ray scattering and allowed me to take ownership of several projects at the lab. Of course the ownership came with some failures, but the failures were greeted with patience, which allowed me to learn and eventually succeed. Thirdly, I'm grateful for the training I received from Livermore's Amy Jenei. Amy showed me how to run an OMEGA campaign and taught me on-the-fly data analysis techniques, which translated into me being able to make on-the-fly decisions to collect high-quality data during experiments. Amy helped me understand that patience, kindness, and poise are as important as technical ability in a lab career.

In no particular order, I also want to acknowledge the mentorship and support I received throughout my Ph.D. from the following individuals: Barbara Jacak and Raymond Jeanloz for providing thoughtful edits on my thesis to improve the final document; Dirk Gericke for always having good ideas for scattering spectra interpretations; Stephanie Hansen for her relentless pursuit of technical truth, and above all for her kindness and encouragement; Howard Scott for his technical mentorship in design physics; Dave Chapman for his friendship, humor, and unparalleled ability to write detailed technical documents at record speeds; Dominik Kraus for bringing me up to speed in data analysis techniques; Anne Takizawa for being an amazing ally throughout my graduate work and helping all of us navigate the campus bureaucracy; Michael MacDonald for many long technical discussions and his personal and professional generosity; Phil Heimann for piquing my interest in the field of HEDP and helping me write my first LCLS proposals; Félicie Albert for mentoring me in laser wake-field studies; Siegfried Glenzer for teaching me the importance of publication, self-promotion, and self-confidence; Brandon Lahmann and Johan Frenje for including me in stopping power experiments; and Joe Nilsen for his career and reserach guidance. I'd also like to thank the people that supported me outside the lab. First and foremost is my fabulous family, which includes my parents, my brother, and my husband; they all gave me encouragement and valuable advice with their external perspectives. Secondly, my best woman Mari for never letting me doubt myself. I also wouldn't have made it through graduate school without my first-year classmates; so thank you Halleh Balch, Trevor Bowen, Robert Kealhofer, and Charlie Hill for helping with everything from problem sets to social hour.

Finally, I'd like to thank the Krell Institute for managing my DOE NNSA Science Stewardship Graduate Fellowship, which supported my Ph.D. work and helped me understand the importance of the work I do at the national labs.

Chapter 1

Introduction to High Energy Density Physics

1.1 High Energy Density Physics

High energy density physics (HEDP) is a multidisciplinary field that combines elements of plasma physics, condensed matter physics, material science, and mechanical engineering to describe the behavior of matter at extreme conditions. A material at "high energy density" conditions has a pressure of greater than 1 Mbar, which is 10^6 times greater than earth's atmospheric pressure [1]. Another benchmarking metric for HEDP conditions is the sun, which corresponds with temperatures on the order of 6000 to 1.5×10^7 K, or 0.5 to 1200 eV and densities on the order of 1 to 100 g cm^{-3} [1]. These conditions are hotter than typically described by condensed matter physics and denser than typically described by traditional plasma physics, but matter in these regimes shows behavior characteristic of both condensed matter and plasma physics. The fields of high energy and nuclear physics also involve extreme temperatures and densities, but seek to understand the properties and interactions of subatomic particles; experiments in these fields often accelerate a small number of particles to energies on the scale of a particle's rest mass to break them apart and study their compositions. In contrast, HEDP experiments involve comparatively more mass and experiments measure the collective and individual behavior of the atoms under extreme pressures. The advent of high-power laser and pulsed power facilities over the past few decades drove the development of experimental HEDP, as these facilities generate extreme conditions in a controlled environment and offer the ability to make high precision measurements of relevant physical properties [1, 2]. Because of its multidisciplinary nature, HEDP was described as the "X-games of Contemporary Science" in a 2003 report that sought to outline the objectives and challenges that the burgeoning field faced [1]. The report stressed the importance of training a new generation of scientists in the field of HEDP to support critical applications, such as inertial confinement fusion research and the stockpile stewardship program. The report also outlined the challenges of HEDP research, as HEDP is a regime of physics in

which many of our traditional models that describe matter begin to break down; much more experimental validation of models is needed, and new experimental techniques are constantly being developed to drive understanding of HED materials to new levels.

Matter at HED conditions behaves fundamentally differently than matter found on the surface of the earth. Water is offered as an example of an incompressible fluid in an introductory physics course, but the approximation breaks down at pressures exceeding 1 Mbar as atoms begin to ionize and dramatic changes in conventional chemistry occur. Above 10 Mbar, the chemistry that rules the periodic table becomes invalid, and the material resists compression through thermal pressure. Between 100 Mbar and 10 Gbar, continuum lowering and pressure-induced ionization begin to dominate the material's response to pressure, and above 100 Gbar, the material becomes dominated by radiation effects and begins to act like a photon gas. To date, there lacks sufficient experimental data at these high energy densities, marking HEDP as an area of physics with much room for progress and experimental validation of models that seeks to describe this behavior.

Figure 1.1 shows a phase-space plot of different regions of high energy density physics and labels different physical phenomena and objects, such as the big bang and giant planets, in terms of their densities and temperatures. The two black lines in the middle of the plot denote the points at which the thermal energy equals either the Coulomb energy or the Fermi energy. Far above the lines in the phase-space plot, the temperature is hot enough such that the plasmas may be considered as classical plasmas. Near and below the lines, the plasmas are highly coupled and degenerate. The different regions of matter are dominated by different forces and require different treatment in order to predict their behavior. The solid colored lines trace the conditions in astrophysical objects such as brown dwarfs and large planets; from left to right, they show the conditions from the outer to inner radii of the objects. The plot shows the variety of conditions described by high energy density physics and the applicability of HEDP to many astrophysics objects and phenomena, such as the big bang. The vast phase-space of HEDP means many competing physical forces must be considered in the generation of theoretical models. Because of the competing forces, there is uncertainty as to what regimes are dominated by what forces, marking the importance of experimental validation. Figure 1.1 also shows the regions of HEDP that are accessible by the currently available experimental facilities (for more details about the facilities, see Section 1.2). To date, much of the phase space remains experimentally inaccessible, but the regions we can access still offer the ability to probe conditions relevant to many astrophysical objects, such as the sun and giant planets. The field of HEDP is a new and exciting field that still has much room for innovation.

1.1.1 Warm Dense Matter

An important subset of high energy density material is warm dense matter (WDM), which lies in the regime where multiple forces dominate the behavior of the material and standard simplifying approximations cannot be made. Much current research focuses on investigating the properties of WDM due to the significant modeling uncertainties and the relevance of

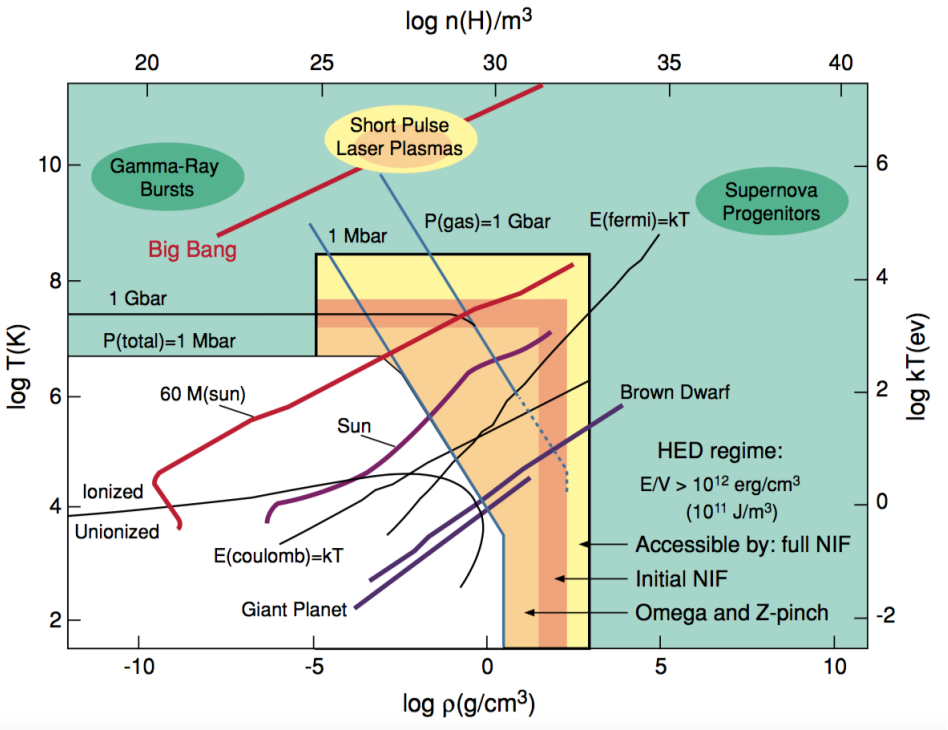

Figure 1.1: A phase-space plot to categorize the different areas of high energy density physics. Two black lines denote the points at which the thermal energy is equal to the Coulomb energy and to the Fermi energy. Far above the lines, the plasmas can be described by classical plasma physics. Close to the lines and below, the plasmas are degenerate and highly coupled. The colored solid density lines indicate the phase-space trajectories of astrophysical objects, such as giant planets and brown dwarfs; the lines trace the conditions from the outer to inner radii of the objects from left to right. Also shown are the regions accessible by the current experimental facilities. Republished with permission of National Academies Press, from Frontiers in High Energy Density Physics: The X-Games of Contemporary Science [1], National Research Council, 2003; permission conveyed through Copyright Clearance Center, Inc.

WDM to planetary interiors, brown dwarfs, and inertial confinement fusion [3, 4, 5, 6, 7, 8, 9, 10, 11]. WDM refers to materials with near solid densities and temperatures between 1 and 10's of eV [2]. More specifically, we quantify the WDM regime with several dimensionless parameters to describe the competing forces that dominate the material's behavior. One parameter is the plasma coupling parameter, Γ, which is defined as the ratio of Coulomb potential energy to thermal energy and is written as:

$$\Gamma = \frac{Z^2 e^2}{r_0 k_B T}\,, \tag{1.1}$$

where Z is the ion charge state, e is the charge of an electron, r_0 is the average distance between ions, defined as $r_0 = (3/4\pi n_i)^{1/3}$, n_i is the ion density, k_B is the Boltzmann constant, and T is the temperature [12, 11]. For WDM, $\Gamma \sim 1$, which means the plasma is moderately coupled and the plasma experiences long- and short-range order due to correlations between the atoms and the ions; in addition, the atoms start to behave in a way that is coupled to the plasma properties [11]. The coupled behavior contrasts with an ideal plasma ($\Gamma \ll 1$), in which atoms are fully described by their isolated motions and the plasma can be treated as a thermal bath. Another way of stating that the coupling parameter in WDM is ~ 1 is to say that the average spacing between ions, r_0, is on the order of the Debye screening length [13]:

$$\lambda_D = \sqrt{\frac{k_b T}{4\pi n_i Z^2 e^2}}\,. \tag{1.2}$$

This means that there are not enough electrons inside a Debye sphere to screen other particles from the Coulomb potential. Charge screening is a fundamental property of classical plasmas, but cannot be assumed in the WDM regime.

Another dimensionless parameter used to describe WDM is the electron degeneracy parameter, Θ, which is the ratio of the thermal energy to the Fermi energy:

$$\Theta = \frac{k_B T}{E_f}\,, \tag{1.3}$$

where the Fermi energy $E_F = \hbar^2/2m_e(3\pi^2 n_e)^{2/3}$, m_e is the mass of an electron, and n_e is the electron density [11]. When $\Theta \gg 1$, the plasma acts classically and the electrons can be described by the Maxwell-Boltzmann energy distribution. When $\Theta \ll 1$, the electrons are fully degenerate and their energy levels can be described by the Fermi-Dirac distribution [12]. In WDM, $\Theta \sim 1$, which means the plasma is moderately degenerate and both quantum and thermal effects must be considered. The challenge in the warm dense matter regime is that the conventional diagnostic techniques and standard plasma theory assumptions that treat correlations and quantum effects as perturbations are no longer applicable [11, 14]. Thus, many of the models used to describe matter in these conditions break down [2, 11, 14]. It is therefore of interest to the HEDP community to generate well characterized WDM states in the laboratory to test models in this regime.

1.1.2 Astrophysical Applications

As seen in Figure 1.1 in Section 1.1, research in high energy density and warm dense matter physics is relevant to the study of astrophysical objects. One such application uses WDM physics to understand planetary formation; the interiors of planets the size Saturn to those a few times greater than Jupiter consist of matter at pressures exceeding 10 Mbar [15]. Much current research seeks to understand the atomic makeup and structure of planetary cores, which informs planetary formation theories [15, 16, 17, 18]. Some theories predict that at the pressures of Jupiter's core, hydrogen and helium will become metallic as a result of pressure

ionization [19, 20, 21, 22, 23]. A metallic core supports a core-accretion planetary formation model, as opposed to a model that predicts Jovian planets form freely from a gas without an initial heavy core [16]. The demonstration of metallic hydrogen in a lab has long been sought as a way to test this theory deriving from WDM physics.

In addition, many WDM experiments seek to investigate the thermodynamics and transport properties of hydrogen and helium at pressures exceeding 10 Mbar in order to understand the formation of brown dwarfs. The exact process of how they form is not well understood [19]. A brown dwarf is a sub-stellar object that is the same size as Jupiter but 10 to 100 times as massive. At the lower end of the mass spectrum, a brown dwarf resists gravitational collapse through Coulomb pressure, but at the higher end, it resists collapse through degeneracy pressure. In the middle of the mass spectrum, the competing forces of degeneracy and Coulomb pressure are a trademark of the WDM regime. Brown dwarfs are not massive enough to fuse hydrogen, but can fuse deuterium, tritium, and lithium. Some experiments analyze observed emission spectra from brown dwarfs in order to understand their detailed chemical makeup and fusion products [20]. Laboratory experiments on warm dense hydrogen and lithium shed light on the underlying structure and behavior of these massive astrophysical objects.

Another astrophysical object with high energy density conditions is the white dwarf, first described by Chandrasekhar in 1931 [24]. The formation of a white dwarf happens when a star fuses all its hydrogen and becomes a red giant. If the red giant doesn't have enough energy to fuse carbon or oxygen, an inert core of carbon and oxygen forms at the center and eventually develops into a white dwarf. Unlike a brown dwarf, the white dwarf doesn't have enough energy to fuse any materials, and only degeneracy pressure prevents its collapse. An average white dwarf is 0.6 solar masses with a radius akin to that of the earth. That means the material in a white dwarf is highly degenerate, with a density of 10^4-10^7 g cm^{-3}. White dwarfs cool over time and can collapse and form supernovae. The physics of white dwarfs is still an area of active research, as very little matter exists in such a dense state [25, 26, 27].

Another application of WDM physics with astrophysical implications is diamond precipitation from a carbon-hydrogen mixture. It is predicted that at the pressures present in gas giants like Uranus and Neptune, the elements that form the molecular methane gas environment will begin to phase separate [28]. Furthermore, under the right conditions, the carbon atoms will begin to form into diamond. The phase separation and diamond formation were demonstrated in an experiment that used CH_4 samples in laser-heated diamond anvil cells [29]. Experimenters also recently demonstrated the formation of nanodiamonds in an experiment on shock compressed CH plastic at the Linac Coherent Light Source, at SLAC National Accelerator Laboratory [30].

Laboratory research of WDM has many applications to astrophysical bodies and helps us understand the behavior of matter extreme conditions that exists naturally in the universe.

1.1.3 Stockpile Stewardship

Another application of high energy density physics is the nuclear weapons program. A report titled "Basic research needs for high energy density laboratory physics" labeled the relationship between unclassified HEDP work and nuclear weapons as the elephant in the room [31], as often the applications of HEDP to weapons cannot be and are not discussed. A nuclear weapon passes through the warm and hot dense matter stages as it detonates, so designing experiments that look at states of matter in those regimes inherently supports our understanding of how weapons function.

It's important to keep in mind that a robust HEDP research program allows us to advance our understanding of weapons without reverting to underground testing of nuclear devices. Testing can result in radiation pollution, among other potentially grave environmental and political consequences. For that reason alone, it is important to keep the field of HEDP thriving such that any weapons-related questions that arise can be answered through controlled laboratory experiments. A large portion of HEDP research remains unclassified so the scientific community can advance our modeling and experimental capabilities. A fusion bomb and an inertial confinement fusion reactor both involve compressing hydrogen isotopes to high densities. Thus, any research in one field promotes research in the other. We as the scientists rely on our policy makers to ensure that the nuclear deterrent we maintain is seen as such internationally, and no nuclear weapon will ever be used in combat again.

1.1.4 Inertial Confinement Fusion

One of the primary applications of high energy density physics research today occurs in the pursuit of laboratory generated inertial confinement fusion (ICF). The goal of these experiments is to hold fusion material together with inertia long enough such that more energy is generated by the system than is put in to compress it; that criteria is referred to as ignition. However, obtaining an ignition reaction in a laboratory has proven to be a complicated task.

In a thermonuclear weapon, the primary stage of a fission reaction generates tens of terajoules ($\sim 10^{13}$ J) of energy to ignite the secondary, which is where an ignition level fusion reaction occurs. In a laboratory setting, the amount of available energy is limited to the energy provided by lasers, which at the National Ignition Facility (see Section 1.2), is on the order of a few megajoules ($\sim 10^6$ J), nearly six orders of magnitude less than in a weapon. Because there is less energy available in the lab, the amount of mass in the fusion target must be smaller than that in a bomb (the mass is also limited by the fact that experimenters don't want the reaction to generate enough energy to destroy the facility). Less mass needs to be compressed more to generate an ignition condition (1000x at the NIF, see following sections for more detail), and then the experiment suffers from the many instabilities that arise from trying to compress matter by that amount.

Figure 1.2 shows a schematic of the four stages of an inertial confinement fusion reaction. At the beginning of the reaction, laser beams (shown as blue arrows) heat the outer surface

of a fusion target, which then causes plasma to ablate at the surface (shown by the orange arrows). The outer surface of the sphere begins to accelerate inwards (shown by the purple arrows) due to conservation of momentum. As the sample continues to compress, the central hot spot reaches pressures akin to those in the center of the sun and fusion reactions begin to occur. Byproducts of the fusion reactions in the hot spot spread to the outer layers and cause more fusion reactions to occur; this is known as thermonuclear burn and is the primary goal of an ICF reaction. Finally, the plasma expands and the pressure drops below what is necessary to sustain a fusion reaction.

A typical fusion reaction consists of a deuterium and tritium nucleus, as seen in Figure 1.3. The two atoms must overcome the Coulomb energy barrier to fuse, which requires ~ 10 keV of energy. The fusion cross section, σ, can be estimated as a product of a geometrical cross section of the reaction and a factor that accounts for the transparency of the quantum tunneling barrier. The highest probability of a fusion reaction occurs at ~ 30 keV, an energy that is a few times higher than the required temperature .

In 1955, John Lawson proposed several criteria to ignite magnetically confined deuterium-tritium (DT) plasmas [32]. Since then, the concept has been extended to understand the ignition criteria for inertially confined plasmas [33, 34, 35], and the criteria are known as the Lawson Criteria. The double-product criterion states:

$$n\tau > 1.5 \times 10^{14} \text{ s cm}^{-3}, \tag{1.4}$$

where n is the DT density and τ is the confinement time [33]. The double-product Lawson Criterion is a time-density product that constrains the requirements for an ignition reaction.

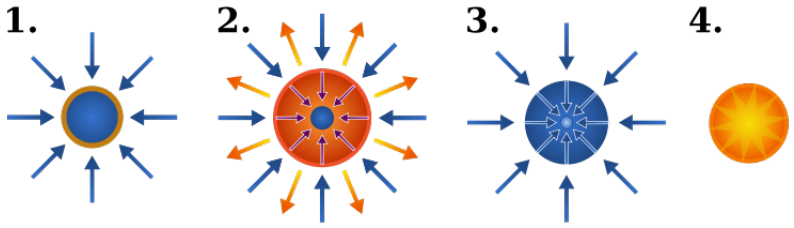

Figure 1.2: A schematic of the four stages of an inertial confinement fusion reaction. 1. Laser beams (shown as blue arrows) heat the outer surface of a fusion target. 2. Plasma begins to ablate (shown by the orange arrows), which causes the outer surface of the sphere to accelerate inwards (shown by the purple arrows) by conservation of momentum. 3. The sample continues to compress, and the central hot spot reaches pressures akin to those in the center of the sun as it begins to ignite. 4. A thermonuclear burn wave propagates outwards through the fuel from the hot-spot until the target completely disassembles. Image by Benjamin D. Esham (bdesham) - Originally uploaded to the English Wikipedia as en:Image:Inertial confinement fusion.jpg by en:User:Deglr6328; marked as a work of the U.S. government and therefore as a public domain image. This version created by bdesham with Inkscape.This vector image was created with Inkscape., Public Domain, https://commons.wikimedia.org/w/index.php?curid=2352291

Some fusion schemes use magnetic fields to confine a lower-density plasma for a longer confinement time, τ [36, 37]. In inertial confinement, much higher density plasmas are confined for much shorter times [13, 34]. Because ICF plasmas are at such high densities, the behavior of the plasmas is described by HEDP.

The confinement time required for an ICF plasma to ignite can be estimated by the amount of time it takes a hot neutron to travel from the central hot spot through the dense core of compressed hydrogen isotopes. Assuming the dense material forms a sphere of radius R with mass M, we estimate the confinement time:

$$\tau = \frac{1}{M}\int_0^R \rho \frac{R-r}{c_s} 4\pi r^2 dr\,, \tag{1.5}$$

where c_s is the material's sound speed [34]. The integral evaluates to:

$$\tau = \frac{R}{4c_s}\,. \tag{1.6}$$

A typical ICF implosion has a dense core with a radius of ~ 100 μm and a sound-speed of 1.3×10^6 ms^{-1} at a temperature of 30 keV [34], which amounts to a confinement time of 20 ps.

We calculate the fusion burn rate:

$$\frac{dn_T}{dt} = n_T n_D \langle \sigma\nu \rangle\,, \tag{1.7}$$

where dn_T/dt is the burn rate of tritium, n_T and n_D are the tritium and deuterium densities, respectively, and $\langle \sigma\nu \rangle$ is the reactivity of the fusion system, which evaluates to the integral

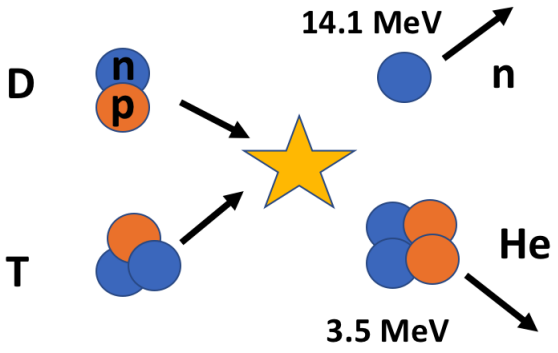

Figure 1.3: A schematic of a typical fusion reaction between a deuterium and tritium atom. Protons and neutrons are shown as red and blue circles, respectively. Once the atoms overcome the Coulomb barrier, a fusion reaction can occur, which results in a neutron and alpha particle.

of the fusion cross section over the particle velocity distribution [34]. Assuming that $n_D = n_T = n$, we simplify the expression for the fusion burn rate [34]:

$$\frac{dn}{dt} = \frac{n^2}{2}\langle\sigma\nu\rangle\,. \tag{1.8}$$

Integrating the fusion burn rate over the confinement time leads to the relation:

$$\frac{1}{n_f} - \frac{1}{n_i} = \frac{1}{2}\langle\sigma\nu\rangle\tau = \frac{R}{8c_s}\langle\sigma\nu\rangle\,, \tag{1.9}$$

where n_i is the initial number density of fuel, and n_f is the final density of fuel remaining that hasn't been burnt [34]. We define the fusion burn rate:

$$f = 1 - \frac{n_f}{n_i}\,, \tag{1.10}$$

and if we define $n_i = \rho/m_{DT}$, where m_{DT} is the mass of an average DT nucleus (2.5 AMU), we estimate the burn fraction as:

$$f = \frac{\rho R}{\rho R + 8m_{DT}c_s/\langle\sigma\nu\rangle}\,. \tag{1.11}$$

At 30 keV, the most probable temperature for fusion reactions [13], we express the burn fraction as:

$$f = \frac{\rho R}{\rho R + 6\ \mathrm{g/cm^2}}\,. \tag{1.12}$$

Clearly, the burn fraction depends on the areal density, ρR. The stagnation pressure and the Lawson criterium can also be expressed in terms of ρR, marking the areal density as a way to quantify the compression necessary to obtain ignition. In order to overcome inefficiencies of an ICF implosion, an ideal burn fraction of the fuel for ICF reactions is $f = 1/3$ [34], which corresponds with a $\rho R = 3\ \mathrm{g\,cm^{-1}}^2$. This new $\rho R = 3\ \mathrm{g\,cm^{-3}}$ condition can be used to rewrite the Lawson criterion in terms of number density and confinement time as $n\tau = 2 \times 10^{15}\ \mathrm{s\ cm^{-3}}$. This means that the Lawson Criterion for ICF implosions is roughly 20 times greater than that for magnetically confined plasmas, which arises from inefficiencies involved in assembling mass to high densities during ICF implosions [34].

We can solve the ICF Lawson Criterion with the confinement time of 20 ps to obtain the required number density of $n = 10^{26}\ \mathrm{cm^{-3}}$. This means a 1 mm-scale target needs to compress by a factor of 1000 in order to achieve ignition. In practice, the only way to achieve a convergence ratio of 1000 is to use spherical implosions. As the sphere compresses, the density scales as R^3, which means the radius needs to decrease by a factor of 30. This required decrease in radius implies that implosion symmetry plays a large role in the success of an experiment. To further the calculations, we estimate the implosion velocity and ablation pressures required to decrease the radius by this amount by equating the implosion kinetic

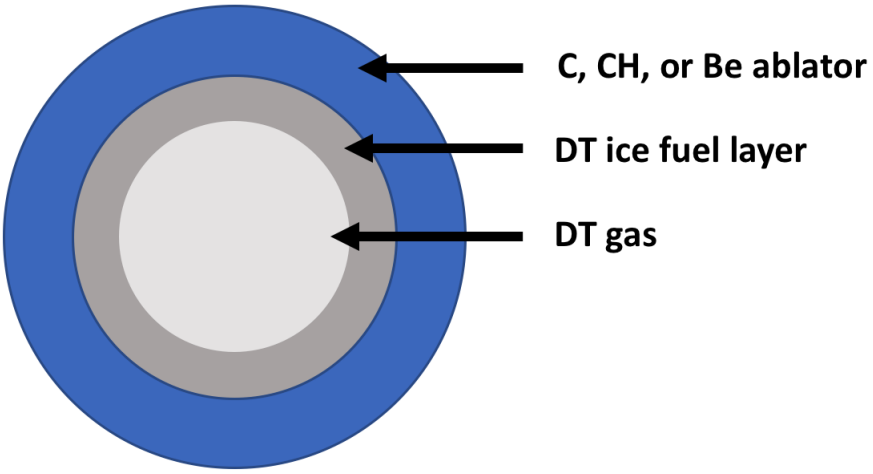

Figure 1.4: A schematic of a typical ICF capsule target. The outer layer consists of a low-Z material, such as C, CH, or Be, designed to ablate off with radiation incident on the surface. The ablation causes the second layer of DT fuel to accelerate inwards and compress. The middle of the target is filled with DT gas at the vapor pressure of the inner-surface of the solid fuel layer.

energy to the Fermi degeneracy pressure of the compressed target [34]. In doing that, we find that $v_{imp} \sim 3.5 \times 10^9$ m s^{-1} and that $P_{abl} \sim 60$ Mbar.

These calculations serve to outline the length and time-scales relevant to ICF experiments. In short, a small capsule must be compressed to very high densities for a short period of time in order to attain the necessary burn fraction to generate ignition. In order to attain the necessary densities on the necessary timescales, ICF capsules compress spherical shells of DT ice. A schematic of an ICF target is shown in Figure 1.4. The outer layer of the target is called the ablator and serves to help compress the target; the ablator layer is often made from beryllium, carbon-based plastic, diamond, or boron carbite [38]. There are several features of ablators that help facilitate capsule compression. One feature is a mid- or high-z dopant in one layer, which absorbs x-rays and prevents the fuel from becoming pre-heated from drive radiation, which would cause the fuel to resist compression due to thermal pressure. Another important consideration of ablators is transparency to the driving radiation source once the ablator material is ionized; the radiation must be able to reach the surface of the ablator to compress the capsule continuously. Carbon and beryllium become nearly transparent to low energy x-rays once their atoms become mostly ionized, which is why ablator materials are rarely made of heavier elements [2]. In principle, high density carbon and boron-carbite are more ideal than lower density ablators, like CH plastic, because heavier atoms can generate greater ablation pressures; however, manufacturing challenges and crystal structures complicate the use and implosion dynamics of these heavier elements.

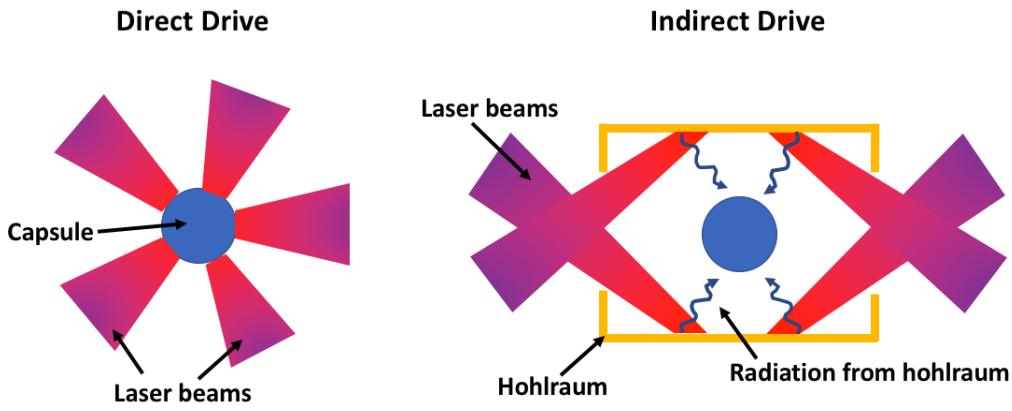

Figure 1.5: Schematics of direct-drive and indirect-drive approaches to ICF. In direct-drive, lasers deposit their energy directly on the capsule surface. In indirect-drive, lasers heat the inner walls of a high-Z hohlraum, which reemits radiation to compress the capsule.

The fuel itself comprises a frozen DT mixture in a spherical shell under the ablator, as seen in Figure 1.4. A cryogenic target both increases the initial fuel density and decreases the amount of compression required to attain the necessary densities for ignition [39]. Using a solid as opposed to liquid fuel layer provides several advantages to the implosion, including minimizing some aspects of the Rayleigh-Taylor instability, which can degrade target performance [39]. Finally, a hollow capsule is preferable to a solid sphere because less peak power and less extreme variations of power with respect to time are required to reach high pressures in the sample [40]; given a certain strength radiation drive, it is easier to compress a shell with a high velocity implosion than it is to send shock wave through a solid sphere at the same velocity. DT gas fills the inner section of the sphere at the vapor pressure of the inner-surface of the solid fuel layer. The density of DT vapor can be controlled by controlling the temperature of the target, and the vapor forms part of the hot spot after the implosion begins, as the vapor gets much hotter than the surrounding fuel [41].

There are two main approaches to laser-driven ICF: direct- and indirect-drive [2, 41, 42]. Figure 1.5 shows a schematic of the two different approaches. In a direct-drive approach, as seen on the left of Figure 1.5, the lasers deposit energy directly onto the surface of the sample. The lasers are tuned to irradiate at intensities ranging from 10^{12} to 10^{16} W/cm^2 [2]. At the higher-end of these intensities, the electric field from the laser is strong enough to ionize the electrons in the ablator directly. At the lower-end of the intensities, the laser light deposits energy in the material through the inverse-bremsstrahlung process; the light penetrates into the ablator layer until the light reaches a surface of a critical density at which point most of the light is absorbed. Electrons then penetrate further into the ablator, depositing more energy, until an ablation front is formed (for more details on the physics of a laser-driven shock, see Section 2.3.1). Then plasma heats and expands and generates an ablation pressure.

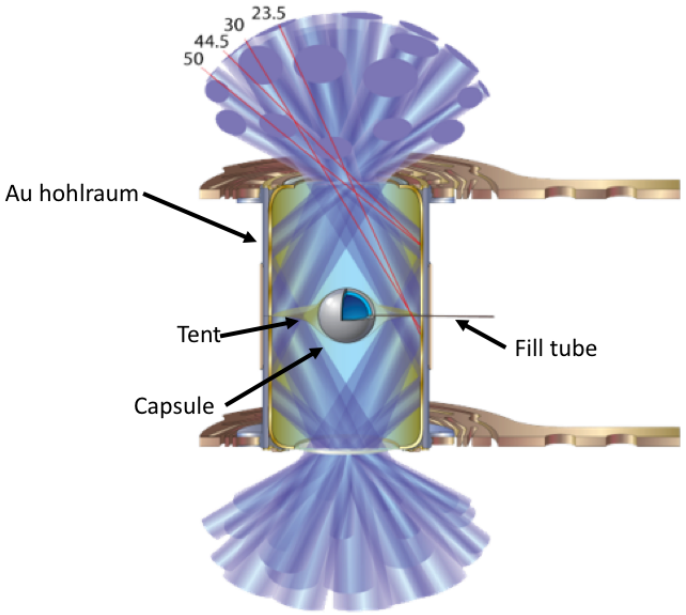

Figure 1.6: Schematic of an indirect-drive platform on NIF. A cylindrical gold hohlraum encases the capsule, which is held in place by two layers of thin of plastic, called "the tent." A fill tube fills the ablator shell with the liquid fuel.

The other approach to laser-driven ICF involves indirectly driving the implosion with x-rays generated from a hohlraum, as seen in the right side of Figure 1.5. In the indirect-drive approach, lasers deposit energy into a high-Z material which heats and radiates x-rays to compress the capsule. The x-ray spectrum mimics a black-body spectrum, with additional x-ray features generated by the high-Z material. Figure 1.6 shows a more detailed schematic of a typical indirect-drive target. A cylindrical gold hohlraum (the German word "hohlraum" translates as "cavity" in English) encases the capsule, which is held in place by two layers of thin of plastic, called "the tent." A fill tube fills the ablator shell of the capsule with the DT gas fuel; as the capsule is cooled to cryogenic temperatures, the gas cools to a liquid and forms an ice layer. For the case of ICF at Livermore, hohlraums are almost always made of gold due to manufacturing facility and high x-ray conversion efficiency. However, other high-Z materials and compounds such as lead and depleted uranium have been explored [43, 44, 45].

Both approaches to ICF have their advantages and disadvantages. The primary advantage of direct drive is better coupling efficiency of the laser energy to the imploding shell's kinetic energy, since the laser impinges directly on the target. However, direct laser ablation also makes the implosion more sensitive to variations in the spatial laser profile, which leads to less symmetric implosions with instabilities that result from imprints of laser spots on the capsule surface [46]. Experimenters made many improvements to the design of direct-drive

experiments since the declassification of laser-driven shocks in the 1970's. One improvement involved changing the wavelength of laser light from infrared to frequency-tripled infrared; the shorter wavelength generated less suprathermal electrons, which led to less preheating of the ICF fuel. Other improvements sought to smooth out the laser spatial profile through techniques such as phase plates and smoothing by spectral dispersion; these reduced the speckle pattern from hot spots in the beam spots, which generated drive asymmetries that propagated through the implosion. Experimenters then focused on reducing the hydrodynamic instabilities that arose as a result of the lasers imprinting a pattern on the capsule surface. Research in direct-drive is still ongoing.

Because of the reduced requirements for laser uniformity and lower sensitivity to hydrodynamic instabilities, the US has primarily focused on achieving ICF through indirect-drive platforms since 1976 [35]. However, hohlraums also present a myriad of complicated physics interactions that complicate laboratory ignition efforts. One such problem includes gold plasma ablating inwards from the hohlraum walls; the under-dense gold plasma undergoes stimulated Raman scattering with the drive laser and electron-transport, which results in areas of high and low temperatures. The temperature of the under-dense Au plasma ranges from 2 keV, near the spots where the lasers interact with the solid hohlraum, to ∼300 eV, or near the wall temperature. Experiments seek to understand the spatial distributions of those temperatures through spectroscopy from localized microdots [47]. To combat the effects of gold plasma filling the hohlraum, the hohlraum is often filled with gas to provide a back-pressure for the expanding Au wall plasma. However, the gas generates its own laser-plasma instabilities. In addition, even though the drive from a hohlraum is more symmetric than that from direct-drive, the drive is still not perfectly symmetric, and hydrodynamic instabilities still arise. The many challenges of hohlraums are left for the reader to explore on her own from here on out.

Although experimenters continue to increase energy yields from fusion experiments, no experiment has thus far achieved ignition. Several reports outline the challenges experimenters face in pursuing laboratory fusion and some of the attempted mitigating strategies [48, 49, 50]. The original National Ignition Campaign (NIC) on the NIF ran for three years, between 2009 and 2012, and sought to maximize the ρR of the fuel [38]. Experimenters used a four-shock design to compress the capsule efficiently at a low adiabat, with an initial small shock, called the "foot," generated by a 60 eV radiation drive. NIC was successful in achieving high compression ($\rho R \sim 1.24$ g cm^{-2}), but neutron yields were limited to 7.5×10^{14}. One reason the campaign failed to achieve higher yields was because the NIC design showed very large growth factors for perturbations seeded at the capsule surface. One particularly strong perturbation originated from the contact ring where the capsule support tent meets the capsule. The tent caused mix of the ablator into the hot-spot, which affected the ability of the fuel to burn [50]; however, mix occured from other asymmetries as well. Tent mitigation strategies are still areas of active research.

After NIC, experimenters implemented a high-foot drive design [38, 50, 51]. The higher energy initial shock reduced the tent-driven hydrodynamic instabilities, and improved the neutron yield to 9×10^{15} neutrons, with a DT fuel ρR of 0.83 g cm^{-2}.The Rayleigh-Taylor

growth rate depends inversely on density gradient scale length and mass ablation rate; the stronger initial shock decreased the gradients between the first and second shocks and increased the implosion velocity, thus reducing the instability. However, this limited the amount the fuel could be compressed which lowered the final ρR [51]. Despite the lower ρR, the high-foot campaign increased the fusion yield by a factor of ten by obtaining α-particle self-heating; α-particle self-heating is a secondary fusion step that occurs when the α-particles from the fusion reactions in the central hot-spot deposit energy into the surrounding colder, denser fuel and cause more fusion reactions to occur there [52]. We are still in a regime where α re-deposition into the hot-spot is the main source of yield.

The high-foot campaign also involved the development of many different experimental platforms that sought to investigate the high energy density physics involved in these implosions [50]. Different campaigns probed different properties, ranging from equation of states to hydrodynamic instabilities. An intense computational effort followed, which tried to match the outputs of the hydrodynamic codes to the experimental results from both the fusion and physics platforms [38]. Radiation hydrodynamic codes such as HYDRA [53], which sought to predict implosion outcomes, often showed predictions that differed vastly from the experimental results. Recent ICF campaigns on the NIF explored the use of diamond, or high density carbon (HDC), as an ablator material [54, 55]. HDC further reduces hydrodynamic instability and hot-spot mix, which increased yields above the 1×10^{16} neutrons mark. However, more work remains to be done before ignition can occur.

ICF implosions remain highly sensitive to the hydrodynamic instabilities involved with compressing matter to 1000$\times$ solid densities. The field of HEDP provides a way to quantify and explore the different instabilities and forces acting in ICF implosions in order to help generate ignition in the laboratory.

1.2 Experimental Facilities for HEDP Research and Applications

There are several facilities capable of compressing matter to conditions at which ignition can occur. The three primary facilities in the United States are described in the following sections.

1.2.1 The OMEGA Laser

The OMEGA Laser is part of the Laser Laboratory for Energetics (LLE), which is part of the University of Rochester in Rochester, New York [56]. An original 24-beam laser was built at LLE in 1980 and the laser was upgraded to the current 60-beam version of the OMEGA Laser in 1995. Figure 1.7 shows an areal schematic of the laser and an image inside the target chamber during an implosion. The laser facility is 10 m tall and 100 m in length, which is approximately the size of one football field. The OMEGA laser is a 60 beam, 351 nm, Nd:glass laser that can deliver over 30 kJ in energy to the target on ns timescales [46,

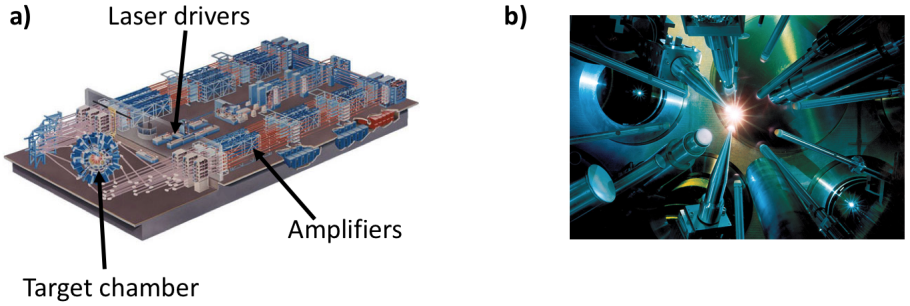

Figure 1.7: a) Areal schematic of the OMEGA laser. The pulse driver generates and shapes seed pulses and delivers them to the amplifiers. The amplifiers increase the energy of the beams, which are eventually focused to a millimeter-scale target at the center of the traget chamber. b) A picture of the inside of the target chamber during the implosion. Different diagnostics point into the center of the chamber. Credit: University of Rochester.

56]. The beams can be focused to 85 μm spot sizes, and can be pointed with a 15 μm accuracy. As seen in Figure 1.7, the pulse driver generates seed pulses, which then split and propagate through the amplifiers until the laser energy impinges on a target. The laser can repeat shots as quickly as once per 45 minutes, which means that experimenters can obtain 10 - 14 shots per day. The 60 beams are distributed spherically around the center of the chamber and as such are optimized for direct-drive capsule implosions.

The OMEGA target chamber has diagnostic ports around it's exterior. Users of the laser can specify diagnostics they would like in each port, as the majority of OMEGA diagnostics are "plug and play" and are designed to work in any port. A ten-inch manipulator (TIM) inserts the diagnostic into the chamber. In a typical experiment, the user has access to six separate TIM's, each at a different position around the target chamber. Typical diagnostics include spectrometers, time-gated x-ray framing cameras, time-of-flight detectors, and diodes.

The main advantage of the OMEGA facility is that experimenters can get many shots per day, and access to shot days tends to be easier than that on larger lasers. The OMEGA laser produces many high-profile papers in high energy density physics and is an essential machine in the field.

1.2.2 The National Ignition Facility

The National Ignition Facility (NIF) is currently the world's largest and most energetic laser. The NIF project began in 1995 and was completed in 2009; the laser continues to run today [57]. Figure 1.8 shows an areal schematic of the laser and a picture of the outside of the target chamber. Roughly three football fields would fit into the NIF laser bay, demonstrating the massive size of the facility. The NIF is a 192 beam Nd:glass laser system that can deliver over 1.8 MJ to a millimeter-scale target on time scales of nanoseconds. The

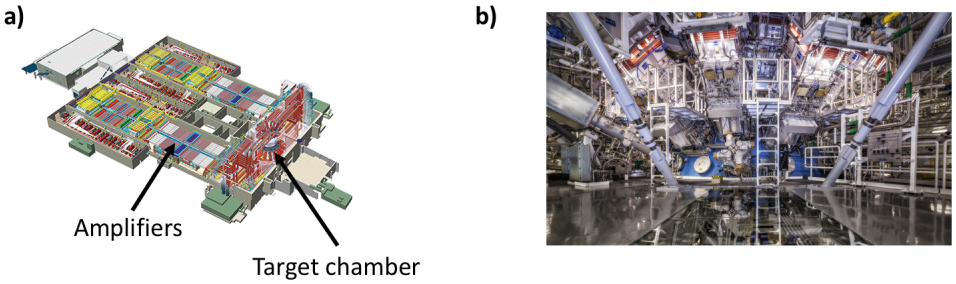

Figure 1.8: a) Areal schematic of the National Ignition Facility. The lasers are amplified in two different laser bays, until they are focused to a millimeter-scale target at the center of the target chamber. b) Picture of the top half of the NIF target chamber, which is 10 m in diameter. Square laser transport tubes and other diagnostics sit on the sides of the chamber.

lasers are arranged around the north and south poles and as such are optimized for indirect-drive implosions. The laser can fire 1 - 3 shots per day, with the cooling of the amplifier optics limiting the recovery time between shots. The NIF is a high accuracy machine, with high-precision and repeatable laser pulse shaping and pointing accuracy on the scale of 15 μm.

The target chamber itself is 13 m in diameter. Various fixed diagnostics are distributed around the chamber, and several diagnostic ports can be swapped out using diagnostic instrument manipulators, or DIM's.

1.2.3 The Z-Machine

The Z-machine is another facility that pursues inertial confinement fusion research, but is not a laser facility like OMEGA or NIF. The Z-machine is a pulsed-power facility that delivers 30 MA currents to create magnetic fields above 1000 T and pressures ranging up to 1 Gbar [58, 59]. The machine was originally built as the "particle beam fusion accelerator" (PBFA) in 1980, but was upgraded to PBFA-Z, or the Z-machine, in 1996. The Z-machine can be run in two different configurations. In the Z-pinch configuration, a cylindrical current implodes a wire array by the Lorentz force, which generates high energy densities and large amounts of x-rays. The x-rays from one implosion contain about 2 MJ of energy, putting it on par with the National Ignition Facility. The imploding wire array can be considered a dynamic hohlraum, which then compresses a capsule inside of it. Another configuration involves using the magnetic pressure to launch a flyer plate, which can shock materials up to pressures of 10 Mbar [58]. The Z-machine can be fired once a day, as each time it fires the target implodes and generates debris. The inside of the target chamber must be physically cleaned out before a new sample is placed inside.

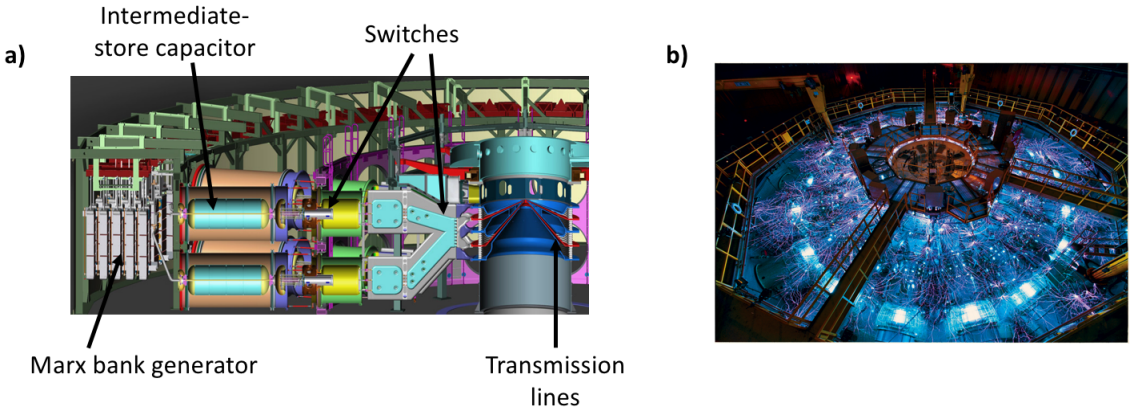

Figure 1.9: a) Schematic side-view of Sandia's Z-machine. Power is stored in the Marx bank capacitors, until it is released and flows through a series of secondary capacitors and switches. The power flows through transmission lines until it reaches the center of the target chamber. The quickly changing electric field from the flowing current generates a magnetic pressure on the sample. b) A picture of the Z-machine during firing.

1.3 Thesis Outline

Chapter 1 outlined the field of high energy density physics and the motivations as to why studying warm dense matter is both challenging and well warranted. The remainder of this thesis will describe my contributions to the field of high energy density physics and present the necessary theoretical background to understand my work. Chapter 2 describes the equation of state variables relevant to warm dense matter and the different models available to describe the ionization state. The chapter also discusses the Hugoniot relations and outlines the importance of the Hugoniot in understanding the equation of state. Chapter 3 describes the different tools we use to study warm dense matter and discusses the advantages and disadvantages of each tool. Chapter 3 also describes the Gbar platform on the NIF, which inspired much of my work. Chapter 4 describes x-ray Thomson scattering (XRTS) in detail, ranging from experimental design considerations to data analysis techniques. Chapter 5 describes an x-ray scattering experiment on the OMEGA laser that was performed on solid diamond spheres and discusses the results. Chapter 6 describes scattering data I analyzed in order to return information about a small impurity fraction in a material. Chapter 7 describes another scattering experiment I performed on the OMEGA laser that measured the temperature of plasmas involved in ion stopping power experiments. And the final chapter, Chapter 8, summarizes my work and provides several suggested future directions.

1.4 Role of the Author

All my work is only possible through collaborations with Lawrence Livermore National Laboratory, University of Rochester, and the MIT Plasma Science and Fusion Center. I here outline my role in the experiments presented in the following chapters.

- *Chapter 4: Implementation of XRTS Experiments on the OMEGA Laser*: Dr. Tilo Döppner and Dr. Amy Jenei of LLNL guided target design decisions and experimental implementation.
- *Chapter 5: X-ray Thomson Scattering and Radiography from Imploding Diamond Spheres on the OMEGA Laser*: Dr. Döppner and Dr. Wolfgang Theobald (University of Rochester) aided in experimental design considerations. Both Dr. Döppner and Dr. Michael MacDonald (UC Berkeley) aided in experimental implementation and data interpretation.
- *Chapter 6: Influence of Argon Impurities on Elastic X-ray Scattering from Imploding Beryllium Capsules*: This paper was a reanalysis of data taken by Kritcher et al. [60]. Prof. Dirk Gericke and Dr. Tilo Döppner aided in data interpretation. The results in this these were published in Reference [61].
- *Chapter 7: Using X-ray Thomson Scattering to Measure Temperature in Ion Stopping Power Experiments*: Brandon Lahmann of MIT acted as the principal investigator of the experimental campaign. Dr. Döppner and Dr. Johan Frenje guided target design decisions.

Chapter 2

Characterization and Generation of Warm Dense Matter

The previous chapter outlined the field of high energy density physics and detailed why warm dense matter is a complex and relevant field. Chapter 1 also described inertial confinement fusion research and the facilities at which ICF and HEDP research is pursued. This chapter will describe methods of characterizing warm dense matter states, which are relevant to both HEDP and ICF.

2.1 Equations of State

To generate warm and hot dense matter in the lab, an experimenter must impose a force that generates a pressure on a material. It is useful to quantify the response of that material in terms of an equation of state (EOS), which describes the relationship between material properties such as pressure, temperature, energy, and density. The following sections outline the different EOS's that can be used to describe materials at high energy densities. Different physical forces dominate the behavior of a material in different temperature and density regimes. Thus, different equations of state can become more or less relevant depending on the plasma conditions.

2.1.1 Ideal Gas

The simplest equation of state is the ideal gas law, which relates pressure P, volume V, temperature T, and particle number N by:

$$PV = Nk_BT \tag{2.1}$$

where $k_B = 8.62^{-5}$ eV/K is Boltzmann's constant [2]. We can rewrite the law in terms of the ionization state of the material, Z, the average atomic mass of the ions, A, and the proton

mass, m_p:

$$P = \frac{\rho(1+Z)k_BT}{Am_p} \tag{2.2}$$

where ρ is the mass density of the material and $V/N = Am_p/\rho(1+Z)$ [2]. In the case of a polytropic ideal gas, we can also derive the sound speed c_s and the specific internal energy, ϵ:

$$c_s^2 = \frac{\gamma P}{\rho} \,, \tag{2.3}$$

$$\rho\epsilon = \frac{P}{\gamma - 1} \,, \tag{2.4}$$

where γ is the polytropic index [2]. In the case of an ideal gas with n degrees of freedom, $\gamma = (n+2)/n$.

A polytropic process is one in which PV^x is constant for all x. In the case of an adiabatic process, $PV^\gamma = constant$. Of course the polytropic EOS equations outlined above assume that the material in question is an ideal gas. In general, a plasma is not an ideal gas, especially when in the warm dense matter state. However, if the temperature of the plasma is well above the temperature required to fully ionize all atoms, then the plasma can be reasonably described by the polytropic equations. And even when the polytropic equations are not particularly accurate, they are often useful in describing the general reliance of one variable on the others.

2.1.2 Warm Dense Matter

As expected, the equation of state in the warm dense matter regime is much more complicated than that of the polytropic ideal gas. As discussed in Section 1.1.1, warm dense matter is often degenerate and highly coupled, which means a plasma in the warm dense matter state responds to pressure fundamentally differently than does an ideal gas.

In a classical plasma, thermal pressure acts to resist compression. In the case of dense matter, degeneracy pressure can also resist compression. This arises from the fact that electrons are fermions, which means only two electrons, one with spin up and one with spin down, can occupy any one energy state. We characterize the degeneracy of the system with the Fermi energy. At zero temperature, the Fermi energy is the highest occupied energy state of an electron gas:

$$\epsilon_F = \frac{h^2}{2m_e}\left(\frac{3}{8\pi}n_e\right)^{\frac{2}{3}} \,, \tag{2.5}$$

where h is Plank's constant, m_e is the mass of the electron, and n_e is the electron density [62]. At temperatures greater that zero, the Fermi energy can be interpreted as the energy equal to the chemical potential, or the energy level with a 50% chance of occupancy. We approximate the Fermi energy in terms of more useful units:

$$\epsilon_F = 7.9 n_{23}^{2/3} \text{ eV} \,, \tag{2.6}$$

where n_{23} is the electron density in units of 10^{23} cm^{-3} [2]; a typical metal at room temperature has an electron density of 3×10^{23} cm^{-3}. In practice, the expression for the Fermi energy at 0 K is compared with the temperature of the system. If $k_B T \gg \epsilon_F$, the electrons can be approximated as free particles. However, in the case of warm dense matter, it is often true that $k_B T \leq \epsilon_F$ and quantum effects like degeneracy pressure must be considered.

In the case of a degenerate plasma, the equation of state is similar to that of a polytropic gas with $\gamma = 5/3$ [2]. The pressure can then be written as:

$$P = \frac{h^2}{20 m_e} \left(\frac{3}{\pi}\right)^{\frac{2}{3}} n_e^{5/3} \,, \tag{2.7}$$

or in the units of Mbar [2]:

$$P = 9.9 \left(\frac{\rho}{A/Z}\right)^{\frac{5}{3}} \text{Mbar} \,. \tag{2.8}$$

Another type of pressure that can play a role in high energy density materials is radiation pressure. Radiation pressure is defined by:

$$P_R = \frac{4}{3}\frac{\sigma}{c} T^4 \,, \tag{2.9}$$

where $\sigma = 5.67 \times 10^{-8}$ Wm^{-2}K^{-4} is the Stefan-Boltzmann constant, and c is the speed of light. Because P_R varies with temperature to the fourth power, radiation pressure rarely dominates the equation of state in warm dense matter. However, in some high pressure experiments, the shock front heats enough to radiate and become radiation-dominated. To determine at what temperature a material switches into a radiation-dominated regime, the polytropic pressure and radiation pressures can be equated to each other. Solving for temperature returns [2]:

$$T(\text{keV}) = 2.6 \left(\frac{\rho(1+Z)}{A}\right)^{\frac{1}{3}} \,. \tag{2.10}$$

For solid density plasmas with $\rho = 1$ g cm^{-3}, this occurs at temperatures of 1 keV, which corresponds with a pressure of 50 Mbar. It is also worth noting that a radiation-dominated plasma has an adiabatic index of $\gamma = 4/3$.

2.1.3 Tabular

While the expressions for pressures in degenerate, polytropic gases, and radiation-dominated plasmas are appealing for their simple analytic expressions, they are often not accurate enough for most practical applications. The radiation hydrodynamics codes of Livermore, such as HYDRA [53], rely on an accurate EOS to model ICF-related implosions. These codes typically use what's called a tabular EOS, which is a table that gives two thermodynamic variables (ρ, P, ϵ, or T) as a function of the other two [2]. This allows for benchmarking

different variables of the EOS with experiments or costly simulations, such as density functional theory or molecular dynamics. These EOS tables must be consistent with the laws of thermodynamics, in that if one variable is held constant and the other varied, the equation of state must obey the first law of thermodynamics. In practice, this is harder than it may seem, and there are countless examples of different calculations of EOS tables for materials at conditions relevant to ICF and in the warm dense matter regime [3, 63, 64, 65, 66, 67, 68].

Many experiments seek to benchmark EOS tables by measuring plasma parameters, such as temperature and density, and equating them to pressure [69, 70, 71, 72, 73, 74]. By doing so, the tabular equations of state can be refined to better predict implosion behavior. A refined table of state will allow simulations to better predict implosion dynamics of ICF experiments, helping with the quest to attain laboratory generated ignition.

2.2 Ionization in Warm Dense Matter

The ionization state of a material affects many physical properties, such as thermal conductivity, radiation transport, and compressibility. This is because an applied pressure adds energy to a system, and the number of free electrons affects how the system absorbs that energy. For example, plasma pressure scales linearly with Z, electron thermal conductivity scales with Z^{-2}, bremsstrahlung radiation scales with Z^2, and the photoelectric absorption cross-section scales with Z^4 [12]. Because ionization affects so many processes, it is important to understand how ionized a material becomes at a specific temperature and density. This is a particularly challenging problem in the warm dense matter regime, in which continuum lowering dominates the ionization state of the material [12]. Much current experimental and theoretical work seeks to investigate the degree of ionization in warm dense matter [75, 76, 77, 78]. Several experiments found higher ionization states than predicted by any commonly applied ionization model [75, 79]; however, the results have come under criticism due to potentially inconsistent and incomplete modeling [80]. Thus, more experiments are needed to benchmark the ionization in the warm dense matter regime.

In warm and hot dense matter, the temperatures are high enough such that all molecules of the original material are each broken up into their constituent atoms [12]. The ionization state of warm dense matter, Z, is defined as the average number of stripped electrons per each atom. For a single atom, Z can only take on integer values. But for a material, Z refers to the average ionization state of a sample, and the distribution of individual ion species that amounts to the average ionization state Z is called the ionization balance. This section presents several models to calculate ionization in plasmas. Functionally, there are three events that can cause ionization: collisions, radiation-induced transitions, and magnetic induced ionization.

The ionization state of a material is determined by the balance of two competing processes: collisional ionization and collisional recombination, or radiative ionization and radiative recombination. In cases where the plasma is not in local thermodynamic equilibrium,

two different processes may act in opposition. For example, in a low density and high temperature plasma, coronal equilibrium is obtained because radiative recombination balances collisional ionization. Coronal equilibrium is aptly named because it occurs in the corona of our sun.

In general, calculating the ionization state of a material is a complicated process that depends on detailed atomic physics. To this day, we still do not have accurate ionization models for matter at extreme conditions. However, the following models show the general behavior of ionization state with respect to equation of state variables, such as density and temperature.

2.2.1 The Saha Model

The simplest model for ionization in plasmas is the Saha equation [81], which denotes the ratio of densities between two ion species with successive ionization states. The Saha equation calculates the most probable state of an atom using the grand canonical partition functions for the three types of particles involved in an ionization event: an atom ionized to m, and an atom ionized to $m+1$ plus a free electron. The electron's partition function is calculated from Maxwell-Boltzmann statistics, and the ions' partition functions are calculated using a hydrogen-like atomic configuration. The Saha equation reads [81]:

$$\frac{n_{m+1}}{n_m} n_e = \frac{g_{m+1}}{g_m} \frac{2}{\lambda_D^3} e^{I_{m+1}/kT} \,, \tag{2.11}$$

where n_m is the number density of ions with state of m, n_e is the free electron density, g_m is the statistical weight of the of state m, $\lambda_D = h/\sqrt{2\pi m_e kT}$ is the thermal DeBroglie wavelength of an electron, and I_{m+1} is the ionization potential of the ion with state $m+1$. The Saha equation can be solved for all charge states to find the ionization balance. In general, the distribution of ionization states is roughly Gaussian.

We can translate the Saha equation to more useful units by assuming there is an ionization state Z_{bal}, for which $n_{m+1}/n_m = 1$ for two charge states $Z_{bal}+1/2$ and $Z_{bal}-1/2$. In this case, because the distribution of charge states is roughly Gaussian, we would expect $Z_{bal} \sim Z$. We can then solve Equation 2.11 for Z_{bal} and obtain [2]:

$$Z_{bal} = 19.7 \sqrt{T_e \left(1 + 0.18 \ln \frac{T_e^{3/2}}{n_{24}} \right)} - \frac{1}{2} \,, \tag{2.12}$$

where n_{24} is the electron density in units of 10^{24} cm^{-3}.

Equation 2.12 shows that ionization increases with increasing temperature and decreases with increasing density. This intuitively makes sense, as a higher temperature implies that more electrons will have energies high enough to undergo ionizational collisions. The competing process, collisional recombination, scales with density; this is why ionization state decreases as a function of increasing density [13]. The Saha equation only applies for the

case of low density plasmas dominated by statistical mechanics, when the governing energies are ionization and excitation [2] and there is no screening of charges [12]. The Saha equation fails to predict ionization in the case of high densities or the presence of non-local thermodynamic equilibrium effects.

2.2.2 Ionization Potential Depression

In warm dense matter, the electrons are often partially degenerate and the inter-atomic potentials between ions must be considered. The Saha equation can be adjusted to account for the correlations by applying an energy offset to the ionization potential of bound electrons; this is referred to as ionization potential depression (IPD), and is also referred to as continuum lowering or pressure ionization. There are many different models that calculate IPD in dense plasmas, but there remains no one model that accurately predicts ionization for all density and temperature regimes.

Figure 2.1(a) shows a simplified cartoon of IPD. The left side shows the electron energy levels of a single atom; all electrons are bound to the ion because they have lower energies than the continuum states. The right side of the figure shows the same electron energy levels, but this time in a dense system. The electrons begin to experience the fields from the neighboring particles, which lowers the energy of the continuum. Now several electrons have energies that are higher than the continuum and are ionized. In the warm dense matter regime, IPD plays a large role in governing the ionization state of the system.

To quantify the effects of ionization potential depression, one must calculate an offset in the binding energy of the electrons. This offset in energy takes the form of the binding energy of the electron in the Bohr model for the hydrogen atom, which was a simplified model, derived before Schrödinger's description of the hydrogen atom existed. The derivation of the Bohr atom energy levels relies on three principles: 1) the Coulomb force between the electron and the nucleus balances the centrifugal force of the orbiting electron, 2) the electron's energy is the sum of kinetic and potential energy, and 3) an orbit of the electron around the nucleus must be done in discrete steps. We solve for the binding energy, E:

$$E = -\frac{Z^* e^2}{2a} \ , \tag{2.13}$$

where Z^* is the nuclear charge, e is the charge of the electron, and a is the classical radius of the electron orbit. For hydrogen, $a = a_0 = 5.29 \times 10^{-11}$ m is the Bohr radius and $E = -13.6$ eV. In a similar fashion, the continuum lowering models calculate ΔI:

$$\Delta I = \frac{Z^* e^2}{2a_n} \ , \tag{2.14}$$

where Z^* is the ion charge, n is the principle quantum number of the level at which the atomic energy levels become a continuum for free electrons, and a_n is the characteristic radius of the beginning of the continuum [12]. Different IPD models calculate different values for a_n depending on the plasma conditions.

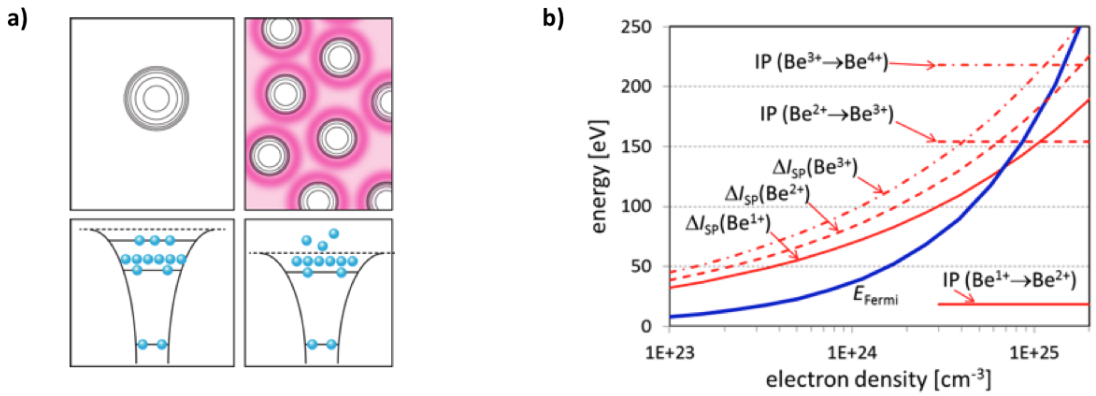

Figure 2.1: a) A cartoon schematic of continuum lowering. The left side shows the electron energy levels for an isolated atom, and the right side shows electron energy levels for a dense collection of atoms. In the case of the dense system, the continuum energy is lowered as a result of interactions between particles. Credit: APS/Alan Stonebraker. Adapted from [82]. b) A plot of energy versus electron density showing the effects of ionization potential depression in beryllium at 0 K. The blue line represents the Fermi energy and scales as $n^{2/3}$. The red dashed lines on the right side represent the ionization potential of different ionization states of beryllium. The red curves represent the change in ionization potential of different states of beryllium as predicted by the Stewart-Pyatt model [83].

The two simplest IPD models use one of the two natural plasma length-scales: either the ion sphere radius, R_0, or the Debye shielding length, λ_D. The ion sphere radius is used in the case of a high density plasma, in which inter-particle correlations are high and the spatial electron distribution is constant within a single ion sphere. The ion sphere radius is defined by [2]:

$$\frac{4\pi}{3} R_0^3 n_i = 1 \ , \tag{2.15}$$

where n_i is the ion density. We set $a_n = R_0$ to obtain the ion sphere IPD model [2]:

$$\Delta I_{Ion\ Sphere} = \frac{Z^* e^2}{2} \left(\frac{4\pi n_i}{r} \right)^{\frac{1}{3}} \ . \tag{2.16}$$

In the case that the plasma is low density and has many particles per Debye sphere, the Debye shielding length is used for a_n. The energy offset is then calculated by the Debye-Hückel model for IPD, which reads [12]:

$$\Delta I_{Debye-H\ddot{u}ckel} = \frac{Z^* e^2}{2\lambda_D} \ . \tag{2.17}$$

The Debye-Hückel model is only valid up to a density in which the coupling parameter $\Gamma = 1$, or when correlations begin to affect the plasma's behavior. Correlations become important at an ion density of $n_i \sim 8 \times 10^{28} T(\text{keV})/Z^{*2}$ [12].

The Stewart-Pyatt model [83] interpolates between the two regimes of low and high density. In that case, the IPD model gives:

$$\Delta I = \frac{Z^* e^2}{2} \frac{3}{2\lambda_d} \frac{(R_0^3/\lambda_D^3 + 1)^{2/3} - 1}{R_0^3/\lambda_D^3} \ . \tag{2.18}$$

Stewart-Pyatt is the most commonly used IPD model in radiation hydrodynamic codes. However, Stewart-Pyatt fails to account for electron screening cloud effects, which occurs as the inner electrons screen the outer electrons from the full nuclear charge [2]. Thus, none of these simple models fully capture the physics of IPD in warm dense matter and more work is needed to investigate the effects of continuum lowering.

2.2.3 Other Ionization Models

The previous discussion on the Saha equation and the IPD models assumed that the electrons obeyed Maxwell-Boltzmann statistics. This is a good assumption if the temperature of the electrons is much greater than the Fermi temperature, but in the case of warm dense matter, the temperatures are similar to or lower than the Fermi temperature, which means the electrons are often partially degenerate. In this case, a Maxwell-Boltzmann description of electron behavior is incomplete and the electrons must also be described by Fermi-Dirac statistics.

Another model for ionization, the Thomas-Fermi model, self-consistently treats electrons as fermions and combines that description with the ion sphere model [2, 41, 84].The Thomas-Fermi model solves Poisson's equation for the electric potential within the R_0 of the ion sphere, assuming the electron density is given by that of a classical electron gas. In this case, ionization is defined as [12]:

$$Z = \int n(r) d^3 r \ , \tag{2.19}$$

where the electron distribution $n(r)$ is given by [12]:

$$n(r) = \frac{4}{\sqrt{\pi}} \frac{1}{\lambda_D^3} F_{1/2} \left(\frac{e\Phi(r) + \mu}{k_B T} \right) \ , \tag{2.20}$$

where $F_j(r)$ is the Fermi-Dirac integral of order j, $\Phi(r)$ is the electrostatic potential within the sphere, and μ is the chemical potential. The electrostatic potential may then be solved for with the following differential equation [12]:

$$\frac{1}{r} \frac{d^2}{dr^2} [r\Phi(r)] = \frac{4}{\sqrt{\pi}} \frac{1}{\lambda_D^3} F_{1/2} \left(\frac{e\Phi(r) + \mu}{k_B T} \right) \ . \tag{2.21}$$

In practice, Z and the potential must be solved for numerically. However, in the case of zero temperature there is an analytic solution, which can be written as:

$$Z = Z^* \frac{y}{1 + y + \sqrt{1 + 2y}} \ , \tag{2.22}$$

where $y = \alpha(\rho/Z^*A)^\beta$, $\alpha = 14.3139$, and $\beta = 0.6624$ [12]. This equation at zero temperature shows that the ionization state increases with density, as the Thomas-Fermi model accounts for density-related effects of ion-ion correlations and degeneracy pressure. Increasing the temperature also affects the solutions to the ionization state as the electron distribution in Equation 2.20 changes to reflect the higher temperatures.

The Thomas-Fermi model is able to capture the physics of pressure ionization by forcing the electron density to equal zero at the ion-sphere radius; this means any electrons with radii higher than the ion-sphere radius are considered ionized. However, the Thomas-Fermi model has significant limitations, as it doesn't account for the shell-structure of the atom, is not relativistic, and is only strictly correct in the limit of infinite nuclear charge [12]. The Thomas-Fermi model is notoriously bad at predicting the ionization states of low-Z and partially ionized materials as it assumes a continuous electron density function and thus calculates continuous and smooth ionization.

A model that does include shell effects is the hydrogenic average-atom model [12, 85, 86]. The precise details of the ionization state calculation are beyond the scope of this thesis, but the calculations derive from several key model components. The three components are: 1) screening theory based on WKB[1] calculations, 2) Hartree-Fock approximations that average over shell populations, and 3) NLTE rate equations to calculate the average shell populations [12].

Figure 2.2 shows a plot of ionization levels of gold (Au[79]) versus temperature at a density of $\rho = 0.1$ gcm^{-3}, calculated by Gupta et al. [87] for three different ionization models (the NLTE model follows a similar formalism to the average-atom model discussed above). The two models that contain shell effects, Saha and NLTE, show ripples in the ionization versus temperature, whereas the Thomas-Fermi model shows a smooth ionization curve. The predictions for ionization vary widely between ionization models, as shown in Figure 2.2. Because ionization affects the equation of state and the behavior of materials, much more experimental validation of ionization models is needed in all regimes of temperatures and densities.

2.3 Shock Physics and the Rankine-Hugoniot Relations

Shock waves are often used to generate HEDP conditions in the laboratory to benchmark different equation of state and ionization models as a shock front traveling through a material can reach high pressure states. A shock wave involves an abrupt transition of fluid properties across a boundary [2] and results from the hydrodynamic properties of the material. In order to generate a shock, a dynamic pressure is applied to a material causes an acceleration. The acceleration launches a compression wave, which propagates at the material's ambient

[1]The WKB method is a method used to approximate the solutions to partial differential equations and stands for WentzelKramersBrillouin.

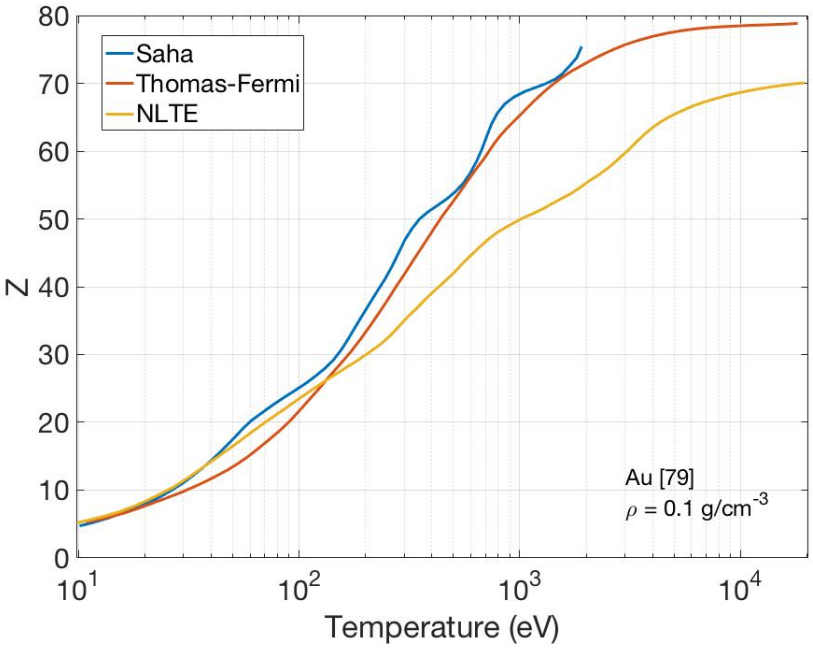

Figure 2.2: Au ionization versus temperature as calculated by three different ionization models. The Saha and NLTE models account for the shell structure of the atom, and so show ripples in the calculated ionization state as a function of temperature. The Thomas-Fermi model does not account for shell effects and shows a smooth ionization curve. Adapted by permission from RightsLink Permissions Springer Customer Service Centre GmbH: Springer Nature Pramana (Gupta, N.K. and Godwal, B.K. Pramana - J Phys (2002) 59: 33. https://doi.org/10.1007/s12043-002-0031-6), Copyright Indian Academy of Sciences (2002).

sound speed. Within the compression wave, the sound speed increases due to the increased density, and successive shock waves travel faster through the compressed regions and catch up to earlier shock waves to form what is known as a shock front [12]. In practice, almost all laboratory HED experiments launch shock waves into materials to generate extreme conditions. The following sections will outline how shocks are generated and characterized.

2.3.1 Laser-Driven Shocks

Lasers efficiently drive shocks into materials, making them ideal tools to generate shock-compressed matter in the laboratory. There are two primary methods for generating shocked material: direct- and indirect-drive, the fundamentals of which were discussed in Section 1.1.4. In a direct-drive platform, such as on the OMEGA laser, an ultraviolet laser impinges on a solid target with intensities ranging from $10^{13} - 10^{16}$ Wcm^{-2}. The laser deposits energy into the target and generates a variety of HED states as the outer surface heats and ablates. The states can be categorized into three regimes: a collisionless/classical plasma in the outer

corona, a collisional plasma farther into the material, and finally a degenerate plasma. Most of the laser energy is absorbed into the hot corona, in which the atoms are partially or completely ionized. Because the photon energy is low compared to the ionization potentials of the electrons in the atom, the light's behavior is dictated by interactions with free electrons in a process called inverse bremsstrahlung [12].

In an inverse bremsstrahlung process, photons from the lasers give energy to free electrons. The laser is an electromagnetic wave that generates a net current from the oscillating electric field within the plasma. Collisions between the ions and electrons damp the wave, which eventually reaches a depth at which the frequency of oscillations equals that of the plasma frequency, $w_p = (ne^2/\epsilon_0 m)^{1/2}$. At that point, the oscillating electrons oscillate at the frequency of the light and form an ostensible mirror [2]. That surface is called the critical surface. Solving for the density at which that occurs, one obtains the critical density equation:

$$n_c[\mathrm{cm}^{-3}] = 1.1 \times 10^{21}/\lambda_{\mu\mathrm{m}}^2 \ , \tag{2.23}$$

where $\lambda_{\mu\mathrm{m}}$ is the wavelength in microns [2]. After the critical surface, the laser deposits any remaining energy into the collisional plasma through resonance absorption, where the electromagnetic wave couples with a longitudinal plasma wave. The light that doesn't participate in resonance absorption is reflected back, and undergoes inverse bremsstrahlung processes again.

Direct-drive implosions generate a substantial amount of hot electrons from inverse bremsstrahlung interactions. The hot electrons carry energy beyond the critical surface and deeper into the dense plasma; the ablation front then occurs in this higher-density regime rather than at the critical surface itself. The deposition of energy up to the ablation-front results in an ablation pressure applied to the plasma. We can estimate the ablation pressures generated in direct-drive experiments by considering how electrons heat material. A simple model used to describe electron heating is flux-limited transport. This model derives from the idea that the maximum possible energy flow occurs when the thermal energy density in the plasma moves at the thermal velocity v_{th}, which generates a free-streaming heat flux of $n_e k_B T v_{th}$ [2]. However, since this is the maximum heat transport, it is often necessary to add a factor called the flux-limiter, f to the equation. Then, the free-streaming heat flux can be written as [2]:

$$Q_{FS} = f n_s k_B T_e v_{th} \ . \tag{2.24}$$

In a typical physical system, $f = 0.1$ [2]. Assuming that $n_e \sim n_c$ beyond the critical surface, and that roughly half of the intensity of laser light transports through the critical surface, we write [2]:

$$0.5 I_L = f n_c k_b T_e \sqrt{\frac{k_B T_e}{m_e}} \ , \tag{2.25}$$

and then solve for T_e with the assumption that $f = 0.1$:

$$T_e[\mathrm{keV}] = 1.7 (I_{14} \lambda_{\mu\mathrm{m}}^2)^{\frac{2}{3}} \ , \tag{2.26}$$

where I_{14} is the laser intensity in 10^{14} Wcm^{-2}. We now estimate the ablation pressure by setting the ablation pressure equal to the outward momentum flux carried by the heated electrons. Assuming that the flow occurs at $\sqrt{2}$ the sound speed (for simplicity of calculation) we can write [2]:

$$P_{abl} = 2M\sqrt{\frac{Zk_BT_e + 3k_BT_i}{M}} \times \frac{n_c}{M}\sqrt{\frac{Zk_BT_e + 3k_BT_i}{M}} \, , \tag{2.27}$$

where M is the Mach number and T_i is the ion temperature. With the assumption that $T_i = T_e/3$, which is reasonable for the coronal area, we derive a simplified expression for the ablation pressure [2]:

$$P_{abl} = 2n_ck_BT_e\frac{Z+1}{Z} \, . \tag{2.28}$$

Finally, by assuming $Z = 3$, we can write the ablation pressure as [2]:

$$P_{abl}[\text{Mbar}] = 8.0I_{14}^{\frac{2}{3}} \, \lambda_{\mu\text{m}}^{-\frac{2}{3}} \, . \tag{2.29}$$

This means that in a typical direct-drive facility such as OMEGA, a 0.35 µm wavelength and 10^{15} Wcm^{-2} drive generates ablation pressures on the order of 75 Mbar, which is equivalent to the pressure at the center of Jupiter [2].

Indirect-drive experiments use laser light to generate shocks in materials through the conversion of laser-light to x-rays in a hohlraum. In the case of the NIF, lasers deposit UV light into a high-Z hohlraum that surrounds a capsule. The heated hohlraum generates a near-uniform x-ray bath at the center of the hohlraum, which heats the sample at the center and generates an ablation pressure and a shock wave. An ideal hohlraum emits radiation like a black body, and the total flux in the cavity can be written as:

$$S[\text{TWcm}^{-2}] = 10T_r^4 \, , \tag{2.30}$$

where S is the flux and T_r is the radiation temperature in 100's of eV. A hohlraum must be heated to 250 - 300 eV to obtain the necessary flux of 500-1000 TW cm^{-2} for ignition [41].

Hohlraums convert laser light to x-rays with 70-80% efficiency [41], but the process is multi-faceted and complex. The first step in conversion occurs in the region of interaction between the laser spots and the hohlraum walls. The laser energy is absorbed through inverse bremsstrahlung process, which ionizes the Au and heats the electrons. The hot electrons excite the partially ionized ions, which then emit x-rays. The x-rays heat and ionize the surrounding cold Au material. Because the optical depth of the ionized Au is low, slightly more than half of the x-rays radiate inwards to heat cold material, and less than half give energy to expanding Au plasma and hot electrons, which also serve to heat the surrounding Au [2]. The radiation past the spots of direct laser irradiance forms a Marshak wave, which is a type of wave that occurs at the boundary between a cold material and a hot material with a constant-temperature energy source. The Marshak wave describes how diffusion of

radiation heats cold material. The depth of a Marshak wave in a hohlraum can be estimated by:

$$x_M[\mu\text{m}] = 0.53 T_0^{1.86} t_{ns}^{0.75} \ , \tag{2.31}$$

where x_M is the depth of the Marshak wave in microns, T_0 is the temperature of the hot material at 1 ns in 100's of eV at the boundary of the hot and cold regions, and t_{ns} is the time in nanoseconds [2, 49]. Equation 2.31 shows that the Marshak wave is only on the order of microns for most hohlraum experiments and that the efficiency of a hohlraum increases with time, as less power is required to sustain the wave.

The laser spots on the hohlraum walls also emit x-rays that further interact with the remainder of the hohlraum walls, because the hohlraum is a closed cavity. That means that every spot that generates x-rays heats the opposing wall with those x-rays. Considering that some of emitted radiation is also reabsorbed, one can arrive at an estimate for the wall temperature in eV as [2]:

$$T_w = \left(\frac{\eta f A_L A_W}{\sigma(1-\alpha f)} I_L \right)^{\frac{1}{4}} \ , \tag{2.32}$$

where η is the x-ray conversion efficiency, A_L and A_W are the areas of the laser spots and the hohlraum walls, f is the fraction of emission from the laser spots that reaches the other walls, and α is the albedo (the fraction of radiation that is incident on a wall which is re-emitted by the wall). Put in simpler units, we can estimate the wall temperature to be [2]:

$$T_w[\text{eV}] = 177 (\xi I_{14})^{\frac{1}{4}}. \tag{2.33}$$

Typical values for these parameters are $\eta \sim 0.7$, $f \sim 0.9$, and $\alpha \sim 1$ [2]. f is near unity because the only fraction of the x-rays that doesn't reach opposing walls is the fraction that exits through the hohlraum's laser entrance holes, which are typically small compared to the total inner surface area of the hohlraum. α is near unity because often many more x-rays are re-emitted than absorbed in the high-Z material. A good approximation for the ratio of laser spot area to hohlraum wall area is $A_L \sim 0.1 A_W$. Thus, we find that ξ is often on the order of unity as well.

The hohlraum emission spectrum has three main components: a lower-temperature black body component governed by the radiation temperature, a higher temperature non-equilibrium component from the hot, under-dense plasma region expanding from the hohlraum walls, and gold M-shell emission around 2 keV. The black-body spectrum contributes the most to the generation of the ablation front as the low energy x-rays efficiently deposit their energy into the low-Z ablator materials; typical values for the radiation temperature on the NIF range from 200-300 eV [88]. If we assume that half the x-ray energy contributes to ablation pressure, we estimate the ablation pressure as [2]:

$$P_{abl} = 0.5(\gamma - 1)\sigma T_w^4 \sqrt{\frac{A m_p}{(Z+1)} k_B T_w} \ , \tag{2.34}$$

where γ is the adiabatic index. In the coronal region, $\gamma = 5/3$. In the case that the ablator is beryllium, we find the following expression for the ablation pressure [2]:

$$P_{abl}[\text{Mbar}] = 4.4 \left(\frac{T_w}{100 \text{ eV}} \right)^{\frac{7}{2}} . \tag{2.35}$$

On the NIF, a hohlraum temperature of 300 eV generates an ablation pressure on the order of $P_{abl} = 100$ Mbar [38]. This is a similar value to the pressures generated by direct-drive implosions.

2.3.2 Efficiency of Laser-Generated Shocks

Material that ablates away acts like a rocket engine; by conservation of momentum, the unablated mass must accelerate in the opposite direction. Both directly- and indirectly-driven shocks result from ablation pressures, but the methods of generating ablation pressures vary greatly between the two techniques. In this section, we asses the efficiency of direct- and indirect-drive techniques by solving the classic rocket engine problem as follows.

A rocket of mass $m+\Delta m$ moves through vacuum with velocity v_i. After the rocket burns a fuel mass of Δm in time Δt, the rocket has a velocity $v_i + \Delta v$ and the the burnt fuel moves with a velocity of v_{ex} relative to the rocket. The equation for conservation of momentum before and after the fuel is burnt can be written as [89]:

$$(m + \Delta m)v_i = m(v_i + \Delta v) + \Delta m(v_i - v_{ex}) . \tag{2.36}$$

We solve the equation for Δv to obtain:

$$\Delta v = v_{ex} \frac{\Delta m}{m} . \tag{2.37}$$

Assuming that the fuel Δm is burned in Δt and dm is negative, we can we write the equation in terms of time derivatives and solve the differential equation to obtain the rocket equation:

$$v_f - v_i = v_{ex} \ln \frac{m_i}{m_f} , \tag{2.38}$$

where m_i and m_f are the initial and final masses of the rocket [89]. We can then solve for the efficiency, e_R, of the rocket, which is defined as the ratio of kinetic energy of the remaining rocket mass to the total kinetic energy of exhausted fuel and remaining mass. The ablation efficiency reads:

$$e_R = \frac{m_f v^2}{m_f v^2 + 2K_{ex}} , \tag{2.39}$$

where K_{ex} is the kinetic energy of the exhausted fuel [2]. After solving for the kinetic energy of the fuel by integrating over the lost mass, we find the rocket engine efficiency to be [2]:

$$e_R = \frac{(m_f/m_i) \ln {m_f/m_i}^2}{1 - (m_f/m_i)} . \tag{2.40}$$

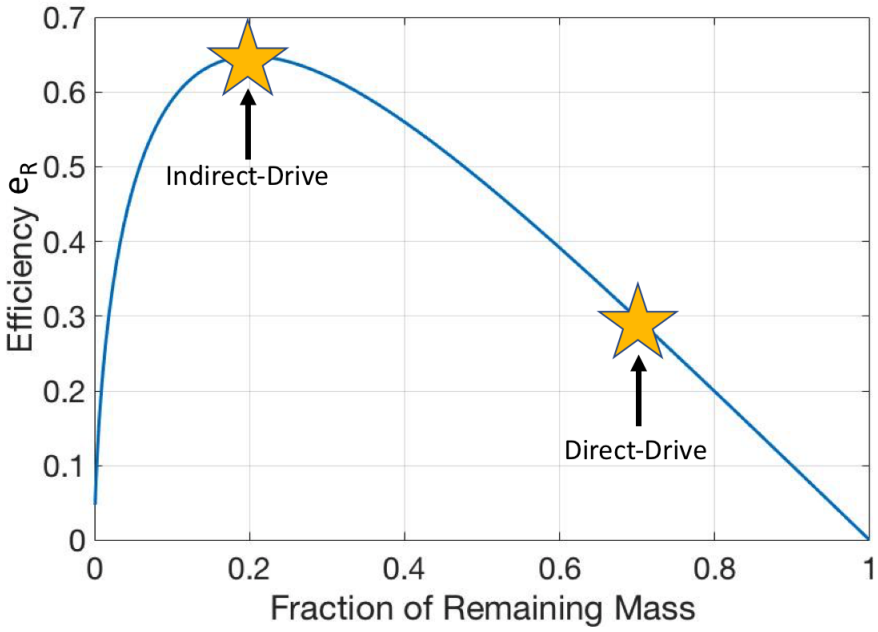

Figure 2.3: Rocket engine efficiency, ϵ_R, versus fraction of remaining mass, m_f/m_i. An indirect-drive implosion works in the regime of maximum efficiency with 20% of the mass remaining. Direct-drive implosions are less efficient at generating shock waves, as they operate in the regime with 70% of the mass remaining.

Figure 2.3 shows a plot of ϵ_R as a function of remaining mass, with arrows indicating the regimes in which direct- and indirect-drive experiments operate. Laser light from direct-drive experiments is absorbed in low density plasmas, whereas the x-rays from indirect-drive experiments are absorbed further into the material, in higher-density regions. Thus, indirect-drive platforms generate higher ablation pressures for a given laser drive intensity. Even though indirect-drive leads to more efficient ablation and higher ablation pressures, the coupling efficiency with the laser is still lower than it is in the direct-drive case. The lower coupling efficiency of indirect-drive amounts to a final fusion energy gain of only double that from a direct-drive implosion [35, 90]. Thus, both direct-drive and indirect-drive platforms are still used to generate shocks in materials to probe the properties of high energy density material in the laboratory.

2.3.3 The Rankine-Hugoniot Relations

An ablation pressure generates HEDP conditions by launching a shock wave into a material. The progression of the shock wave and the conditions behind the shock front depend on the equation of state of the compressed material. Thus, many experiments measure the shock propagation and shock front conditions as a way to characterize the equation of state [91].

As a shock propagates through a material, there is a discontinuity in conditions between

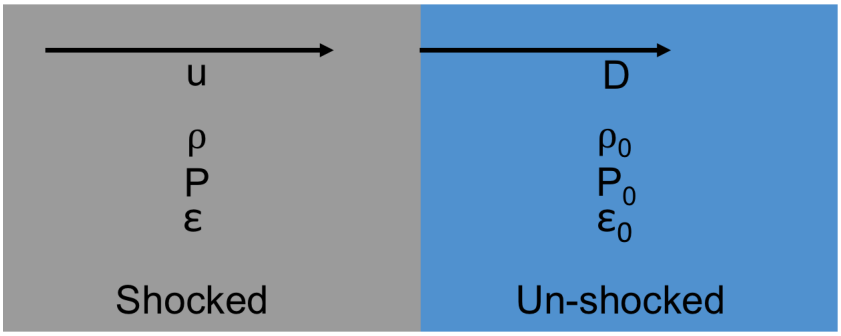

Figure 2.4: A schematic of a shock front traveling at velocity D in a material; the grey portion represents the shocked material and the blue portion represents the unshocked material. The unshocked material has an initial density and pressure of ρ_0 and p_0, and the shocked material has density and pressure ρ and p. u is the jump in particle velocity across the shock front.

the cold, unshocked material and the hot and dense shock front. The Rankine-Hugoniot relations, often referred to as the shock Hugoniot, describe the change in conditions over the boundary of the shock front. Figure 2.4 shows a schematic of a shock wave as it travels through material. The shock front travels with velocity D, and u represents the jump in particle velocity across the shock front. The unshocked material has initial density, pressure, and energy ρ_0, p_0, and ϵ_0, and the shocked material has density, pressure, and energy ρ, p, and ϵ. The Rankine-Hugoniot relations conserve momentum, mass, and energy across the shock front. The following derivations follow the method of Reference [91].

By the conservation of momentum across the shock front, we obtain the equation:

$$p - p_0 = \rho_0 D u \ . \tag{2.41}$$

Conservation of mass gives:

$$\rho_0 D = \rho(D - u) \ , \tag{2.42}$$

and conservation of energy gives:

$$\epsilon - \epsilon_0 = \frac{1}{2}(p - p_0)\left(\frac{1}{\rho_0} - \frac{1}{\rho}\right) \ . \tag{2.43}$$

In solids, $p_0 \ll p$, so we assume $p_0 = 0$. ϵ_0 is the thermal energy associated with the lattice vibrations of the solid, which is, in principle, tabulated and known [91]. That then leaves three equations and five unknowns, namely: ϵ, p, D, u, and ρ. Thus, measuring any two variables allows one to solve for the entire equation of state. This is the power of the Hugoniot relations: one only needs to measure two variables to solve for all five. For example, in the case that one measures ρ and D, the equations can be rewritten to solve for pressure in the shock front as a function of density and shock speed as:

$$p = \frac{\rho_0}{\rho}(\rho - \rho_0)D^2 \ . \tag{2.44}$$

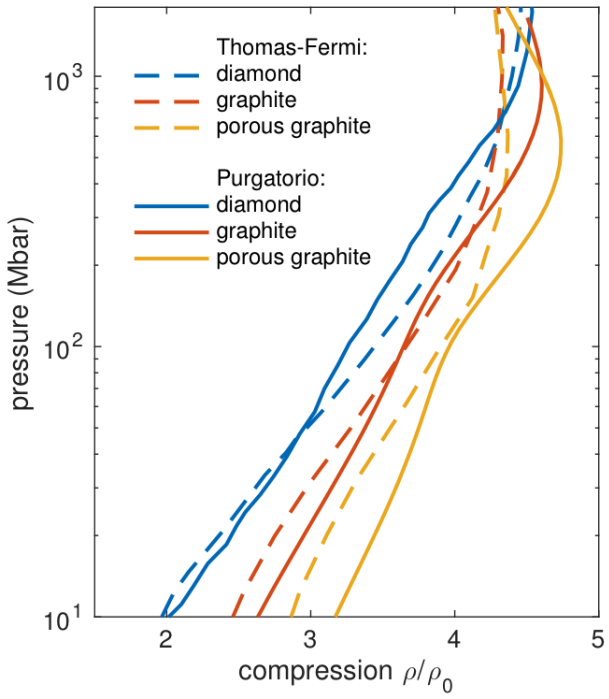

Figure 2.5: Calculated shock Hugoniot curves for three different initial densities of carbon: diamond at $\rho_0 = 3.5$ gcm^{-3} (blue), graphite at $\rho_0 = 2.3$ gcm^{-3} (red), and porous graphite at $\rho_0 = 1.0$ gcm^{-3} (yellow). The plot shows how the shape of the Hugoniot changes with different equation of state models. The Thomas-Fermi model (dashed lines) shows smooth compression curves, whereas the average-atom Purgatorio model [92] shows the effects of atomic shell structure through slight wiggles; instead of assuming a smooth function of ionization, each shell requires a different amount of energy to ionize. It is worth noting that even though the ρ/ρ_0 compression reached by all materials is similar, the materials with higher starting densities allow for reaching much higher densities in the shock fronts at peak compression; shock fronts in diamond can reach densities of 14 g cm^{-3} whereas shock fronts in porous graphite can only reach densities of 4 g cm^{-3}.

In practice, the Hugoniot is a useful framework for understanding how materials in extreme conditions respond to pressure. The shape of the Hugoniot curve through pressure-density space depends on the EOS, so measuring the shock Hugoniot benchmarks EOS models. Figure 2.5 shows a plot of Hugoniot pressure versus compression (ρ/ρ_0) for carbon at three different initial densities (represented by the different colors) for two different EOS models: Thomas-Fermi [84] and the average-atom model, Purgatorio [92].

The primary difference to note between curves is the shape at higher compressions. The average atom curves have additional structure due to the atomic shell structure. When the pressure becomes high enough to free the electrons in a specific shell, more energy goes into internal energy [2]. The density then increases more for a given pressure, and the Hugoniot curve "softens." This effect is seen around 100 Mbar in Figure 2.5. Once ionization is complete, less of the energy in the shock front converts to internal energy, and the Hugoniot curve "hardens," as seen around 1 Gbar in Figure 2.5. The Thomas-Fermi curve is smooth through all states as the Thomas-Fermi does not contain the physics of atomic shell structure. Thus, mapping out the shape of the Hugoniot provides information on the onset of ionization in materials, as well as the material's compressibility at high pressures.

Overall, HED experiments seek to measure plasma properties and equation of state variables in these dynamic compression experiments. The following chapter will describe the basic theory and methodology of several important measurement techniques, as well as an experimental platform that can be used to measure the Hugoniot.

Chapter 3

Measuring Equation of State Variables in High Energy Density Matter

3.1 Diagnostics for Plasma Conditions in Warm Dense Matter

Chapter 2 defined the equation of state and outlined the challenges of predicting equation of state variables in materials at high energy density conditions. This chapter will outline the theory of several techniques used to measure conditions in highly compressed materials where optical techniques like VISAR are no longer capable of making measurements due to the extreme densities. Both high energy x-rays and neutron diagnostics are capable of penetrating into high densities, making them ideal probes for HEDP conditions.

3.1.1 X-ray Thomson Scattering

One powerful tool for probing the conditions of warm and hot dense matter is x-ray Thomson scattering (XRTS). An XRTS experiment scatters a narrow energy band of x-rays off of a plasma sample and then collects the frequency-resolved scattered power spectrum at a specified scattering angle. Since the photons scatter from electrons, XRTS probes the physics of the electrons in the system, which can reveal many plasma properties, such as electron temperature, density, ion-ion correlations, and ionization states [62]. Here I present the basic theory and techniques of XRTS.

Thomson scattering itself refers to the process of a photon scattering elastically from an electron. More specifically, Thomson scattering refers to the process of an electron oscillating and emitting radiation in response to an applied electric field. For the simplicity of the initial derivation, we assume that a linearly polarized electric field of frequency ω_0 and strength E_0, with oscillating velocity less than the speed of light ($h\nu \ll mc^2$), is incident on a free

electron. We can write the force on the charge due to the electric field [93] as:

$$\vec{F} = m\ddot{\vec{r}} = eE_0 \sin\omega_0 t\hat{\epsilon} \ , \tag{3.1}$$

where m is the mass of the electron, $\vec{r}$ is the position vector, e is the charge of the electron, and $\hat{\epsilon}$ is the direction of the electric field. Using the expression for the electric dipole, $\vec{d} = e\vec{r}$, we find a differential equation for $\vec{d}$ [93]:

$$\ddot{\vec{d}} = \frac{e^2 E_0}{m} \sin\omega_0 t\hat{\epsilon} \ , \tag{3.2}$$

and then solve the differential equation for $\vec{d}$ to obtain [93]:

$$\vec{d} = -\left(\frac{e^2 E_0}{m\omega_0^2}\right) \sin\omega_0 t\hat{\epsilon} \ . \tag{3.3}$$

The dipole approximation allows us to estimate the radiated power per solid angle as [93]:

$$\frac{dP}{d\Omega} = \frac{e^4 E_0^2}{8\pi m^2 c^3} \sin^2\theta \ , \tag{3.4}$$

where $c = 3 \times 10^8 \ \mathrm{m\,s^{-1}}$ is the speed of light in vacuum and θ is the scattering angle. The incident flux on the sample is the average of the Poynting vector: $\langle\vec{S}\rangle = (c/8\pi)E_0^2$. We can then rewrite the scattered power in terms of the scattering cross section σ [93]:

$$\frac{dP}{d\Omega} = \langle S\rangle \frac{d\sigma}{d\Omega} = \frac{cE_0^2}{8\pi}\frac{d\sigma}{d\Omega} \ . \tag{3.5}$$

With Equation 3.4, we find that:

$$\left(\frac{d\sigma}{d\Omega}\right)_{polarized} = \frac{e^4}{m^2c^4} \sin^2\theta = r_0^2 \sin^2\theta \ , \tag{3.6}$$

where we define $r_0 \equiv e^2/mc^2$ as the classical electron radius [93]. To find the total cross section, we can integrate over the full solid angle to obtain what is know as the Thomson scattering cross section, or σ_T [93]:

$$\sigma_T = \frac{8\pi}{3} r_0^2 \ . \tag{3.7}$$

For electrons, $\sigma_T = 0.655 \times 10^{-24} \ \mathrm{cm^2}$. Equation 3.6 can be extended to unpolarized light by averaging over linearly polarized light of angles 0 and $\pi/2$. The result is then [93]:

$$\left(\frac{d\sigma}{d\Omega}\right)_{unpolarized} = \frac{1}{2} r_0^2 (1 + \cos^2\theta) \ . \tag{3.8}$$

If the initial photon is of sufficiently high energy ($h\nu \sim mc^2$), the scattering cross section can also depend on the energy of incoming photons, at which point the actual quantum

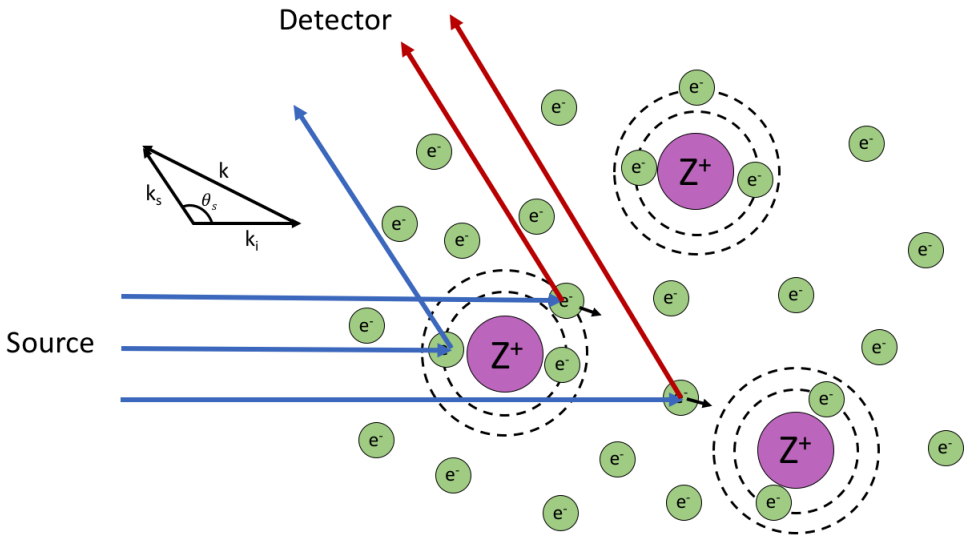

Figure 3.1: A cartoon schematic of x-ray Thomson scattering. Incoming photons can scatter elastically from electrons that are tightly bound to the ionic core. Photons scatter inelastically from free electrons and from loosely bound electrons. These three processes can be described as bound-bound, bound-free, and free-free scattering, respectively.

mechanical cross sections must be used. Thomson scattering is also referred to as coherent scattering, as the emitted photon maintains the same frequency as the incoming photon.

One type of incoherent scattering that can happen when a photon is of sufficiently high energy is Compton scattering. In this case, a photon impinges on an electron, imparting momentum. In practice, Compton scattering can be thought of akin to a relativistic billiards ball momentum transfer problem. Let's first assume the electron is at rest and a photon with an initial wavelength λ_i scatters off of the stationary electron. The photon imparts some momentum to the electron, which then carries its own momentum. The typical relativistic momentum conservation equations can be solved to obtain the wavelength shift of the photon:

$$\lambda_s - \lambda_i = \frac{h}{mc}(1 - \cos\theta) \ , \tag{3.9}$$

where λ_s is the scattered wavelength and θ is again the scattering angle [93]. The Compton wavelength is defined as $\lambda_C \equiv h/mc$, and equals 0.024624 Å for electrons.

Another type of incoherent scattering occurs when a photon photoionizes a loosely bound electron. In that case, the bound electron experiences a force due to the applied electromagnetic field while under the central field force of the nucleus. This adds a frequency-dependent adjustment factor to the Thomson scattering cross section. The cross section for scattering from bound electrons becomes:

$$\sigma_{bound} = \frac{8\pi}{3} r_0^2 \frac{\omega_0^4}{(\omega_0^2 - \omega_e^2)^2 + (\gamma\omega_0)^2} \ , \tag{3.10}$$

where ω_e is the resonant frequency of the oscillator force imposed by the central field and γ represents a dissipative force that accounts for energy loss [94]. The cross section is the largest when the incoming photon is on resonance with the oscillator force, or if $\omega_0 \sim \omega_e$. In that case, the cross section is considerably higher than that of the case of scattering from a free electron. In the high frequency limit of $\omega_0 \gg \omega_e$, the photon scatters as if it were scattering from a free electron. In the low frequency limit of $\omega_0 \ll \omega_e$, we return the classical Rayleigh scattering cross section of [94]:

$$\sigma_R = \frac{8\pi}{3} r_0^2 \left(\frac{\omega_0}{\omega_e}\right)^4 , \tag{3.11}$$

which of course explains why the sky is blue due to the strong frequency dependence (although, it does not explain why the sky is not purple.)

XRTS involves both Thomson and Compton scattering phenomena, but it is simply referred to as x-ray Thomson scattering. Figure 3.1 shows a cartoon schematic of an XRTS process in which x-rays impinge on a plasma sample and then scatter to a detector at a scattering angle, θ. X-rays scatter elastically from inner-shell electrons that are tightly bound to the ionic core and inelastically from free or loosely bound electrons, as seen in Figure 3.1. In free-free scattering, the photon transfers an average momentum to the electron of $h\vec{k}$, where $\vec{k}$ is the scattering vector. In the nonrelativistic limit, we approximate the magnitude of $\vec{k}$ as:

$$k \equiv |\vec{k}| = 4\pi \frac{E_0}{hc} \sin\theta/2 \tag{3.12}$$

where E_0 is the energy of incident radiation [95]. We can then define the Compton energy, E_C in terms of the scattering vector [95]:

$$E_C = \frac{\hbar^2 k^2}{2m} = \hbar\omega_i - \hbar\omega_s , \tag{3.13}$$

where ω_i and ω_s are the frequencies of incident and scattered light, respectively. The dimensionless scattering parameter, α, describes whether XRTS will probe individual electron effects or collective electron effects. We define the scattering parameter as [62]:

$$\alpha = \frac{1}{k\lambda_s} , \tag{3.14}$$

where λ_s is the screening length. In the case of non-degenerate plasmas, we can take λ_s as the Debye screening length, and in degenerate plasmas, is becomes the Thomas-Fermi screening length. The correct screening length can be determined by the previously introduced degeneracy parameter, Θ; the Thomas-Fermi screening length should be used if $\Theta \leq 1$ [95]. The work in this thesis will only include scattering in which $\alpha < 1$, in which the scattering spectrum reflects non-collective motion of the electrons.

We can now extend Equation 3.8 to the case of scattering multiple photons off of a diverse set of electronic states. In that case, the scattered power per unit frequency per solid angle

from unpolarized light can be written as:

$$\frac{dP}{d\Omega d\omega} = r_0^2 \frac{1}{2}(1+\cos^2\theta)\left(\frac{\omega_s}{\omega_i}\right)^2 N I_0 S(k,\omega)\ , \tag{3.15}$$

where N is the number of scatterers, I_0 is the intensity of incident radiation, and $S(k,\omega)$ is the total electron dynamic structure factor [62]. The structure factor is defined as the Fourier transform of the electron density correlation function [95]. This structure factor accounts for both elastic and inelastic scattering. The well-known Chihara decomposition [96] breaks the dynamic structure factor into three components, each component denoting bound-bound, free-free, and bound free scattering. The Chihara decomposition reads [96, 97]:

$$S(k,\omega) = |f(k)+q(k)|^2 S_{ii}(k,\omega) \ + \ Z_f S_{ee}(k,\omega) + Z_b \int S_{be}(k,\omega-\omega')S_s(k,\omega')d\omega', \tag{3.16}$$

where $f(k)$ is the ionic form factor, $q(k)$ is the electronic screening cloud contribution, S_{ii} is the ion density correlation function, Z_f is the ionization state, S_{ee} is the free-free dynamic structure factor, Z_b is the bound charge per atom, S_{be} is the form factor of bound electrons undergoing Raman-like transitions to the continuum, which is modulated by the self-motion of the ions, S_s. From left to right, the three terms represent the contributions from bound-bound, free-free, and bound-free scattering, respectively.

Free-free scattering occurs when x-rays scatter from free electrons. The Compton wavelength we derived previously assumed that the electron was initially at rest. In practice, the electrons are moving with a velocity distribution, $f(v)$, so a photon interacts with an electron in motion. In this case, the frequency shift of a scattered x-ray can be written as [62]:

$$\omega = -\frac{\hbar k^2}{2m} \pm \vec{k}\cdot\vec{v}\ . \tag{3.17}$$

The first term in Equation 3.17 accounts for the Compton shift and the second term accounts for the Doppler effect, as the photons interacts with a moving charge. Thus, free-free scattering probes the velocity distribution of the free electrons. In the case of a highly degenerate plasma, the velocity distribution depends primarily on the electron density, and in the case of a classical plasma, the velocity distribution is Maxwell-Boltzmann. In many cases of warm and hot dense matter, the plasma is weakly degenerate, and the velocity distribution depends on both temperature and density. Bound-free scattering is similarly broadened by the electron velocity distribution.

XRTS also offers the ability to probe the ionization state of the sample. Inelastic scattering occurs from electrons that are either free or loosely bound, and elastic scattering occurs from electrons that are tightly bound. Thus, the ratio of elastic and inelastic scattering scales with the ionization state. Elastic scattering depends on the ion-ion structure factor $S_{ii}(k)$, the ionic form factor $f(k)$, and the screening cloud contribution $q(k)$. At sufficiently high

k-values, both $S_{ii}(k)$ and $q(k)$ reach their ideal plasma values of 1 and 0, respectively. Elastic scattering is then sensitive to the ion form factor, which is simply the Fourier transform of the electron charge density around the nucleus. In that case, elastic scattering scales with Z^2.

Table 3.1 describes all terminology associated with the different components of an XRTS spectrum in order to characterize which terms are used interchangeably with each other in the literature and in this thesis.

Term	Description	Usage
Elastic Scattering	Elastic scattering refers to all x-rays that scatter elastically from electrons. This occurs when x-rays interact with electrons that are tightly bound to an ionic core and the photons are unable to impart significant momentum, thus leaving the electron's state unchanged. The strength of the elastic scattering signal scales with the ionic form factor, $f(k)$, the screening cloud contribution, $q(k)$, and the ion-ion structure factor, $S_{ii}(k)$.	"Elastic scattering" and "Rayleigh scattering" are often used interchangeably in the literature to describe the elastic scattering of x-rays.
Rayleigh Weight	Rayleigh scattering was originally defined by Lord Rayleigh as the primarily elastic scattering of electromagnetic radiation from the atmosphere. In terms of XRTS, the Rayleigh weight is defined as: $W_R(k) = [f(k) + q(k)]^2 S_{ii}(k)$ and refers to the total strength of elastic scattering in the Chihara decomposition.	The terms "elastic scattering strength" and "Rayleigh weight" are often used interchangeably in the literature to describe the relative amount of elastic compared to inelastic scattering.

Thomson Scattering	Thomson scattering refers to the elastic scattering of electromagnetic radiation from a charged particle. The theory behind Thomson scattering is based in classical electromagnetism; free electrons accelerate as a result of an incident electromagnetic wave, which then generates an electric dipole, which reradiates an electromagnetic wave. The process is considered to be elastic, as the electron state is left unchanged.	"Thomson scattering" is used to describe all contributions of an XRTS spectrum in this thesis and in the literature.
Inelastic Scattering	Inelastic scattering refers to the processes that result in photons imparting momentum to electrons; because the photons impart momentum, they scatter inelastically. The inelastic scattering portion of the scattering spectrum is comprised of photons that undergo free-free and bound-free scattering. The inelastic scattering peak is Doppler-broadened by the thermal motion of the plasma.	"Inelastic scattering" and "Compton scattering" are used interchangeably in the literature, as the two contributions to inelastic scattering typically overlap to form one inelastic peak.

Compton Scattering	Compton scattering refers to the inelastic scattering of a photon from a free electron and occurs in the limit that the photon energy is much higher than the binding energy of the electron. Compton scattering is a quantum mechanical phenomenon, as the photon must be treated like an incoming particle with a momentum that scales with the frequency. The Compton peak in an XRTS spectrum is centered at an energy of $E_0 - \hbar^2 k^2 / 2m_e$, where E_0 is the energy of incident radiation. The peak has a finite width due to the velocity distribution of the electrons.	Colloquially, the "Compton peak" in an XRTS spectrum refers to the entire peak of inelastic scattering.
Doppler Broadening	In XRTS, all three components of bound-bound, bound-free, and free-free scattering are broadened by the velocity distribution of the electrons; however, unless the plasma has a bulk speed comparable to the scattering energy, the Doppler broadening of the elastic peak is small enough to be ignored. The width imparted to the inelastic components is referred to as Doppler broadening. Because of the Doppler broadening, the width of the spectrum can be analyzed to return the velocity distribution of the electrons, and thus the electron temperature or density.	In XRTS literature, "Doppler broadening" typically refers to the broadening of a spectral feature due to the velocity distribution of the electrons.

Table 3.1: A table recounting the terms used to describe the different components of an XRTS spectrum. The third column describes the usage of the term in this thesis and in the relevant literature, and outlines the terms that are used interchangeably.

Figure 3.2 shows XRTS simulations from a beryllium target generated with the scattering simulation code, Multi-Component Scattering Simulations (MCSS). The simulations use a

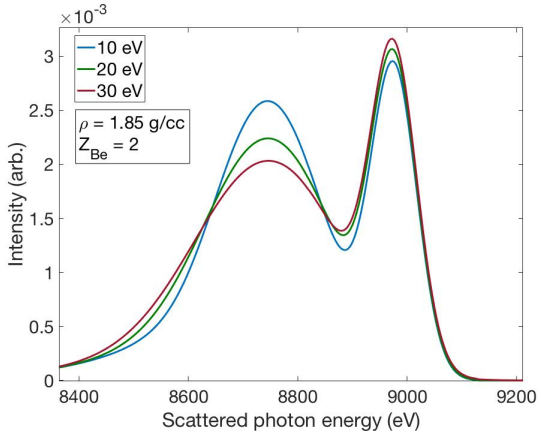

(a) Simulations varying T_e.

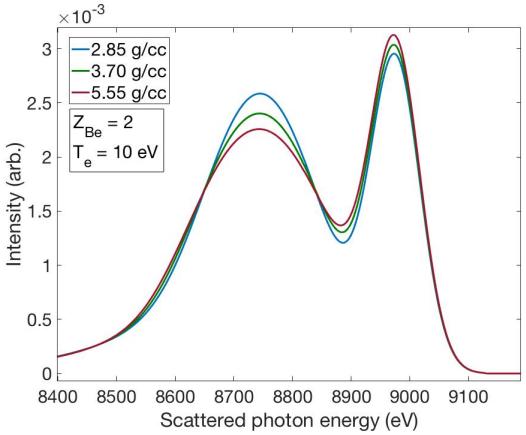

(b) Simulations varying ρ.

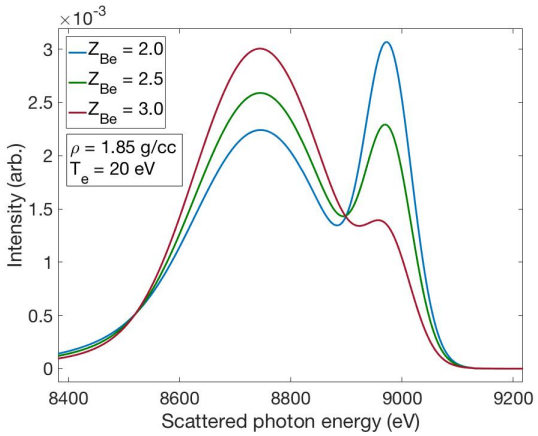

(c) Simulations varying Z_{Be}.

Figure 3.2: Simulations of XRTS spectra from a beryllium target generated with the Multi-Component Scattering Simulations Code [98]. All simulations assume a scattering angle of 120° and use a 100 eV FWHM Gaussian x-ray source centered around 8975 eV. The simulations show the sensitivity of scattering spectra to the various parameters.

100 eV FWHM Gaussian x-ray source centered at 8975 eV in order to mimic the Zn He-α source typically used, and assume a scattering angle of 120°. In the case of solid density beryllium at 1.85 g cm^{-3} with an ionization state of 2, the electron density is 2.5×10^{23} cm^{-3}, and the Fermi energy is 16 eV. Thus, the spectra show sensitivity to temperature and density. It should be noted that there is a significant trade-off to fitting both density and temperature, as often a good fit to a spectrum can be found for a given temperature and density, and then again for a different set of temperature and density values. However, the range of temperatures and densities for which good fits can be found is often bounded, both by physical limitations (e.g. the density of a compressed sample cannot be lower that solid density) and by fitting limitations; there is almost always a temperature and density that is too high or too low such that a good fit cannot be found. In addition, increasing temperature softens the red-most wing of the spectrum, whereas density tends to affect the FWHM of the inelastic peak. In practice, a spectrum that is being fit for temperature and density constrains one of the variables by simulations or other *a priori* knowledge. But in principle, an experiment can be designed such that the spectrum is more sensitive to one variable or the other (e.g. scattering spectra from Fermi degenerate matter will be more sensitive to density), which then better constrains the fitting, although limits the fitting relevance to only one variable.

Figure 3.2 also shows the sensitivity of scattering spectra to the beryllium ionization state. As the beryllium ionizes above $Z_{Be} = 2$, the elastic scattering decreases. Elastic scattering at 120° is less sensitive to ionization states below $Z_{Be} = 2$. This occurs because photons impart significant momentum to electrons when the photons are back-scattered, as they are in the case of 120° scattering; the large momentum transfer ionizes any electrons in the Be L-shell. In principle, elastic scattering in a forward-scattering geometry would remain sensitive to lower Be ionization states.

The use of inelastic scattering to determine electron properties such as temperature and density is well documented in previous work [60, 99, 100, 101]. In these experiments, plasmas are created through techniques like radiative heating or shock compression. Then, the shape of the elastic feature is fit to analytic models to determine plasma parameters. Experimenters have also used the shape of the bound-free feature to determine the ionization state and to constrain continuum lowering models [4]. There has also been forward scattering work that analyzes the plasmon shape to return density of the sample with high accuracy [6, 102]. Much recent work has focused on the information found from the elastic scattering feature; various authors use the strength of the elastic scattering to deduce plasma properties, such as the ion structure factor [103], the ionization state [4, 5, 30, 75, 104], or the screening properties [105, 106].

However, some of the results from these analyses have come under criticism due to use of physics models for different parts of the Chihara decomposition that are not self consistent [107]. In all of the above cases, simplifying models have been used to determine the precise shape and intensity of both the inelastic and elastic features (for more details on frequently used approximations, see Chapter 4). Much recent work focuses on more detailed modeling of x-ray scattering to help constrain the scattering models through density func-

tional theory and other similar computational tools [9, 107, 108, 109]. These simulations are advantageous in that one does not need to assume simplifying physics models for the different parts of the Chihara decomposition, but disadvantageous in that they are very costly to run, both in expertise and time. It is thus of benefit to the community to run experiments to benchmark models used for Thomson scattering; once Thomson scattering is well understood, it can be better applied to understand the physics of matter in extreme conditions.

Despite some uncertainties in the modeling, XRTS remains a valuable tool to measure plasma properties of dense matter. Because XRTS is based on a theory and not a model, XRTS is not as susceptible to the systematic errors present in some other techniques used to study HEDP. Of course no method is a panacea, and XRTS presents its own difficulties with data interpretation, as alluded to above. In addition, the experiments frequently suffer from low signal-to-noise ratios and high background signals due to the small Thomson scattering cross section. For the present, I shelve the discussion of XRTS, which will discussed in more detail in the later chapters.

3.1.2 X-ray Radiography

X-ray radiography is another important x-ray diagnostic that can probe the physics of high energy density material. In a radiography experiment, x-rays propagate through a shocked plasma target and a detector, such as film or a CCD, collects the transmitted signal. Depending on the instrument, a radiography image can take the form of a 1-D line image that is streaked in time, or several time-gated frames of 2-D images. In either case, the radiographs show the time progression of the shock front which allows one to characterize the shock propagation. The image from the radiograph can be thought of akin to a medical x-ray; an x-ray of a hand shows contrast on the film because bone is higher density than skin and absorbs more of the light. The same principle holds for x-ray radiographs of HEDP experiments; the higher density region in the shock front absorbs more than the lower density regions. The contrast can then be used to determine phenomena related to density, such as the position of the shock front at a specific time.

In addition, if one knows the brightness of the x-ray source before it passes through the sample, the reduced signal after transmission can be used to determine the absolute amount of mass that caused the absorption. If we consider a mono-energetic collimated source of x-rays passing through material, the change in intensity over a small distance dx is written as:

$$dI = \mu I dx \ , \tag{3.18}$$

where I is the irradiance or spectral flux density and μ is the linear attenuation coefficient with units of 1/[length] [110]. Integrating the equation over the distance variable provides the expression for the intensity after absorption:

$$I = I_0 e^{-\mu x} \ , \tag{3.19}$$

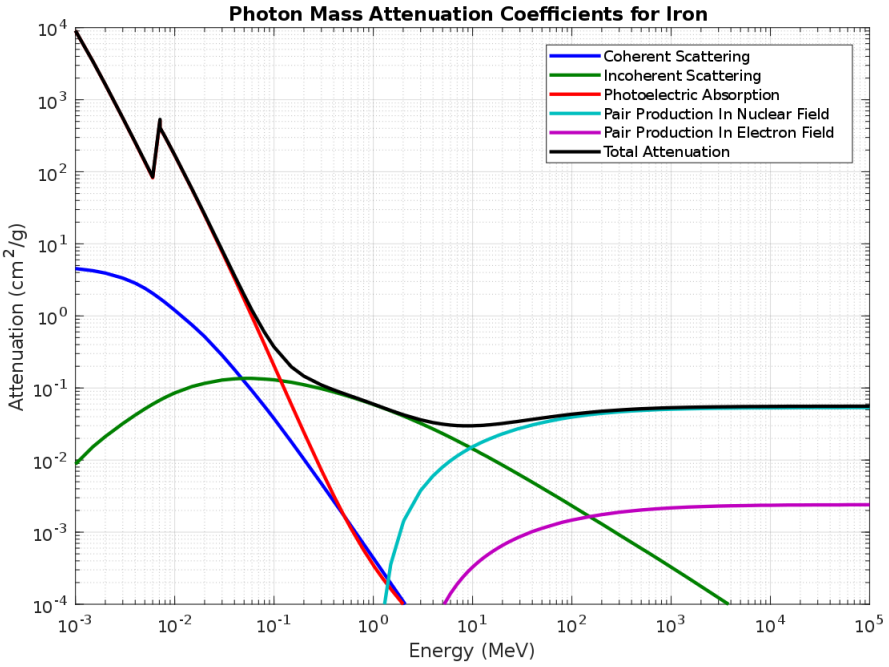

Figure 3.3: Mass attenuation coefficients for iron plotted versus photon energy. Absorption dominates photon interactions below 100 keV.

where I_0 is the initial intensity and x is now the total distance traveled through the sample [110]. In practice, $1/\mu$ can be thought of the mean free path of a photon through the material. Thus, μ can be represented in terms of the interaction cross section as $\mu = n\sigma$, where n is the number density. More commonly, attenuation is expressed in terms of the mass attenuation coefficient, $\mu_m = \mu/\rho$. In practice, μ depends on several physical parameters, such as the ionization state of the sample and the energy of the photon beam. All attenuation processes, including absorption and coherent and incoherent scattering can be described by μ. The values of μ for all interactions have been measured by various experiments and are tabulated in databases managed by the National Institute of Standards and Technology. Figure 3.3 shows iron mass absorption coefficients plotted versus photon energy in MeV from the XCOMS database. Note that for x-rays below 1 MeV, absorption dominates photon attenuation and processes like coherent and incoherent scattering are several orders of magnitude less likely. Thus, if the photon source is below 10 keV, a radiography measurement provides an accurate measurement of mass attenuation.

X-ray radiography measures the attenuated signal through a sample and can be used to determine the density of the sample. In practice, analysis of radiography data is always complicated by the fact that no practical x-ray source is mono-energetic and it is hard to determine the precise 2D profile of the x-ray source. Radiography will be discussed in more detail in the following chapters.

3.1.3 X-ray Fluorescence

Another x-ray diagnostic used in HEDP experiments is fluorescence spectroscopy, which measures the energies and line-shapes of radiative transitions from the atoms that make up a plasma. The energies of the transitions depend on the ionization balances, which in turn depend on the plasma temperatures and densities. Thus, fluorescence spectroscopy provides another way to measure equation of sate variables.

A fluorescence experiment involves a plasma sample that contains a small fraction of a mid-Z or high-Z dopant. A high energy x-ray source impinges on the sample, which excites inner-shell electrons. The excited state of the electron has a finite associated lifetime, and at the end of the lifetime, the electron decays back to its ground state and the atom radiates a photon to conserve energy. The radiated photons are then collected by a spectrometer, and the observed spectrum is compared to theoretically generated spectra that vary plasma parameters to try to reproduce the data. Much previous work has focused on using K-α and K-β fluorescence line ratios and line shapes to determine a sample's temperature [111, 112, 113]. Other work used the energy required to remove a K-shell electron to quantify the effects of continuum lowering in dense samples [79, 114, 115].

In a radiative transition, the radiated photon has the same energy as the difference between the energies of the final and initial states. The change in energy between two electronic energy levels in a hydrogen atom is given by [116]:

$$\Delta E = \frac{Z^2}{2}\left(\frac{1}{n_f^2} - \frac{1}{n_i^2}\right) , \tag{3.20}$$

where n_i and n_f are the initial and final primary quantum numbers. Values of $n_f = 1$ and $n_i \to \infty$ result in the hydrogen binding energy of -13.6 eV. The quantum number n is one of several quantum numbers that classifies the various energy levels available to electrons in an atomic system. The available energy levels are referred to as the atomic structure, which is governed by many different quantum effects, including but not limited to quantized angular momentum, quantized spin, spin-orbit coupling, and relativistic effects. An x-ray fluorescence spectrum shows line emission from many different radiative transitions from these different energy levels, and a detailed understanding of the atomic structure is required to understand the origins of all the emission lines. The energy of the radiative transition provides a way to measure the ionization state of the sample. As an atom ionizes, electrons in excited states experience less shielding of the nuclear charge as a result of fewer bound electrons. Less shielding leads to a higher-energy radiative transition.

Another feature of line emission that depends on the material's equation of state is the line shape. Because each transition has an associated lifetime, the uncertainty principle requires an energy spread to the transition, according to $\Delta E \Delta t \sim \hbar$ [110]. The natural line shape follows a Lorentzian profile, with frequency-dependent intensity given by:

$$I_\nu = I_0 \frac{(\gamma/4\pi)^2}{(\nu - \nu_0)^2 + (\gamma/4\pi)^2} , \tag{3.21}$$

where I_0 is the central and maximum intensity, γ is again the damping constant and also the decay rate of the excited state, and ν_0 is the central frequency. The line shape can change with an increased plasma temperature through Doppler broadening, which means the line shape can be a way to determine the plasma temperature. In the case of Doppler broadening, the line shape takes on a Voigt profile, where the center line becomes dominated by a Gaussian function shape [93]. However, the resolving power of the spectrometer must be greater than a million to see such an effect [110]. Another type of broadening is called pressure or collisional broadening and can result from increased density or temperature. Collisional broadening reduces the associated lifetime of the excited state and thus increases the energy band-width of the Lorentzian line-shape of the radiative transition.

The plasma conditions can be extracted from fluorescence spectra by comparing data with theoretically generated fluorescence spectra. The plasma parameters used to generate the theoretical spectra can be altered until the predictions match the data. Two commonly-used codes for extracting plasma parameters from fluorescence spectra are Cretin [117] and FLYCHK [118]. In order to generate valid results, the codes require detailed atomic models, which describe all the possible electron energies for all possible ionization states of an atom. However, the statistical weight of each electron energy level increases exponentially with the number of electrons in the system, even for a single electron excitation. Thus, for an atom like argon with 18 electrons, one would have to account for roughly 10^7 possible electron configurations for only one electron excitation (if one considers excitations up to the $n = 10$ energy level). Typically, one accounts for several different possible electron excitations, which means the model must include even more possible electron configurations. For practical and computational purposes, extensive simplifications of the atomic models are often required in data analysis. The codes use the simplified atomic models to calculate the atomic kinetics and the radiative properties [119, 120]. Because of the simplifications and modeling required, analyzing fluorescence data is a complicated and convoluted technique subject to much systematic error. Like any multi-parameter fit, one must be sure to use self-consistent models to avoid obtaining the right answer for the wrong reasons. The primary advantage to fluorescence is that the signal levels scale with the absorption cross section, which results in a lot more signal than could ever be obtained in an XRTS experiment. Ideally, both techniques should be benchmarked against each other to provide data that enhances our certainty in data analysis.

3.1.4 Neutron Spectroscopy

Another method to diagnose plasma conditions in HEDP involves measuring neutrons from fusion reactions with neutron time-of-flight (nTOF) spectrometers. The average reactivity of a fusion reaction is defined by:

$$\langle \sigma v \rangle = \int_0^\infty \sigma(v) v f(v) dv \ , \tag{3.22}$$

where σ is the cross section, or probability per pair of particles of the occurrence of the reaction, v is the velocity, and $f(v)$ is the velocity distribution [41]. The reaction rate of species '1' and '2' with densities n_1 and n_2 depends on the mass density and reactivity of the sample by:

$$R_{12} = \frac{f_1 f_2}{1+\delta_{12}} \frac{\rho^2}{\bar{m}^2} \langle \sigma v \rangle \ , \tag{3.23}$$

where f_1 and f_2 are the atomic fractions of species '1' and '2', δ_{12} is the Kronecker delta function, and $\bar{m}$ is the average mass density [41]. Thus, the reaction rate depends on both the density and the temperature of the sample.

The fusion reaction with the largest cross section is:

$$\mathrm{D} + \mathrm{T} \rightarrow \alpha \ (3.5 \text{ MeV}) + \mathrm{n} \ (14.1 \text{ MeV}) \ , \tag{3.24}$$

where α refers to an alpha particle and n to a neutron. Two other reactions with D+D are equally probable:

$$\mathrm{D} + \mathrm{D} \rightarrow \mathrm{T} \ (1.01 \text{ MeV}) + \mathrm{p} \ (3.03 \text{ MeV}) \ , \tag{3.25}$$

and:

$$\mathrm{D} + \mathrm{D} \rightarrow {}^3\mathrm{He} \ (0.82 \text{ MeV}) + \mathrm{n} \ (2.45 \text{ MeV}) \ , \tag{3.26}$$

where p is a proton. There is also a T+T reaction that has a similar cross section to the D+D reactions:

$$\mathrm{T} + \mathrm{T} \rightarrow \alpha + 2\mathrm{n} + 11.3 \text{ MeV} \ . \tag{3.27}$$

An experiment that seeks to use neutrons to measure either temperature or density will dope a sample with deuterium or tritium. Then, the nToFs will be set to look for neutrons with specfic energies that are known to arise from fusion reactions. One previous experiment imploded solid CD_2 spheres and measured neutrons with energies of 2.45 MeV that resulted from D-D fusion reactions [121]. The nToF spectrum was Doppler-broadened in time as some of the neutrons were generated in shocked material that was moving with a thermal velocity similar to the neutron velocity. After accounting for Doppler-broadening effects, the amount of neutrons produced per time was analyzed to return the reactivity of the reaction, which allowed determination of the density and temperature in the implosion hot-spot. There are also several other examples of experiments that similarly used a Doppler-broadened neutron spectrum to determine hot-spot conditions [122, 123]. The advantage of neutron spectroscopy is that neutrons are not very interactive with matter, which results in high accuracy measurements. The limitations are that fusion reactions only occur in parts of the sample that are hot enough to cause fusion, which often limits the applications of neutron spectroscopy to hot-spot related measurements.

3.2 The Gigabar Platform

The Gbar platform [124, 125] is a platform designed for the NIF to measure the absolute equation of state of a spherically convergent sample up to pressures exceeding 1 Gbar, which

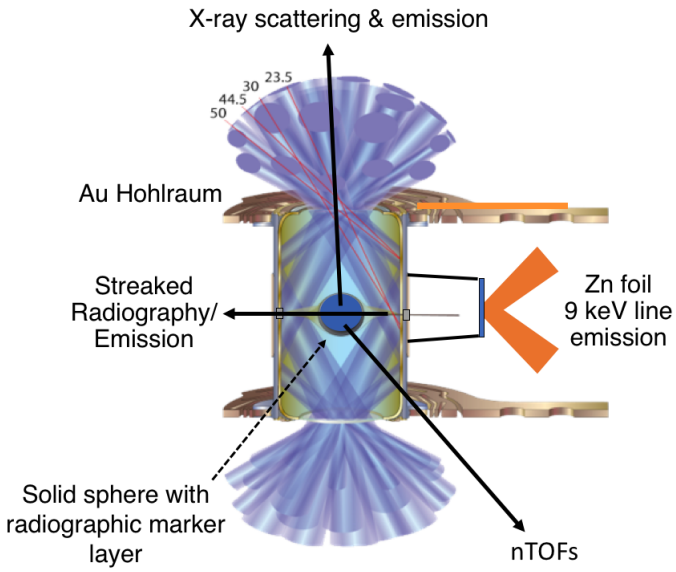

Figure 3.4: A schematic of the Gbar platform. As the solid sphere compresses due to the hohlraum-generated ablation pressure, a Zn He-α x-ray source backlights the sphere to provide streaked x-ray radiography and time-gated XRTS measurements. The radiography measurement allows for an absolute measurement of the Hugoniot equation of state.

is 10^9 times greater than Earth's atmospheric pressure. Figure 3.4 shows a schematic of the target and the placement of the primary diagnostics, which include radiography, x-ray Thomson scattering, neutron spectroscopy, and penumbral imaging of x-ray emission. The Gbar target is similar to a typical NIF ICF target in that an Au hohlraum is used to indirectly-drive a capsule implosion at its center. In the case of Gbar, the capsule consists of a solid carbon-based sample surrounded by ablator layers. A thin layer of the ablator is doped with silicon or germanium, which absorbs Au M-shell emission and prevents preheat of the center sample. There are two slits in the hohlraum, each directly across from the other, located on the hohlraum midline. A Zn backlighter foil is mounted over one slit. As the sample compresses from hohlraum driven laser ablation, several lasers heat the Zn backlighter, which allows for several different measurements to be made to constrain the equation of state.

The primary diagnostic for the Gbar platform is the streaked radiography measurement, which measures the mass density behind the shock front and shock speed at different points in time in order to measure the Hugoniot over a range of pressures; previous measurements ranged from 100 Mbar - 1 Gbar [124, 121]. X-rays from the Zn propagate through the slit in the hohlraum, then through the sphere and out the other slit. Because the radiography image it is streaked, the measurement shows the time dynamics of the implosion. Figure 3.5 shows a simulated streaked radiography measurement of an imploding CD_2 sphere in the Gbar platform [121]. The radiography measurement shows several features, as noted in the

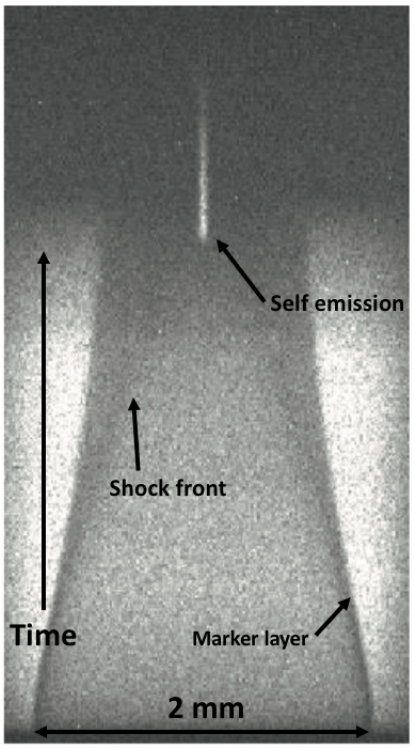

Figure 3.5: Simulated radiograph of an imploding CD_2 sphere from the Gbar platform. The position f the shock front decreases in radius until the capsule reaches peak compression. Reprinted from High Energy Density Physics, 21, Nilsen et al., Using neutrons to measure keV temperatures in highly compressed plastic at multi-Gbar pressures, p. 20-26, Copyright (2016), with permission from Elsevier.

figure. The primary features are the shock front and the radiography marker layer, as well as emission from the central hotspot once the shock waves converge in the center. The shock speed can be determined at each point in time by a $\Delta x/\Delta t$ calculation. The radiography marker layer constrains the amount of mass in the sample at each point in time by noting the outer radius of the spherical sample. By knowing the outer radius of the sample and the density of the unshocked region, the density in the shocked region can be inferred.

The Gbar platform is able to probe multiple points on the Hugoniot in just one measurement because the platform uses a spherically convergent geometry. As the shock travels inwards, convergent flow causes the shock pressure to increase due to accumulating mass in the shock front. The pressure increases with radius as [124]:

$$P \sim r^{-2\beta} \ , \tag{3.28}$$

where $\beta = 1/2 + 1\gamma + (\gamma/2(\gamma-1))^{1/2}$, and in this case, γ is the adiabatic index. For $\gamma = 5/3$, $\beta = 0.45$ and for $\gamma = 4/3$, $\beta = 0.375$ [124]. Initial experiments showed a 4% error on both density and pressure measurements, which will help constrain the Hugoniots of materials at

such high pressures. As Figure 2.5 shows, the compressibility versus pressure of materials varies greatly with the assumed EOS. Thus, experimental data at high pressures is still needed to benchmark the equations of state. Initial measurements on CH spheres are still being analyzed, but show promise in resolving the equation of state [D. Swift et al., in prep., T. Döppner et al., submitted to Phys. Rev. Lett., and A. L. Kritcher et al., in prep.].

Another important measurement technique for the Gbar platform is XRTS [126]. In this case, x-rays from the Zn scatter from the compressed sample along the hohlraum axis through laser entrance holes to a time-gated spectrometer [127, 128] that collects XRTS spectra. Initial spectra from an imploded CH capsule showed much higher ionization than predicted by most commonly applied ionization models in the regime [75]. However, the measurement arose from the inhomogeneous conditions of an imploding sphere, and there were many background signals present, which convoluted data interpretation. More improved measurements are needed to increase confidence in the results. Because the shape of the Hugoniot depends on the ionization state of the sample, XRTS offers an independent way to benchmark the Hugoniot measurement from the radiography diagnostic and can provide important insight into the material conditions.

Neutron emission can also be used to determine plasma conditions in a deuterium or tritium doped Gbar capsule. The Doppler-broadened neutron spectrum reflects the velocity distribution of ions in the sample [121, 123, 122]. In one experiment on the Gbar platform, nTOFs measured the neutron yield as a function of time from imploding CD_2 capsules to determine the temperature and density in the hot-spot [121]. The neutron yield in combination with x-ray radiography can help constrain EOS models, as well as models of hot-spot formation.

Finally, x-ray emission from the hot-spot has been observed with penumbral imaging in order to return information about the hot-spot micro-structure in Gbar implosions [129, 130]. Penumbral imaging involves viewing the x-rays emitted from the hot-spot through a pinhole array attached to a time-gated x-ray camera. The images from the camera can be analyzed to return high-resolution images of the hot-spot, which allows assessment of the hot-spot size and capsule compression ratio [129].

These four measurement techniques of the Gbar platform were initially developed as part of the Discovery Science program on the NIF, which allows university researchers to pair with Livermore scientists to do measurements on the world's most energetic laser. Because of the success of the Gbar platform, several groups at Livermore now use the platform to measure the absolute Hugoniot of materials at extreme conditions. The Gbar platform was then extended to the OMEGA laser to increase the number of shots and data points, and to improve diagnostics like XRTS. Chapter 5 will discuss results from an implementation of the Gbar platform on OMEGA, and show the resulting radiography and XRTS data.

Chapter 4

Using X-ray Thomson Scattering for Warm Dense Matter Experiments on the OMEGA Laser

In this chapter, I describe the practical aspects of performing an XRTS experiment on the OMEGA laser and all the considerations that must be taken into account, ranging from target design techniques to data analysis. I illustrate the many trade-offs to consider when constructing a target by describing the iterative process I went through to design experiments on spherical implosions. I then discuss the details of processing XRTS data from images to spectral line-outs. Finally, I outline the models we use to extract plasma parameters such as temperature and density from spectra.

4.1 Experimental Design Considerations

An XRTS experiment at a large laser facility requires three components: a narrow-band x-ray source, a spectrometer, and a plasma target. The following sections describe the three requirements in more detail.

4.1.1 X-ray Source

There are no built-in x-ray sources that are suitable for XRTS or radiography measurements at facilities like OMEGA and NIF, so experimenters have to generate x-rays by use of laser-driven foil backlighters. A foil backlighter is created when several lasers heating a thin foil to keV temperatures, which ionizes the atoms in the foil to a helium-like state; the atoms then emit helium-like K-α line radiation, which is referred to as He-α radiation [131]. He-α radiation appears as a doublet of two lines from the ortho- and para-helium-like states, which results from the two electrons being in either singlet or doublet states [116]. XRTS measurements use Zn as the backlighter foil material on OMEGA and NIF; experimenters chose to

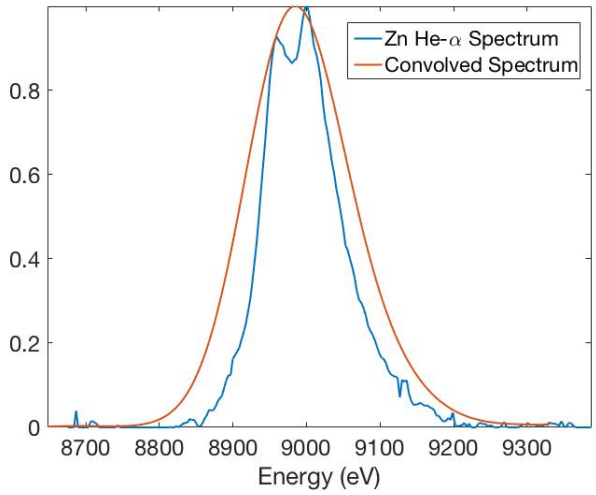

Figure 4.1: A measured Zn He-α source spectrum and the same spectrum convolved with a 15 eV FWHM Gaussian. The Zn He-α doublet shows line emission at 8.950 and 8.999 keV.

use the Zn He-alpha line because the 9 keV line is of high enough energy to propagate through $\sim$1 mm of 4x compressed CH plastic, which was required for early ICF experiments [127]. Zn He-α doublet line emission occurs at 8.950 and 8.999 keV [127].

On OMEGA, XRTS experiments use 6-10 beams on a foil to generate Zn He-α radiation. The lasers are focused to obtain the best conversion efficiency from laser light to Zn He-α radiation, which occurs with a laser irradiance of 2×10^{15} W cm^{-2} [131]; this often amounts to a laser spot-size of 300 μm. A 300 μm spot-size implies that the Zn He-α spectrum will be blurred due to the finite source size of the laser-spot on the foil. Figure 4.1 shows an example of a measured Zn He-α spectrum from a small (< 50 μm) laser spot, and the same spectrum convolved with a Gaussian. In practice, the convolved spectrum is used as the XRTS source spectrum in data anlysis; the width of the Gaussian used in the convolution is altered to match the width of the elastic scattering peak in the data.

4.1.2 Spectrometer

We use the time-gated OMEGA spectrometer called ZSPEC to collect XRTS spectra. ZSPEC means "zinc spectrometer," and is named as such because it collects x-rays with energies between 7.5 - 10 keV, which is centered around the Zn He-α emission.

A schematic of the ZSPEC is shown in Figure 4.2. ZSPEC is a Bragg crystal spectrometer, which consists of a 50 mm x 25 mm highly oriented pyrolytic graphite (HOPG) crystal placed equidistantly from a gated microchannel plate (MCP). The MCP contains four different strips arranged vertically (in space and in the orientation of Figure 4.2). Time gating of each strip occurs by an applied bias voltage across the MCP. The voltage is a square pulse, which sweeps over the strip in 200 ps. In order to obtain enough signal, XRTS measurements

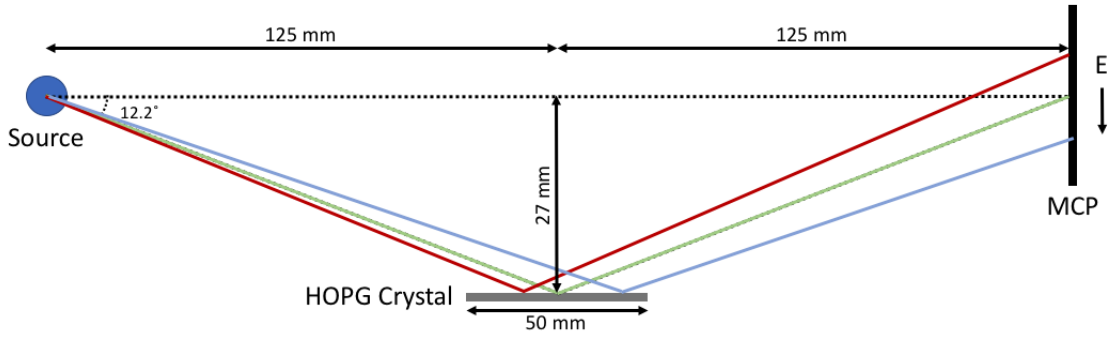

Figure 4.2: A schematic of the ZSPEC at OMEGA. ZSPEC consists of a highly oriented pyrolitic graphite (HOPG) crystal equally spaced between the source and a gated mircrochannel plate (MCP). The different colors in the figure represent different energy x-rays; the x-rays must satisfy the Bragg condition to reflect constructively to the MCP.

use a 500 ps pulse-width for the MCP voltage, which results in 180 ps of integration time due to the characteristic MCP signal rise time. The bias voltages of each strip can be set independently to change the signal gains in each strip. The MCP generates a signal when scattered photons cause electrons from the MCP material to cascade through the MCP in response to the applied voltage. The electrons then hit a phosphor screen behind the MCP, which fluoresces as a result of electron impact. A CCD behind the screen captures the image from the phosphor screen, which generates the image-based data. Often, the bias voltages and timings of the ZSPEC strips will have to be changed between shots in order to obtain good signal on all strips. These changes are routine and can be easily completed within a shot cycle.

The HOPG crystal in ZSPEC is a mosaic crystal comprised of several layers of many smaller graphite crystals with slightly different orientations to the normal. Mosacity is defined as the FWHM of the Gaussian of angular spread of crystal orientation, and takes a value of 0.3° in the ZSPEC. A crystal with high mosaicity has an integrated reflectively of over 10-100 times as high as a single crystal [132, 133], making it an ideal tool in the case of XRTS experiments, which often suffer from low signal levels. As described in Reference [133], photons of a specific energy fanning from a point source can reflect constructively through many different paths and at different depths in the crystal, which results in higher signal levels. However, mosaicity often affects the resolution of the instrument; the spectrometer has a limited resolving power of roughly $\Delta E/E \sim 2 \times 10^{-4}$ [134].

The crystal resolves photons that satisfy the Bragg condition [94]:

$$n\lambda = 2d \sin\theta_B \ , \tag{4.1}$$

where n is the diffraction order, λ is the wavelength of light, d is the lattice plane spacing in the crystal, and θ_B is the Bragg angle. XRTS experiments typically use first order reflections

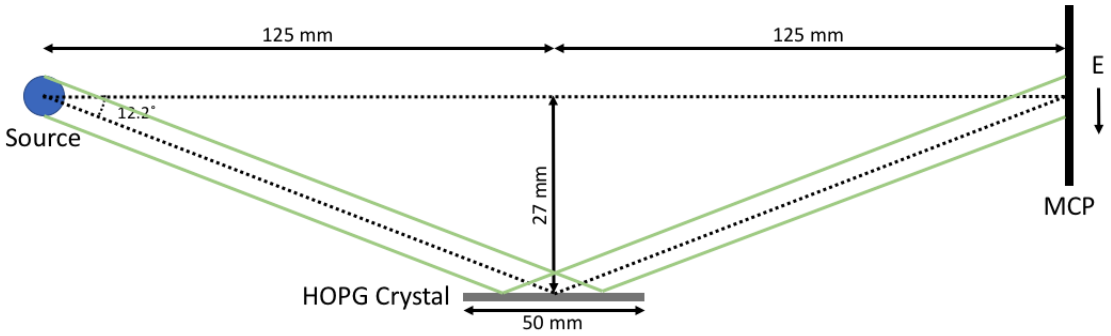

Figure 4.3: A schematic of the ZSPEC at OMEGA showing how the same energy x-rays arising from different sources may appear offset in the energy.

($n = 1$), and for ZSPEC, $2d = 0.67$ mm and $\theta_B = 12.2°$. Because reflections must satisfy the Bragg condition, different energies of light reflect constructively at different reflection angles, as indicated in Figure 4.2. The dispersion of the ZSPEC is calculated as:

$$\frac{\Delta E}{\Delta x} = \frac{E}{2F \tan\theta_B} , \tag{4.2}$$

where E is the center energy and F is the distance between the center of the crystal and the source, $F = 125 \text{ mm}/\cos\theta_B$. At 9 keV, the rule-of-thumb is 1 mm = 150 eV.

Another feature of the ZSPEC is one-to-one distance mapping from the source to the detector. This arises from the equidistant crystal placement between the source and the MCP [127]. Figure 4.3 shows how monoenergetic x-rays that emerge from different points in space may appear shifted in energy. This often means that unwanted signals in spectra contain a mix of energy and spatial information, and it is up to the experimenter to determine the origin of the signal.

The ZSPEC includes a blast shield to protect the crystal from any debris that might be generated in the experiment. The ZSPEC may also contain filters in front of the MCP module in order to reduce x-ray signal. XRTS experiments use a Be blast-shield, which is near-transparent to 9 keV x-rays. For shots in which the ZSPEC looks directly at line emission from a target, the MCP filtering includes ∼600 μm of aluminum.

4.1.3 Target

The design of the scattering target can have many effects on the data obtained from the spectrometer, including overall signal levels. As described in Chapter 3, the Thomson scattering cross section is small enough such that obtaining adequate signal levels in an XRTS experiment always presents a challenge. To be sure an experiment will be successful, one first has to calculate the number of photons to be collected at the detector; this is referred to as calculating the photometrics of an experiment.

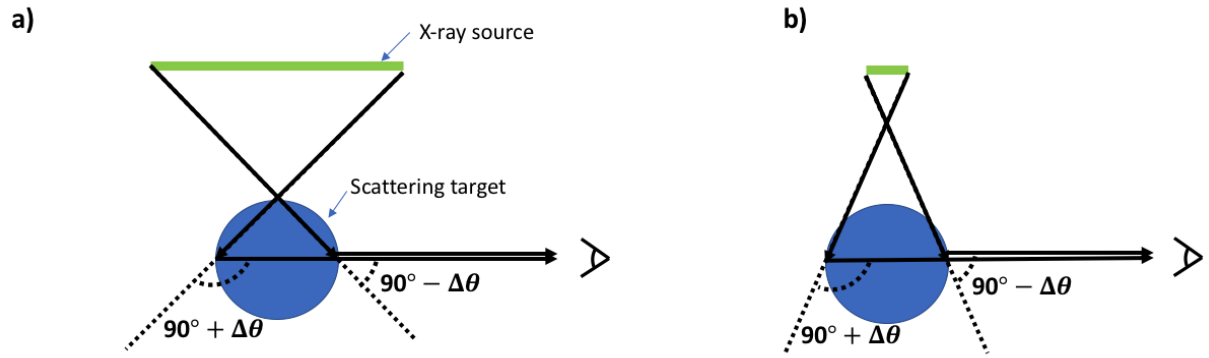

Figure 4.4: A schematic of k-vector blurring from an experiment that nominally has a 90° scattering angle. a) k-vector blurring that is dominated by the size of the source, b) k-vector blurring that is dominated by the size of the scattering target.

We calculate the photometrics by first considering that the Zn x-ray source emits photons into a 4π solid angle. The number of photons that reach the scattering target depends on the solid angle that the target subtends. Photons that reach the target again scatter into 4π with some probability, and a portion of those photons eventually reach the detector. The number of photons that will be detected can be estimated by [62]:

$$N_{ph,det} = \left(\frac{E_L}{h\nu}\right)\left(\frac{\Omega_{plasma}}{4\pi}\right)(n_e\sigma_T l)\left(\frac{\Omega_{det}}{4\pi}\eta_{det}\right) , \tag{4.3}$$

where E_L is the energy of the laser incident on the backlighter foil, $h\nu$ is the energy of a single photon, Ω_{plasma} is the solid angle subtended by the plasma sample, n_e is the electron density, σ_T is the Thomson scattering cross section, Ω_{det} is the solid angle subtended by the spectrometer, and η_{det} is the quantum efficiency of the detector.

Designing an XRTS target often involves an optimization between higher signal levels and challenges in data interpretation. One such compromise involves signal level versus k-vector blurring. k-vector blurring occurs when an experiment probes the average of multiple scattering angles, which results in measuring scattering from several k-values. This can obfuscate interpretation of data by artificially broadening the resulting scattering spectrum. Figure 4.4 shows a schematic of how k-vector blurring can occur for the case of a large source (a) and for the case of a large target (b). Both examples show a nominal scattering angle of 90°, but the finite source and target sizes show that x-rays will scatter to the spectrometer with scattering angles of $90° \pm \Delta\theta$, as depicted. Increasing the distance between the source and the target decreases the effects of k-vector blurring. However, decreasing the distance increases the signal levels by a factor of r^2. In practice, all experiments have some k-vector blurring, but the distribution of angles probed is sharply peaked around the designed scattering angle. A rule-of-thumb for OMEGA experiments is that the source should be 1 mm away from the scattering target for adequate signal levels and minimal k-vector blurring.

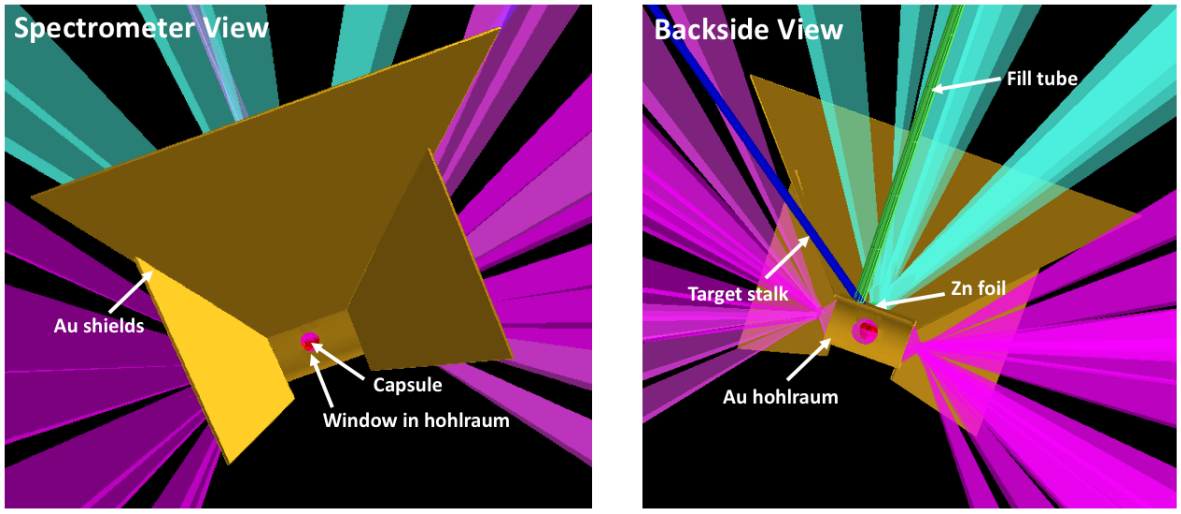

Figure 4.5: Two VISRAD [135] screen shots of experimental configurations on hohlraum-driven spheres. 20 lasers drive the holraum, and 6 beams drive the Zn backlighter foil which sits over a notch cut in the hohlraum's side. The left image shows the spectrometer's view of the capsule. The Au shields block the spectrometer's direct line-of-sight to the Zn foil and to x-rays generated by the hohlraum drive. The right image shows the backside view of the hohlraum and is intended to demonstrate the complexity of laser pointing in a demonstrative XRTS experiment.

Another design consideration that competes with signal levels is shielding of the x-ray source from the spectrometer. Decreasing the distance between the x-ray source and the target increases signal levels, but also increases the challenge of blocking the spectrometer's direct line-of-sight to the Zn foil. Blocking the direct line-of-sight is crucial to obtaining high-quality scattering measurements, as any x-ray signal directly from the foil will be orders of magnitude stronger than the XRTS signal. To make things more challenging, the Zn can expand around the shielding once the backlighter drive lasers turn on. The lasers heat the Zn, which becomes a plasma and expands like liquid around the target. The way to mitigate signal-leakage from the expanding plasma is to make shielding structures large enough such that any signal that emerges from expanding Zn will be far enough separated from the scattering signal as to not distort the data. Using the rule-of-thumb for dispersion, signals that could appear on the low energy side should be separated by roughly 600 eV, which requires a shield that subtends 4 mm in the dispersion plane, and the high energy side by 100 eV, which requires a 0.66 mm shield. It is thus advantageous to plan a target such that emerging Zn plasma will appear on the high energy side as so less shielding mass is required.

In addition to the above listed considerations, there are many other target-related details that must be considered: the scattering target must have a direct line-of-sight to the laser spot on the Zn foil, the XRTS measurement must be made when the beams driving the

target are off to avoid seeing a strong thermal-emission spectrum background, glue must be placed on junctions of shielding where Zn plasma could leak through, and none of OMEGA's 60 beams should clip anywhere on the target. In order to overcome these challenges, there is a software developed by Prism Software called VISRAD [135]. VISRAD is a full 3-D view factor code that allows one to build a 3-D target inside a simulated target chamber, and then point and focus the OMEGA laser beams on to targets in order to estimate deposited power. As an example of the possible complexity of a target and laser configuration, Figure 4.5 shows two VISRAD screen shots from an indirect-drive XRTS campaign. Twenty beams generate the hohlraum drive and six beams heat the Zn backlighter foil. The backlighter beams are pointed and focused to avoid both the target stalk and the hohlraum fill-tube; the fill-tube puts a gas pressure inside the hohlraum to help avoid Au blowoff towards the capsule. The images are intended to demonstrate the technical challenges of pointing lasers in the OMEGA chamber- there are many beams, all with the ability to be pointed independently. On the more powerful NIF laser, other considerations must be taken into account, such as reflections from unconverted infrared laser light, bringing even more necessity to programs like VISRAD.

The challenges in designing an XRTS measurement are many, which is why there is still a dearth of experimental XRTS data from high power laser facilities. However, with the right combination of target elements, a successful experiment can be performed.

4.2 The Gigabar Platform on OMEGA

To illustrate the challenges in designing XRTS targets for OMEGA, I will describe the iterative path we took in designing two platforms to take XRTS data from imploding spheres: one in direct-drive geometry and the other in indirect-drive geometry. In collaboration with a group at Livermore, I participated in the OMEGA Gbar campaign, which was a programmatic campaign that sought to measure the Hugoniot of pressures ranging from 50 - 200 Mbar in a spherically convergent geometry. This was an extension of the Gbar platform described in Chapter 3, and aimed to support the NIF Gbar data by providing additional data. The primary diagnostic of the campaign was again x-ray radiography. However, a temperature measurement was also desired, so the platform expanded to include XRTS. The goal was to design platforms in which XRTS and x-ray radiography shots could be taken back to back in an OMEGA shot day to measure the full phase space of a capsule implosion. The desire for two configurations in one shot day imposed several limitations on the target geometries of both measurements; namely, the lasers used to drive the backlighter foils could only be repointed once per day and by less than 1 mm.

Figure 4.6 shows a schematic of three different direct-drive XRTS targets that were shot on three successive XRTS campaigns. All campaigns were based off of the previously successful OMEGA XRTS experiments of Kritcher et al. and Fletcher et al. [4, 60], who used spherical shells of beryllium or CH with diameters on the order of 860 μm. In the previous campaigns, conical Au shielding cones were glued directly to the spherical shells.

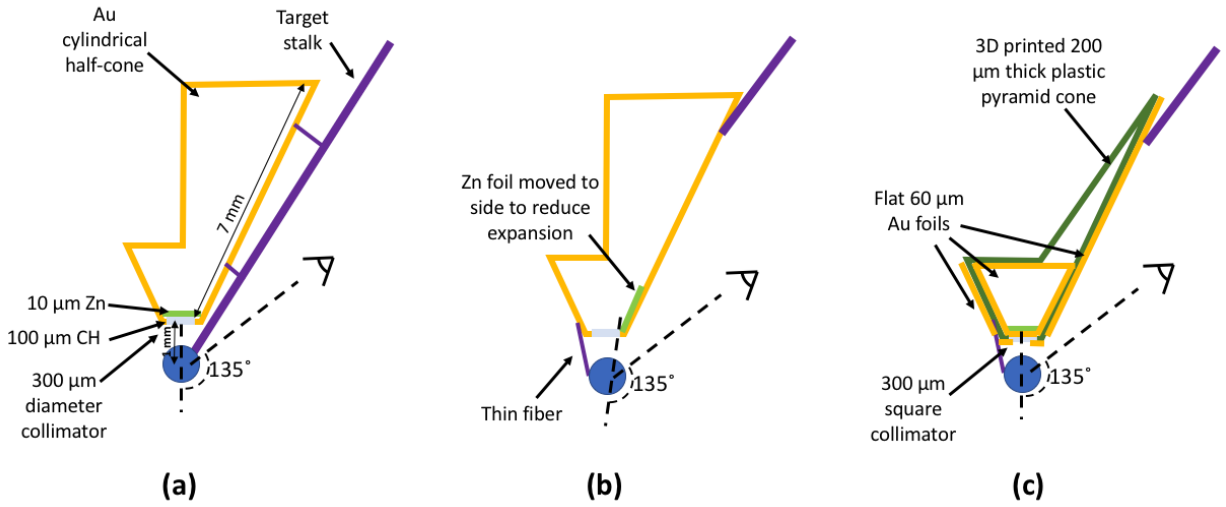

Figure 4.6: Three iterative target designs used to take XRTS measurements from directly-driven imploding spheres on the OMEGA laser. (a) The first target was based off of previously successful work [60, 4]; measurements later in time were corrupted by Zn plasma emerging from the cone tip; the target stock was also too large and perturbed the implosion. (b) The second design reduced the effect of the stalk and attempted to mitigate Zn plasma blowout by placing the Zn foil on the inside of the cone. This was unsuccessful, as a lip at the end of the cone from target manufacturing blocked the direct line-of-sight from the laser spot on the Zn foil to the compressed sample. (c) The third design used 3D printed plastic cones covered in Au foils to reduce the cost of the targets and collected clean scattering data.

The Zn backlighter foils were glued on the inside edges of the cones, close to the spheres. We adapted the experimental geometry so radiography measurements could be performed in series. This led to the separation of the cone and the sphere, as shown in Figure 4.6. All the Gbar campaigns used carbon-based spheres (CH, CH_2, CD, and diamond) with radii that ranged from 430 - 1000 µm in diameter. The shielding cones contained an opening at the tip, over which was placed 100 µm of CH with 10 µm of Zn on top. The opening angle of the cone was designed to be wide enough to accept six backlighter beams, which were focused to 300 µm diameter spot sizes; this yielded maximum conversion efficiency to Zn He-α light with an intensity of $\sim 1.5 \times 10^{15}$ Wcm^{-2} [131].

The first campaign, depicted in Figure 4.6(a), was a half shot day in which we took two XRTS shots. The shots showed promising signal-to-noise ratios, but shots later in time showed a non-physical increase in the elastic scattering signal, as well as background signal emerging from Zn expanding outside the shielding cone. In addition, the target stock created a significant perturbation in the implosion, as the amount of mass in the stock was on the same order of magnitude as the mass in the sphere. The second campaign changed how the sphere was mounted to the cone by using a small fiber instead of the large stock. To

mitigate Zn backgrounds, the Zn foil was moved to the inside edge of the cone, as seen in Figure 4.6(b). This succeeded in reducing the expansion of Zn plasma around the cone. However, we failed to collect an XRTS signal. The cause was at first mysterious, but we deduced that it was because the sphere did not have a direct line-of-sight to the laser spot on the Zn foil. The gold shielding cone came to a tip, and at the tip, there was a slight gold lip that arose from machining. When the sphere was moderately compressed, no potion of the sphere had a direct line of sight to the laser spot on the foil. Up to this point, it was believed that the XRTS x-ray source arose from both the laser spot on the Zn foil and expanding Zn plasma that interacted with the lasers. However, if that were true, expanding Zn plasma would have come into the field of view of the compressed sphere. In our case, we did not collect any XRTS signal, which suggests the expanding Zn did not create a bright enough x-ray source for XRTS. The experiment demonstrated that the scattering target must have a direct view of the laser spot on the Zn foil in order to generate a scattering signal.

On the final direct-drive shot day, we moved the Zn foil back to the tip of the cone and restricted our shot timing to the earlier half of the backlighter drive. The machined Au cone was replaced with a 3-D printed plastic cone covered with Au foils to reduce the cost of target fabrication. The targets resulted in good XRTS data when used with the larger 1 mm diameter diamond spheres (discussed in detail in Chapter 5), but failed to generate strong signals for the smaller 430 μm CH spheres. We believe this was again due to alignment of the spot of the lasers on the Zn foil with the sphere. These targets included a gold foil collimator over the tip of the cone to reduce the x-ray source size. A slight misalignment of the target with respect to the laser system could result in a loss of the line-of-sight from the sphere to the laser spot on the Zn foil. In the future, the collimator will be removed, and all experimental designs will be built to tolerate these misalignments. However, the resulting high quality data from the diamond spheres offer important information on warm dense diamond and signify a successful platform development.

We also developed an XRTS platform for hohlraum-driven spheres. Figure 4.7 shows a schematic of the three different iterations of hohlraum targets. All targets used a 1.3 mm x 2 mm hohlraum with 1 mm laser entrance holes. In all three cases, the Zn foil was placed over plastic that covered a window carved in the hohlraum wall. All configurations used carbon-based spheres with diameters ∼500 μm. In the first configuration, the spectrometer viewed the sphere down the hohlraum axis. A flat Au disc shielded the spectrometer from a direct line of sight to the Zn foil. The shield subtended 180° around the hohlraum and failed to provide adequate protection from Zn expanding around the target. The shot day resulted in successful collection of inelastic scattering data, but the elastic peak was overshadowed by a direct view of Zn. The results are described in Reference [136].

The second configuration of XRTS from hohlraum targets altered the orientation of the spectrometer such that it viewed the sphere through a window in the hohlraum wall. This was due to classification concerns, as well as a desire to prevent the spectrometer from seeing thermal continuum emission backgrounds from the hohlraum. An Au cone contained the spread of the Zn foil on the side of the hohlraum, as depicted in Figure 4.7(b). However, the orientation of the cone on the side of the hohlraum proved difficult for the target fabrication

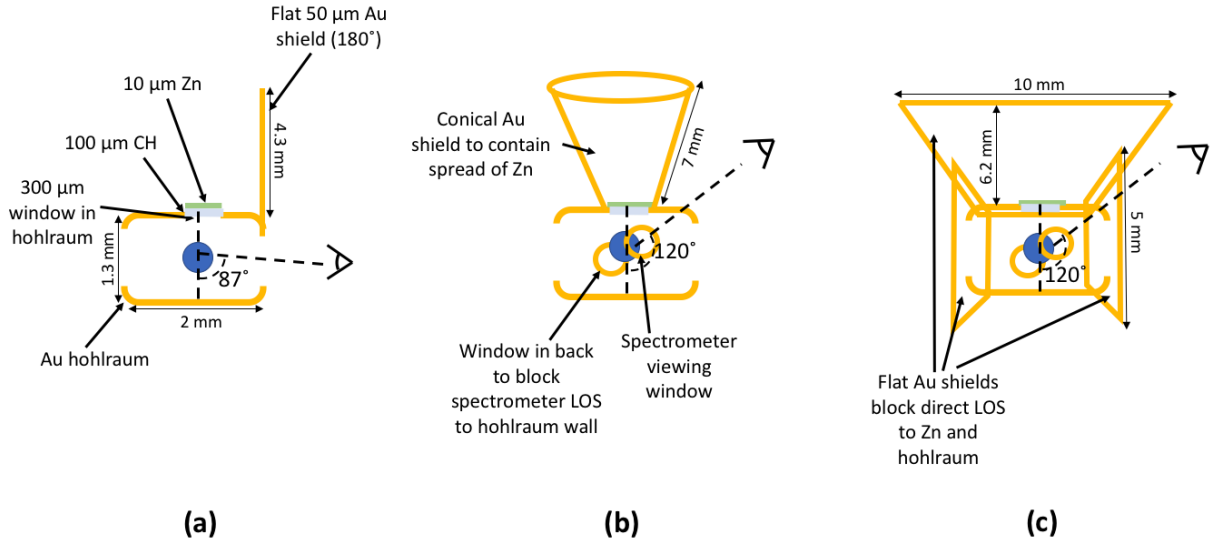

Figure 4.7: The three iterative target designs used to take XRTS measurements from hohlraum-driven spheres on the OMEGA laser. All three designs use a 2 mm x 1.3 mm hohlraum to compress a plastic sphere that ranges from 430 - 600 µm in diameter. The 10 µm Zn foil provides the Zn He-α x-ray source for the scattering experiment. (a) In the first design, the spectrometer viewed the imploding sphere through the hohlraum axis and used a half-circle Au shield [136]. However, the shielding was ineffective. (b) The second design attempted to mitigate the shielding issues by containing the Zn plasma with a full cone. It also moved to a back-scatter geometry, in which the spectrometer views the sphere through a window in the hohlraum. (c) The final design used a series of flat shields to block the spectrometer's line of sight to the Zn. The best results were obtained with this platform.

team to complete, and several targets fell apart in the target chamber before the measurement was made. In the end, the cone model had to be abandoned and we moved to flat pieces of Au to shield the spectrometer, as seen in Figure 4.7(c). This platform yielded the most successful results. However, the intensity of the elastic peak increased unphyiscally as a function of backlighter drive turn-on time. We believe this was due to Zn expanding into the hohlraum. In the future, this measurement will be improved by increasing the thickness of the plastic that supports the Zn. This will prevent the plastic from being ablated and will lead to a successful XRTS measurement.

4.3 XRTS Data Processing

Once successful XRTS data is taken, there are several steps required to generate spectral line-outs. These include: dispersion calibration, flat fielding, accounting for filter transmission, background subtraction, and source-function calibration. This section describes each process.

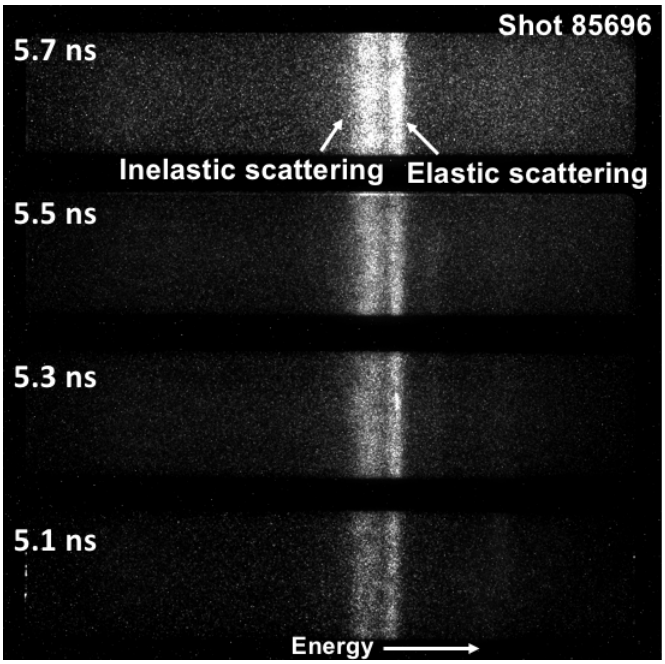

Figure 4.8: Raw XRTS data from directly-driven solid diamond spheres from the ZSPEC on OMEGA shot number 85696. Each strip is time gated and integrates over 200 ps. The elastic and inelastic scattering features are indicated.

Figure 4.8 shows an image of raw XRTS data from directly-driven 1 mm diamond spheres on the OMEGA laser. Each strip is time gated and integrates over approximately 200 ps. The two peaks of elastic and inelastic scattering are visible in all four strips. A line-out from each strip can be obtained by summing the signal in the vertical dimension in one strip. The first correction to be performed is flat-fielding. Flat-fielding helps to account for any defects in the HOPG crystal, which can result in areas of the crystal with more or less reflectivity and can distort the shape of the scattering spectrum. A flat-fielding measurement is made by measuring the bremsstrahlung spectrum of a mid-Z material, such as aluminum. The bremsstahlung spectrum shows the areas of the crystal with low or high reflectivity, which can then be used to correct the data. One can also account for crystal non-uniformities by averaging over scattering spectra that are taken at the same time from different strips on the detector.

After accounting for crystal non-uniformities, one needs to calibrate the horizontal axis of the scattering spectrum from pixels to energy. The dispersion can be calculated by Equation 4.2, which derives from the spectrometer geometry. However, Equation 4.2 relies on an accurate understanding of the distance between the center of the crystal and the target, as well as the energy for which the distance between the crystal and target and target and source are equal. The nominal stand-off distance for ZSPEC is 125 mm and the center energy is 8600 eV. But the crystal is placed into the spectrometer by hand and can be up to several

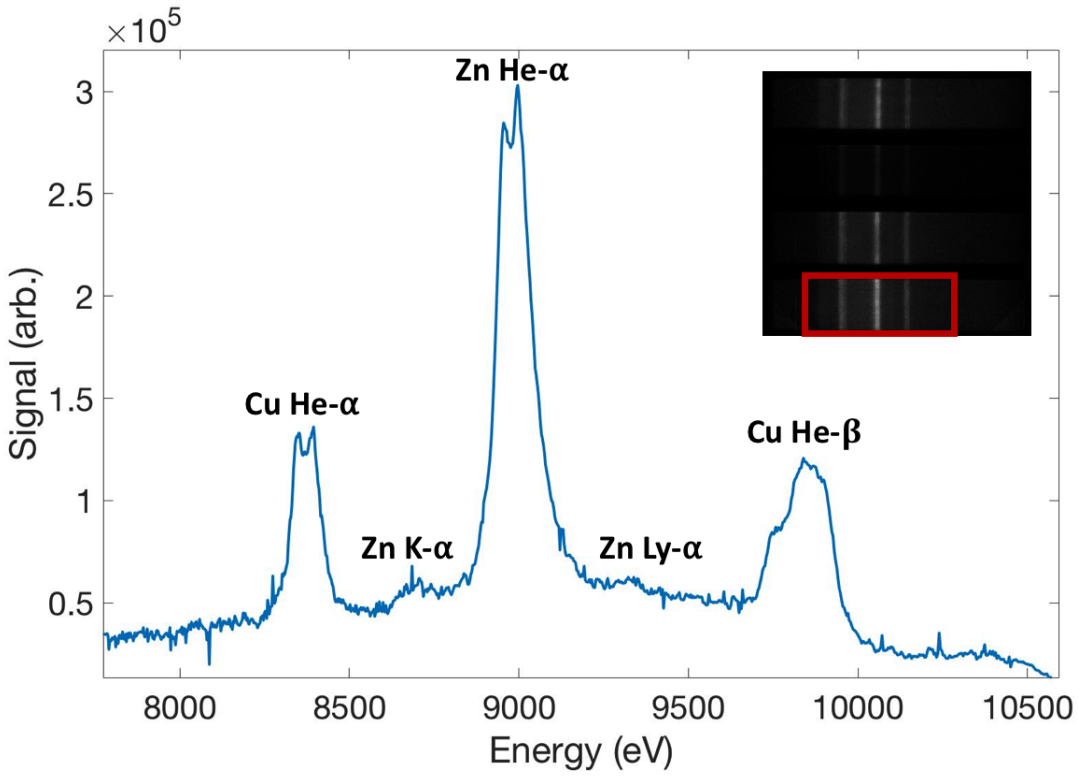

Figure 4.9: A line-out of one strip from a shot on a brass foil which has been calibrated for dispersion. The Cu He-α (8.347 and 8.392 keV), Zn K-α (8.639 keV), Zn He-α (8.950 and 8.999 keV), Zn Ly-α (9.318 keV), and Cu He-β (9.862 and 9.875 keV) emission lines are labeled. Dispersion is calibrated by comparing calculated dispersion curves with the positions of the emission lines.

millimeters off from the design position.

To calibrate the distances used in the dispersion calculation, we generate emission lines at known energies to make a map between pixel number and photon energy. This is done by measuring the emission spectrum from a brass foil. The emission lines from the Cu and the Zn in the brass provide enough points to calibrate the spectrometer. Figure 4.9 shows a calibrated line-out from one such brass foil shot. The three lines used to calibrate the dispersion are Cu He-α (8.347 and 8.392 keV), Zn He-α (8.950 and 8.999 keV), and Cu He-β (9.862 and 9.875 keV) [127]. The points of pixel number versus energy are then compared to calculated dispersion curves with different focal lengths and center energies until a best fit is found.

Once the dispersion is calibrated, there are several other effects that need to be taken into account. The CCD in ZSPEC records the number of counts per spatial bin. Because different regions get "squeezed" or "stretched" due to non-linear dispersion, the integral of the counts beneath the spectral curve needs to be conserved by dividing each point on

the spectrum by a factor of $\Delta E/\Delta x$. This has the effect of raising the red side of the spectrum and lowering the blue side. Spectrometer filtering also affects x-ray transmission, and the observed spectrum should be divided by the filter transmission curve. Often the only filtration is millimeter-thick beryllium, which has a slowly varying opacity function over the energy range of scattering. This also results in raising the red side of the spectrum.

The final correction to the spectrum involves subtracting any shaped x-ray background, which often generates significant uncertainty in spectral processing. Since the shape of the XRTS spectrum reveals the plasma conditions, subtracting any form of shaped background complicates interpretations. If the experiment is well shielded, the background subtraction will be a simple DC offset, in which a constant is subtracted from all points on the spectrum. In the case of a thermal x-ray background, a polynomial function can be fit to the background shape and then subtracted from the spectrum. This has been performed in the past [75], but is known to greatly increase error in the final conclusions. Another option on the OMEGA laser is to take a separate shot without the XRTS drive beams to obtain a background measurement that can then be subtracted from the scattering spectrum; however, this reduces the number of data-shots available and does not account for any background that might be created by the Zn drive.

To summarize, here are the steps that must be taken to generate a spectral line-out from the image-based data:

- Take a lineout of the data along the dispersion direction
- Perform flat-field correction to account for crystal nonuniformities
- Calibrate energy dispersion by matching emission lines of known energies with calculated spectrometer dispersion curves
- Account for dispersion distortion by dividing each point on the spectrum by the calculated $\Delta E/\Delta x$
- Divide by filter transmission profiles
- Subtract background signals

Once the modified line-out is attained as described by the above list, the spectrum can be fit to reveal the plasma conditions.

4.4 Extracting Plasma Parameters from XRTS Spectra

The shape of the spectrum depends on the experimental geometry and the plasma conditions of the scattering sample, as described in Chapter 3. To extract the plasma parameters, we use a forward fitting technique. That is, we generate theoretical scattering spectra for a set

of input parameters, such as scattering angle (which is set by the experimental geometry), electron temperature, mass density, and ionization state, and then compare the resulting calculations to the data.

4.4.1 χ^2 Fitting of Spectra

We compare the theoretically generated spectra with the experimental data via a χ^2 fitting technique. In the case that there are N data points in the spectrum, each with value x_i and variance of σ_i^2, the χ^2 is defined as:

$$\chi^2 = \frac{1}{\nu}\sum_i^N \frac{(x_i - \mu_i)^2}{\sigma_i^2} \ , \tag{4.4}$$

where μ_i is the associated value of the point of the theoretically generated fit and $\nu = N - n$ is the number of degrees or freedom, or number points minus the number of fitting parameters [137]. The closer the χ^2 value is to 1, the better the fit. Fitting certainties can be associated with certain χ^2 values; with two fitting parameters, a χ^2 of 2.28 corresponds to 2σ certainty.

In the case of XRTS data, it can be difficult to obtain independent measurements for the variance of each point, σ_i^2. In that case, the χ^2 values can be fit and absolutely calibrated by the fact that the probability of all solutions must sum to unity. In order to do this, the fitting parameters should be generated on a fine mesh with dimensions set by the number of fitting parameters. Theoretical fits should be generated for each point in the mesh and the χ^2 values calculated using a best-estimate for the variance of each point. The mesh should span a large enough space such that the χ^2 values approach their limiting value of ∞ on all borders. This will generate an oval-like "island" χ^2 plot in 2-D space. The probability of each point is related to the χ^2 value by [137]:

$$P(\chi^2) \propto (\chi^2)^{\frac{\nu-2}{2}} e^{\frac{-\chi^2}{2}} \ . \tag{4.5}$$

All points on the χ^2 surface can then be normalized by the fact that the total probability must sum to unity, and the resulting χ^2 can be obtained through back calculation. In practice, generating a normalized χ^2 fit "island" from XRTS data is often unfeasible, as the island can be cut off by physical limits, such as temperatures below zero and nonphysical ionization states.

As mentioned above, it can be difficult to obtain an accurate and independent value of σ_i^2 for each point on the XRTS spectrum. σ_i^2 should scale with $\sqrt{\text{Counts}}$, where the number of counts refers to the number of detected photons. However, ZSPEC is not absolutely calibrated. In the case that normalizing the full probabilities to unity is not an option, we generate a theoretical best fit to the data and calculate the variance of that fit. That variance is then used as the variance for all points in the data. Because of this method, care must be taken before interpreting χ^2 fitting certainties as error bars, as often things like background

subtraction contribute substantially more to error [75, 138]. However, the χ^2 fits do provide a way of interpreting sensitivity to fitting parameters and can be used to generate error bars in the case that background subtraction and other steps in data processing do not contribute significantly.

4.4.2 The MCSS Code

We use a code called Multi-Component Scattering Spectra (MCSS) [98, 138] to generate theoretical scattering spectra to compare with the data and extract plasma conditions. A collaborator at the Atomic Weapons Establishment in the United Kingdom developed the code to improve upon the models used in previous XRTS simulation codes [97, 139]; MCSS accounts for different plasma components, whereas previous work relied on average atom approximations [98]. The code allows the user to select different physics models for the different components in the Chihara decomposition based on the experimental geometry and anticipated plasma conditions in the sample. For instance, experiments that probe at a large k-value are suited to different models than experiments that probe in the collective regime at low k, and degenerate plasmas can require different treatment than classical plasmas. In this section, I outline the methods used by the code to generate scattering spectra and highlight the most frequently used physics models for the data analysis performed in this thesis.

The code itself is user friendly and quick to run; it takes only a matter of seconds to generate a single scattering spectrum. Figure 4.10 shows an example of an input deck file designed to generate a scattering simulation from a mixture of beryllium and argon. The setup block of the deck file specifies the output mode of the code; the code can be run in angular or spectral mode. Spectral mode generates a scattering spectrum for a given scattering angle. Angular mode calculates the scattering components like S_{ii} as a function of k and is useful for characterizing the scattering regime and understanding the contributions of different components to scattering spectra. The plasma block allows the user to specify the plasma conditions, such as temperature, density, and ionization state. If the user specifies a mean charge state, the code automatically generates populations of whole charge states above and below the specified mean state such that the average charge evens out to the user's specification. In addition, the user can specify population densities of atomic species; Figure 4.10 shows an example with 95 at.% (atomic percent) beryllium and 5 at.% argon. The probe block specifies the x-ray source conditions, which can be a source spectrum from a file or a Gaussian or Lorentzian source. The detector block contains all the details about the spectrometer, including energy ranges and the scattering angle. The code is able to average over different scattering angles in the case of significant k-vector blurring. The models block contains all the approximations used for the components of the Chihara decomposition. These models will be discussed in detail below.

To use the code, one generates a deck file with parameters relevant to the experiment. A front-end processor, such as Matlab, may be used to vary the desired fitting parameters, such as temperature, density, and ionization states, and to calculate the χ^2 fit to the data. Matlab contains machine learning algorithms, which can be used to find the best fit to the

```
$SETUP
    mode_of_operation = "XRTS_SPECTRAL"
    number_of_ions = 2
$END
$FILE
    output_file_name = "out/omega_be_out.csv"
    status_file_name = "stat/omega_be_status.txt"
$END
$PLASMA
    use_mean_charge_states = .TRUE.
    atomic_number = 4, 18
    ionization_state = 2.4, 8
    density_fraction = 0.95, 0.05
    mass_density = 8.3
    temperature = 14
$END
$PROBE
    probe_energy = 8979
    use_source_func_data = .TRUE.
    source_func_file_name = "data/source_functions/source_mit_foil_shot_lowbg_convflat.csv"
$END
$DETECTOR
    number_of_points = 1000
    min_scat_energy = 7000
    max_scat_energy = 11000
    scattering_angle = 135
    number_of_angles = 1
    min_scat_angle = 130
    max_scat_angle = 140
    angle_dist_fwhm = 5
    angle_dist_power = 2
$END
$MODELS
    ee_pol_func_model = "BORN_MERMIN"
    ee_lfc_model = "STATIC_INTERP"
    ipd_model = "STEWART_PYATT"
    ii_potential_model = "DEBYE_HUCKEL"
    screen_cloud_model = "FINITE_WAVELENGTH"
    ei_potential_model = "EFFECTIVE_COULOMB"
    sec_core_power = 6, 6
    calibration_energy = 8620
$END
```

Figure 4.10: An example of a deck file used to run the MCSS code for an experiment that collects back-scattered spectra from a mixture of berylium and argon. The SETUP block specifies basic conditions such as the number of atoms and the output of the code, the PLASMA block specifies plasma parameters such as mass density and temperature, the PROBE block characterizes the x-ray source function, the DETECTOR block determines the scattering angles and energy bandwidth of collection, and the MODELS block specifies the physics models for the different components in the Chihara decomposition.

spectrum. However, sometimes the best fit occurs for a non-physical set of parameters, such as sub-zero temperatures. In addition, the χ^2 fit can possess several local minima. Because of this, it is often more efficient to generate a large grid of plasma conditions that varies density, ionization, and temperature. Spectra and χ^2 values can be calculated for all points on the grid, and the best fit can be found by observing the fits over the whole parameter space.

While MCSS is an immensely powerful and user-friendly code, it does possess limitations. For one, the code is inherently 0-D; one can only generate a scattering spectrum from a single condition. This presents problems for more complicated scattering geometries, in which scattering arises from multiple sets of conditions. In that case, additional efforts must be made to compute 3-D effects, such as source-broadening and x-ray attenuation due to opacity. In addition, the code uses simplifying models to calculate scattering spectra. The next section discusses the modeling in more detail. But as with any simplifications, the user needs to have a detailed understanding of the regimes of validity for all models. Overall, the MCSS code provides an effective way to fit spectral data and understand spectral sensitivity to plasma parameters.

4.4.3 Models Used by the MCSS Code

The code is convenient to use for fitting spectra because it run quickly, but the speed arises from simplifications to scattering models used to compute theoretical spectra. Thus, as in any simulation, the user must understand the approximations behind the code in order to evaluate whether or not the code produces a reasonable and physical simulation. The approximations and models in the code are described in detail by the user manual [138, 98]. Here I summarize the most frequently used models.

As described in Chapter 3, the semi-classical Chihara decomposition breaks the dynamic structure factor into three terms. In view of a multicomponent treatment, the three components can be written in terms of their overall weighted contribution to scattering, W, as:

$$W_{tot} = W_C^{ff}(\vec{k},\omega) + W_C^{bf}(\vec{k},\omega) + W_R(k)\delta(\omega) \ , \tag{4.6}$$

where the first two terms represent free-free and bound-free scattering and compose the inelastic (or Compton) peak, and the last term represents the Rayleigh weight of elastic scattering [138, 98]. The first two terms can be written in terms of their dynamic structure factors as:

$$W_C^{ff}(\vec{k},\omega) = \left(\frac{\omega_s}{\omega i}\right)^2 \sum_a x_a Z_a^f n_i S_{ee}(\vec{k},\omega) \ , \tag{4.7}$$

and:

$$W_C^{bf}(\vec{k},\omega) = \left(\frac{\omega_s}{\omega i}\right)^2 \sum_a x_a Z_b^f n_i S_{ea}(\vec{k},\omega) \ , \tag{4.8}$$

where both equations sum over all ion species a, Z_a^f is the number of free charges per ion species, Z_a^b are the number of bound charges per ion species, x_a is the partial number density

fraction of ion species a, and S_{ee} and S_{ea} are the free-free and bound-free dynamic structure factors, respectively [139]. The total Raleigh weight can be written as:

$$W_R(k) = \sum_{a,b} \sqrt{x_a x_b} n_i [f_a(k) + q_a(k)][f_b(k) + q_b(k)] S_{ab}(k) \ , \tag{4.9}$$

where $f(k)$ are the atomic form factors, $q(k)$ are the screening cloud contributions, and S_{ab} is the partial structure factor for correlations between ion species a and b [140, 98].

Both free-free and bound-free transitions contribute to the inelastic, peak of the scattering spectrum. The Chihara decomposition treats the free electrons as a free electron gas with the ions generating a uniform charged background [96]. In order to calculate the free-free structure factor, the code must calculate the retarded polarization function of the plasma, which determines the behavior of the free electron density in response to the total effective potentials of the fully interacting system [98]. In the non-interacting limit, the retarded polarization function can be modeled using the random phase approximation, which only keeps the lowest order term in the expansion of the the polarization function expression. In order to account for correlations in denser plasmas, the RPA can be modified with local-field corrections [62]. Experiments that probe with large k-values can can approximate the local field corrections with their static limits, whereas a dynamic treatment must be used for collective scattering at lower k-values. In the case that the characteristic relaxation rate of electron distributions due to collisions with ions is large, the Born-Mermin approximation can be used to account for electron correlations with ions. A local field correction can be added to account for electron correlations. In running the code, we model the electron polarization function with the Born-Mermin ansatz, and then add dynamic Hong-Lee local field corrections; these are generally agreed upon as the current best models for the free-free structure factor in warm dense matter [98].

The bound-free term accounts for electrons that undergo Raman-like transitions from bound states into the continuum. The total bound-free dynamic structure factor can be found by summing over each occupied sub-shell around an ion using the Kramers-Heisenberg formula. Different approximations for the effects of each sub-shell apply to different k-value limits. In the limit that $k \to \infty$, the impulse approximation (IA) may be used. The impulse approximation ignores the binding energy of the nucleus, and treats the initial and final states of the electron as plane waves. Several un-tested corrections can be made to IA to account for the asymmetry of the Compton profiles of the bound states. In theory, the best correction would be to treat the initial state of the electron as a bound state with the form factor approximation. However, current work on modeling the bound-free term with the form-factor approximation shows disagreements with most scattering data [98]. Thus, the current best estimate for the bound-free term is found with the impulse approximation. In running the code, we model the bound-free feature with a slightly modified impulse approximation that accounts for edge effects near the binding energies of the electrons. In general, there is much room for improvement in modeling of the bound-free feature, as the shape of the feature depends on the available energy states of the electrons and thus the atomic models.

Elastic scattering comprises three components: the ionic form factors ($f(k)$), the screening cloud contributions ($q(k)$), and the ion-ion structure factors ($S_{ii}(k,\omega)$). The values of $f(k)$, $q(k)$, and $S_{ii}(k,\omega)$ all depend on the magnitude of the scattering vector, $k = \frac{2}{c}\omega_i \sin\theta/2$, which depends on the frequency of incident radiation, ω_i, and the scattering angle, θ. The ionic form factor, $f(k)$, provides the dominant contribution to elastic scattering, and is the Fourier transform of bound electrons around an ion species. $f(k)$ can be represented by a sum over all bound electron states, as [98]:

$$f(k) = \sum_{n,l,m,\sigma} f_{n,l}(k) \; . \tag{4.10}$$

The individual $f_{n,l}$ are typically constructed with the screened-hydrogenic approximations [98, 141], although other simplifications have also been used [142]. The screened hydrogenic approach to constructing the ionic structure factor is widely accepted as the best available method.

There is less consensus behind the modeling of the electron screening cloud's contribution to elastic scattering, which contributes to uncertainties in interpreting elastic scattering signal strength. The electron screening cloud contribution arises due the response of the free electrons to the ions; the quantified contribution is particularly uncertain in the partially-ionized warm dense matter regime [98, 105]. Several different approximations can be used to calculate $q(k)$, including finite-wavelength screening at larger wave numbers and Debye-like Debye-Hückel screening at smaller wave numbers. Other approximations used to calculate the screening cloud contribution to elastic scattering vary the treatment of the potential between the electrons and the ions. A typical approximation for this potential is the effective Coulomb potential, which replaces the nuclear charge with an effective charge that accounts for the nucleus and the free electrons. Other models include the hard empty core treatment, which generates an empty core of zero charge inside a user-imposed radius of bound electrons [98]. However, finite wavelength screening has been observed experimentally [105], and so remains the most-frequently used model for the screening cloud contribution.

Another contribution to the strength of elastic scattering is the static structure factor, $S_{ii}(k)$, which arises from spatial correlations of the ions. Typical approximations used to account for the potential governing ion-ion interactions include an effective coulomb potential that is ideal in weakly ionized systems or a Debye-Hückel potential for fully ionized atoms with weak coupling. More work is being done to develop a finite-wavelength screening model and a short-range repulsion model ideal for dense and partially ionized plasmas, but Debye-Hückel remains the model we use in the code to model scattering spectra.

It should be noted that there is a lot of uncertainty as to whether or not fitting the data with MCSS is the best way to extract plasma conditions from the scattering data [9, 107, 108]. As the Chihara decomposition allows different components of the spectrum to be modelled independently, spectra can be fit using physics models that are not self-consistent. In addition, the Chihara decomposition forces the definition of an average charge state. In warm dense matter, the definition of ionization is not fully clear, as the material is often too

dense for the electron to ever become fully part of the continuum [143]. Finally, because the code allows for many different input parameters, good fits to the spectrum can sometimes be found in non-physical regimes. Thus, much recent work focuses on modeling spectra outside of MCSS and outside of the Chihara decomposition [9, 23, 107, 108]. However, these techniques require significant computing resources. Thus, because of its speed and ease of use, MCSS remains a useful tool for understanding fitting sensitivities and benchmarking fits to different plasma conditions.

Chapter 5

X-ray Thomson Scattering and Radiography from Imploding Diamond Spheres on the OMEGA Laser

As a culmination to the XRTS platform development work, we collected high quality scattering data from directly-driven 1 mm diameter single-crystal diamond spheres during a Laboratory Basic Science one-day campaign. This chapter outlines the motivation for the work and discusses the results and and conclusions from the shot day.

5.1 Introduction

Understanding the behavior of matter at extreme conditions is crucial to laboratory astrophysics and experiments that pursue inertial confinement fusion. Both experimental areas rely on an accurate equation of state (EOS) model, which describes how matter heats and compresses in response to an applied pressure. Modern static compression experiments can reach pressures up to 7 Mbar, at which point valence and conduction bands begin to distort and material chemistry begins to change. Planar dynamic compression experiments from laser-driven shocks and flyer plates can reach pressures up to 100 Mbar, at which point basic chemical properties break down and the EOS becomes dominated by the thermal motion of the ions. Pressures exceeding 100 Mbar can be reached by lasers that dynamically compress solid capsules in spherically convergent geometries, at which point pressure-induced ionization begins to dominate the material's response. The EOS models begin to deviate as materials reach such high energy densities, which are orders of magnitude greater than found on Earth's surface. Equation of state studies of some materials with pressures up to 3.6 Gbar were completed using nuclear and chemical explosives during the age of underground testing [144, 145, 146]. However, to date, there lacks sufficient experimental data

from modern compression techniques to benchmark EOS models at these high pressures.

Dynamic compression experiments generate high pressures by launching a shock wave into a material. The Hugoniot relations describe the locus of thermodynamic states that can be reached by single-shock compression from the ground state. Much recent theoretical and experimental work has focused on the modeling of the Hugoniot of carbon-based materials [74, 147, 148, 149, 150, 124, 121] because of the prevalence of carbon-based materials as ICF ablators [52, 50], it's relevance to astrophysics, and ease of use. Diamond is a material of particular interest, as recent campaigns on the National Ignition Facility [57] obtained higher neutron yields in fusion experiments when using high density carbon (HDC) ablators [54]. Experiments have studied the shock Hugoniot in diamond in detail up to pressures of 26 Mbar [148, 151, 152, 153] and the equation of state of ramp-compressed diamond up to pressures of 50 MBar [154]. However, there remains a dearth of Hugoniot data at higher pressures, at which point EOS models begin to diverge in their predictions of material behavior [16, 10, 155]. Experiments using spherically convergent geometries can generate pressures exceeding 1 Gbar [156, 124, 125, 121, 126]. As the shock wave coalesces towards the center, mass accumulates in the shock front and the pressure differential between shocked and unshocked material increases [124]. The increasing pressure allows experimenters to probe multiple points along the shock Hugoniot in a single shot with use of time-gated instruments.

Because of the high densities of compressed solid spherical samples, the penetrative power of x-rays is often used to measure the plasma properties. One such diagnostic is x-ray radiography. In a radiography experiment, an x-ray backlighter shines through a sample as the sample compresses, and a time-gated camera measures the intensity of light after it passes through the sphere. The amount of light absorbed by the sample can be used to infer the sample's density, and the time-resolution of the camera allows for resolution of the shock speed. From these two inferred quantities, the pressure in the sample can be obtained from the Hugoniot relations. The use of radiography to determine plasma densities in a variety of experimental geometries is well documented in the literature [157, 158, 159]. X-ray radiography has also been demonstrated to measure the Hugoniot of a solid spherical sample in a spherically convergent geometry at pressures approaching 1 Gbar on the National Ignition Facility [125]. Results from spherically convergent NIF experiments show the promise to measure the EOS of materials at higher pressures than previously recorded [121].

Another x-ray diagnostic suited to measure plasma parameters of dense matter is x-ray Thomson scattering (XRTS). In an XRTS measurement, an narrow-band x-ray source impinges on a plasma sample and a spectrometer measures the scattered x-ray profile at a designated scattering angle. The Compton-shifted profile of inelastically scattered x-rays reflects the electron velocity distribution, and thus the density and temperature, and the number of elastically scattered x-rays depends on the number of tightly bound electrons, and thus the ionization state [62]. The use of the inelastically scattered x-rays to infer density and temperature is well documented in the literature [6, 100, 60, 5], and much recent work has used the elastic feature to determine properties such as ionization and structure factors [103, 61]. A recent XRTS measurement on solid spherical samples on the NIF used radiography

in conjunction with XRTS to understand the ionization of carbon at 200 Mbar [75, 126]. The measurement found that the carbon in the shock front ionized more than predicted by commonly applied IPD models. More data at similar pressure ranges is needed to constrain EOS modeling at such high pressures.

While solid capsules in spherically convergent geometries offer the ability to reach unprecedented pressures, they present challenges in data interpretation. X-ray radiography measurements rely on an accurate understanding of the opacity of the dense material in the shock front, as the measured x-rays pass through all areas of the sample; however the opacity of warm and hot dense carbon is still an area of active discussion [160, 161]. In addition, XRTS measures mass-averaged conditions, which can also be affected by the opacity of the material. A previous analysis of an XRTS measurement from a solid spherical sample on the NIF determined that XRTS can measure the opacity-weighted mass-averaged conditions of the sample, but the ability to measure average conditions depends on the linearity of the scattering response to plasma parameters [75, 162]. It is thus of importance to perform more XRTS and x-ray radiography experiments in conjunction to refine our understanding of how capable these two measurements are of refining EOS models at high pressures.

To that end, we developed a platform on the OMEGA laser facility [56], which performs x-ray radiography and XRTS measurements on solid spherical samples. In this chapter, we present initial measurements from one millimeter diameter solid single-crystal diamond spheres. We use the radiography measurements to generate post-shot radiation hydrodynamics simulations of the implosions and confirm that the simulations accurately represent the mass density profiles of the compressing spheres. We then perform a full analysis on the XRTS data to determine the electron density and average ionization state in the sample. Finally, we discuss the successes and challenges in the interpretation of the data, and present methods to improve upon this data in the future.

5.2 Overview of Experimental Setup and Data Collection

Here we present the two platforms used to take either x-ray radiography or XRTS measurements from directly driven spheres on the OMEGA laser. The platforms are designed to work in series with each other, such that experimenters can alternate between the two in a shot day. In both platforms, 52 beams point at the sphere at target chamber center and drive the implosion with a 26 kJ, 1 ns square pulse, beginning at time $t = 0$ ns. The drive beams are used with phase plates to smooth the laser profile on the sphere. Six backlighter beams point at a 5 μm thick Zn foil mounted in a cone above the sphere and heat the foil with a 3 kJ, 1 ns square pulse at the time the measurements are to be made. The Zn emits He-α radiation, which serves as the x-ray source for both XRTS and x-ray radiography. The samples are single-crystal 1 mm diameter diamond spheres obtained from Dutch Diamond Technologies. The company quotes a density of 3.52 g cm^{-3} and roundness of $\leq$ 250 nm.

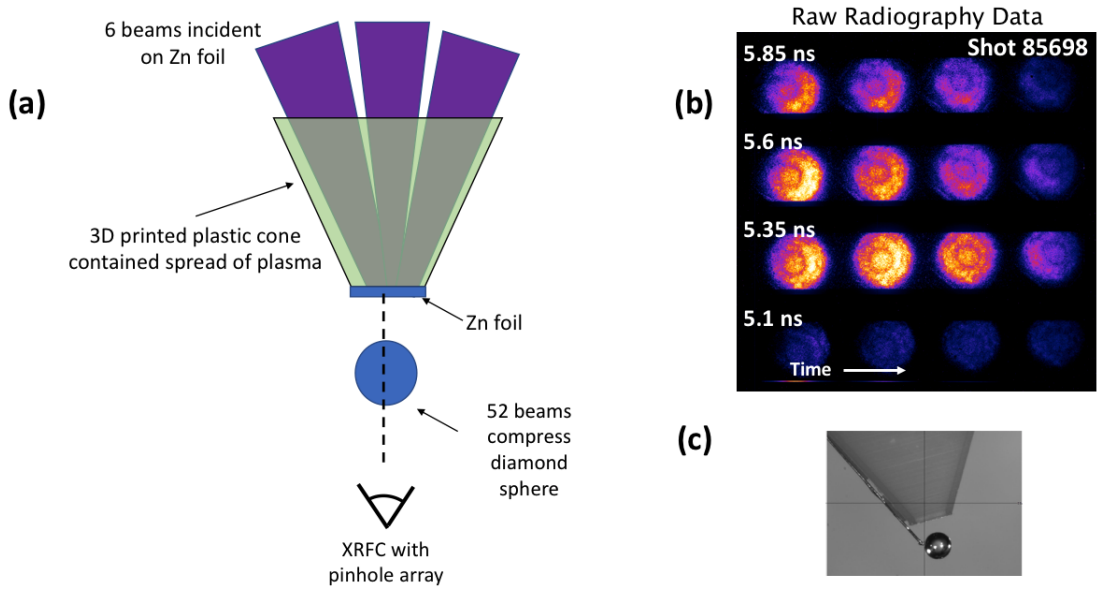

Figure 5.1: (a) A schematic of the experimental setup for the radiography shots. 52 beams drive a diamond sphere directly for 1 ns. 6 1-ns-long beams heat a Zn x-ray backlighter later, during the implosion. Zn x-rays that pass through the sphere are collected by a time-gated x-ray framing camera with a pinhole array. (b) Raw radiography data. (c) A side-view picture of the target.

The single-crystal diamond has a concentration of single substitutional nitrogen of less than 100 parts per billion.

Figure 5.1(a) shows a schematic of the radiography platform and Figure 5.1(c) shows a picture of the target. For radiography, the backlighter lasers are focused to make a 900 mm spot on the Zn foil to backlight the sphere. The Zn foil is suspended at the bottom of a 3D printed plastic cone, which contains the outwards spread of the Zn plasma. The cone is opened at an angle to allow enough beams to reach the Zn foil. X-rays from the Zn are collected on the opposite side of the sphere by a time-gated x-ray framing camera (XRFC) with a pinhole array. The framing camera collects 2-D images of the compressing sphere, as seen in Figure 5.1(b). Each vertical strip begins recording at a different time in the implosion, as indicated by the labels at the beginning of the strips. Each individual image integrates over roughly 50 ps, and the time difference between the first and last image in a strip is approximately 150 ps.

Figure 5.2(a) shows an experimental schematic for the XRTS platform. As with the radiography measurement, a 200 μm thick 3D printed plastic cone contains the spread of the Zn plasma. 60 μ-thick Au foils layer over the plastic cone to block the spectrometer's direct line-of-sight to the Zn foil. The gold foils are coated with 5 μ of CH plastic in order to prevent the gold from accidentally becoming heated by direct laser irradiation or

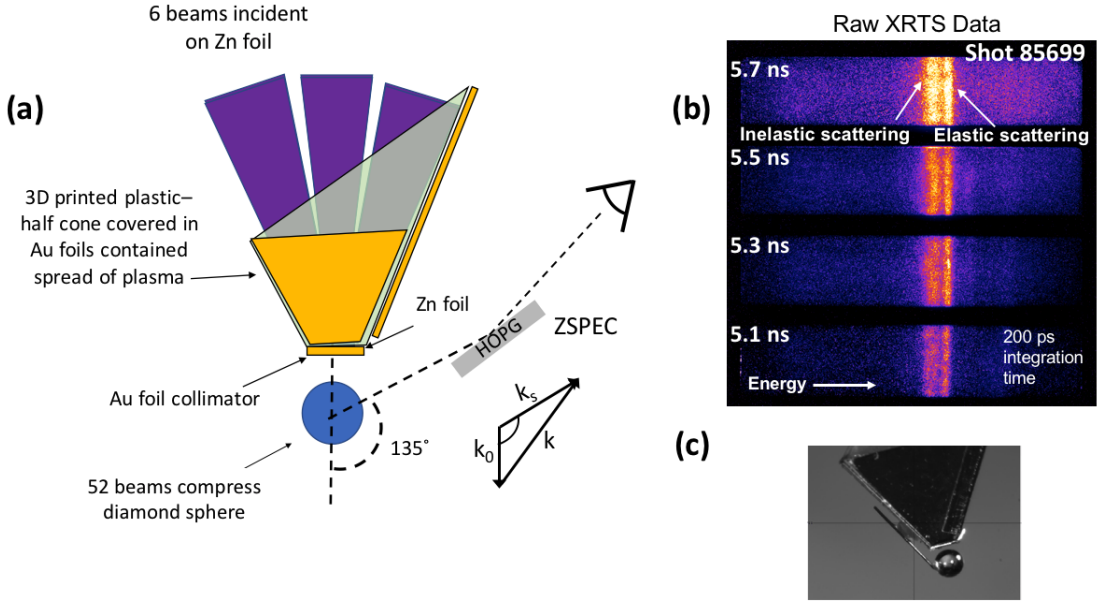

Figure 5.2: (a) A schematic of the experimental setup for the XRTS platform. 52 beams compress the sphere directly for 1 ns. 6 beams heat a Zn x-ray backlighter for 1 ns later in the implosion time. Zn x-rays that scatter through the sphere are collected by a HOPG crystal spectrometer attached to a time-gated x-ray framing camera. (b) Raw XRTS data from one shot. (c) A sideview picture of the target.

hot electron interactions. The backlighter lasers are focused to a 300 μm spot on the Zn foil. The spectrometer is located at a scattering angle 135°. However, the shielding cone is thick enough such that a portion of the sphere is not visible to the spectrometer, which means scattering arises from a scattering angle of $118 \pm 5°$. The spectrometer, ZSPEC, is described in Chapter 4. Raw data can be seen in the upper right side of Figure 5.2. Each strip integrates over 200 ps, and is gated to begin at a different time, as indicated at the beginning of each strip.

The following sections outline the theory behind scattering from inhomogenous samples and perform a full analysis of the radiography and XRTS data in order to return important information on the ionization in HEDP conditions.

5.3 X-ray Scattering from an Inhomogenous Sample

A scattering spectrum that arises from homogeneous conditions is easy to analyze because one electron temperature, one electron density, and one ionization state suffices to describe the plasma conditions. However, there are many cases in which a scattering measurement from an inhomogeneous sample is desired, such as in the case of solid spherical samples. If the

sample is relatively transparent to the probing radiation, the resulting scattering spectrum measures the mass averaged conditions of the sample. For a spherical sample, the mass averaged conditions are calculated by:

$$\langle x \rangle = \frac{\int_0^\infty x(r)\rho(r)r^2 dr}{\int_0^\infty \rho(r)r^2 dr} \ , \tag{5.1}$$

where $x(r)$ is the radially dependent plasma condition to be averaged and $\rho(r)$ is the mass density. However, because spherically convergent geometries reach such high densities, it is often the case that the sample attenuates a fraction of the x-ray probe source and opacity effects must be taken into account. The detailed effects of opacity in a spherical sample are summarized in Reference [162]. Opacity shifts the bulk of material that does most of the scattering to the outer radii of spheres, as the x-rays are attenuated as they penetrate inwards. Thus, the bulk of the scattering occurs from the warm and dense inwardly moving material.

In addition, scattering spectra from large targets can suffer from the effects of k-vector blurring. A previous analysis of scattering from solid density spheres determined that the scattering spectrum was still well represented by the mass weighted averages, despite opacity and k-vector blurring effects [75]. However, opacity and k-vector blurring should always be considered when analyzing scattering from a large object, as there are regimes in which the mass-weighted averages might not well represent the scattering spectrum [162].

5.4 Results from Radiography and Generation of Post-Shot Simulations

We collected data from two radiography shots, with images spanning 5.3 - 7.8 ns in the implosion. Figure 5.3 shows an image of the raw radiography data with key features marked. The inner circle in each image represents the region of maximum absorption, which corresponds with the high-compression, shocked material. We tracked the region of maximum absorption as a function of time to measure the shock speed. Figure 5.4 shows a plot of the measured shock radius as a function of time as the sphere implodes. We then used these measurements to tune 1-D radiation hydrodynamics simulations with HYDRA [53] to have the same implosion trajectory.

The post-shot simulations of mass density and electron temperature versus radius are shown in Figure 5.5. Each color represents a different snapshot in time. The simulations are calculated with the tabulated Livermore equation of state for diamond, LEOS 9064. A red box denotes the conditions over the times we measured. We anticipate up to 10 eV and three times compression in the shock front, which amounts to pressures of up to 50 Mbar. The Fermi temperature of three times compressed diamond is roughly 35 eV, which means the plasma is partially degenerate at temperatures temperatures we expect to measure (10 eV and lower).

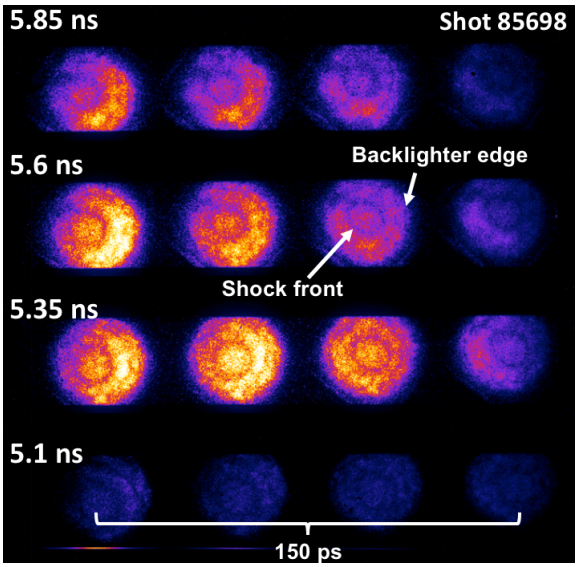

Figure 5.3: Raw radiography data from OMEGA shot 85698. Each strip is gated to measure at a specfic time and takes four images. The first and last images are separated by 150 ps, and the times quoted on the left of the strips refer to the timing in the middle of the strip. Each image integrates over 50 ps. The outer edge of each image is the edge of the laser spot on the foil backlighter, and the inner circle is shock compressed material.

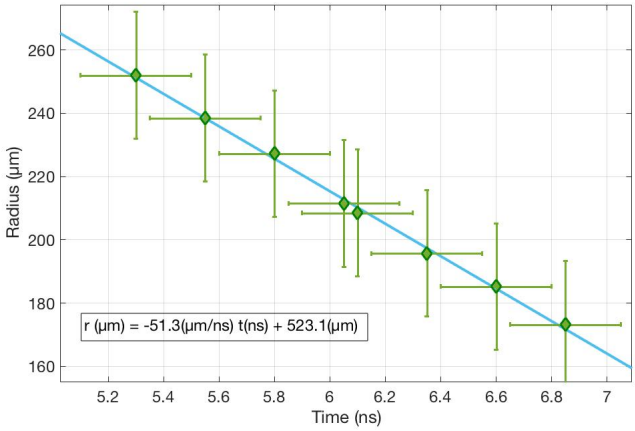

Figure 5.4: A plot of the measured radius of the shocked material versus implosion time. A straight line was fit to the data to return a shock speed of 51 ± 10 μm ns^{-1}.

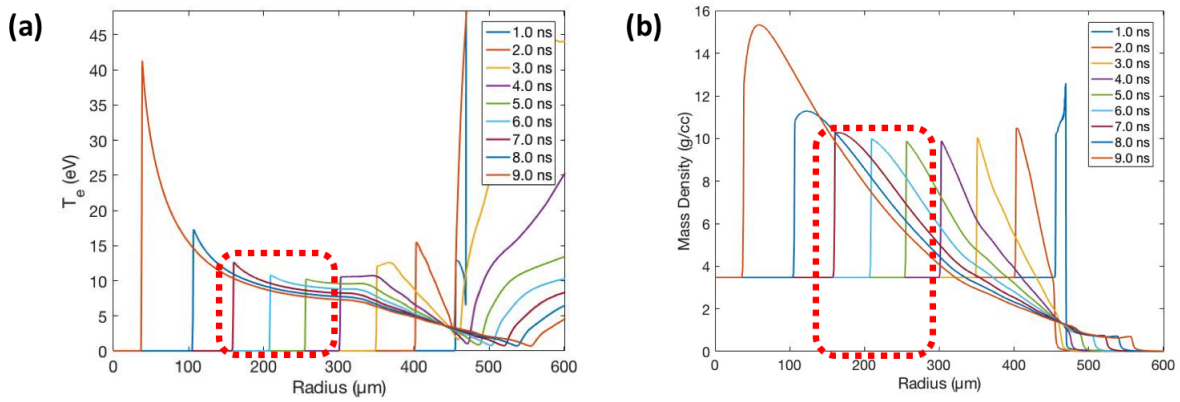

Figure 5.5: Radiation hydrodynamic simulations of electron temperature and mass density as a function of radius. Each color is a different snapshot in time. We expect up to 10 eV and three times compression in the shock front at the times we measured (boxed in red). The simulations use a tabulated equation of state with ionization calculated by a Thomas-Fermi-like model.

We then validated the simulated radial density profiles by comparing simulated transmission profiles with the radiographs. At temperatures of < 10 eV and densities < 10 g cm^{-3}, carbon is not expected to ionize into its K-shell (above $Z_C = 4$) . Thus, the cold opacity suffices to simulate x-ray transmission. Using a mass attenuation coefficient of $\mu = 3.225$ cm^2/g, we calculated the transmission through each point on the sphere by:

$$I(x,y) = I_0(x,y) \int_0^{z_{max}} e^{-\mu\rho(x,y,x)z} dz \tag{5.2}$$

where $I(x,y)$ is the measured 2-D intensity profile, $I_0(x,y)$ is the initial 2-D intensity profile of the laser spot on the radiography foil backlighter, and z is the dimension through which the x-rays pass. We simulated the laser spot size as a 2-D super Gaussian with FWHMs representative of the laser profile on the foil. Because the precise position of the laser spot varies between strips due to measurement parallax, we altered the central (x,y) coordinates of the laser spot to match the radiography images. We then scaled the maximum intensity of I_0 to match simulated transmission line-outs as a function of sphere radius.

Figure 5.6 shows an example comparison of the radiography data to the simulated transmission profiles. Figure 5.6(a) shows the raw radiography image at 6.5 ± 0.2 ns. Figure 5.6(b) shows the laser spot profile on the backlighter foil, and (c) shows the corrected image, which divides the radiography image by the scaled laser intensity profile. Figure 5.6(d) shows the simulated transmission line-out at 7.0 ns compared with a radial transmission line-out from the data. The simulations show good agreement with the data in the region of the shock and outward, which implies that the simulations predict the radial distribution of density to within 20%. There is a discrepancy of 0.5 ns in the timing between the simulations and the

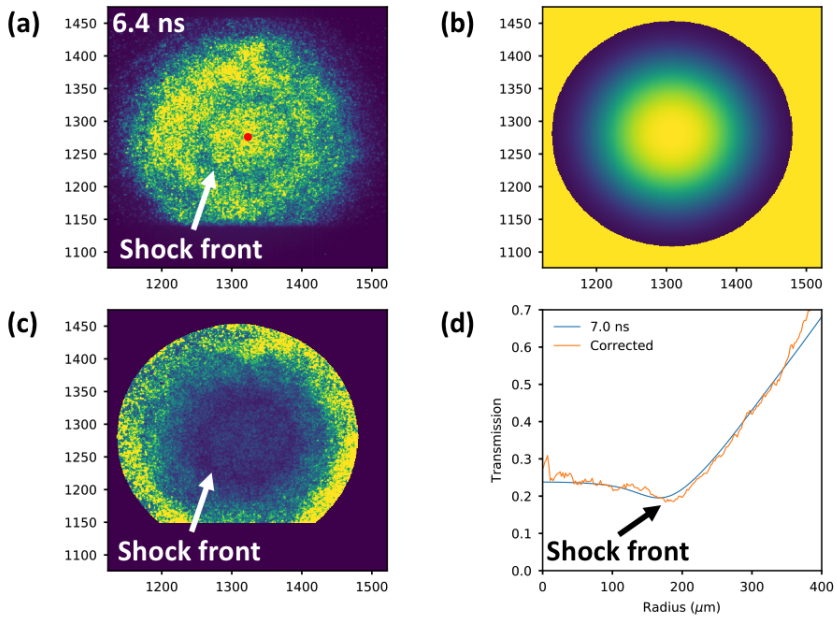

Figure 5.6: An example of calculating the simulated transmission through the sphere. (a) Radiography data from shot number 85697, taken at 6.5 ± 0.2 ns with arrow indicating position of shock front. (b) The laser spot profile on the backlighter foil. (c) The corrected radiography image, which divides the radiograph by the scaled laser intensity. (d) Radial lineouts of transmission profiles from the corrected data compared to the simulated transmission lineout at 7.0 ns. The transmission data show good agreement with the simulations, except for an offset in shock timing of 0.5 ns which is within the margin of error from analysis shown in Figure 5.4.

data, however, this discrepancy is within the margin of uncertainty from the shock timing analysis seen in Figure 5.4.

By verifying that the simulated transmission profiles match the radiographs, we benchmark one important aspect of the simulations: namely, that the simulated radial mass density profiles match those same profiles as observed in the experiment. Using this information, we can now constrain the mass density to that predicted by the simulations. This reduces the number of fitting parameters available in the XRTS analysis and increases confidence in the modeling of the experiment.

5.5 Analysis of XRTS Data

We measured XRTS spectra from two different shots. Figure 5.7 shows two processed spectra, one from each shot. The shots were performed at different times in the implosion, which separated the spectra in time by 1.1 ns. Each spectrum integrates over roughly 350 ps and

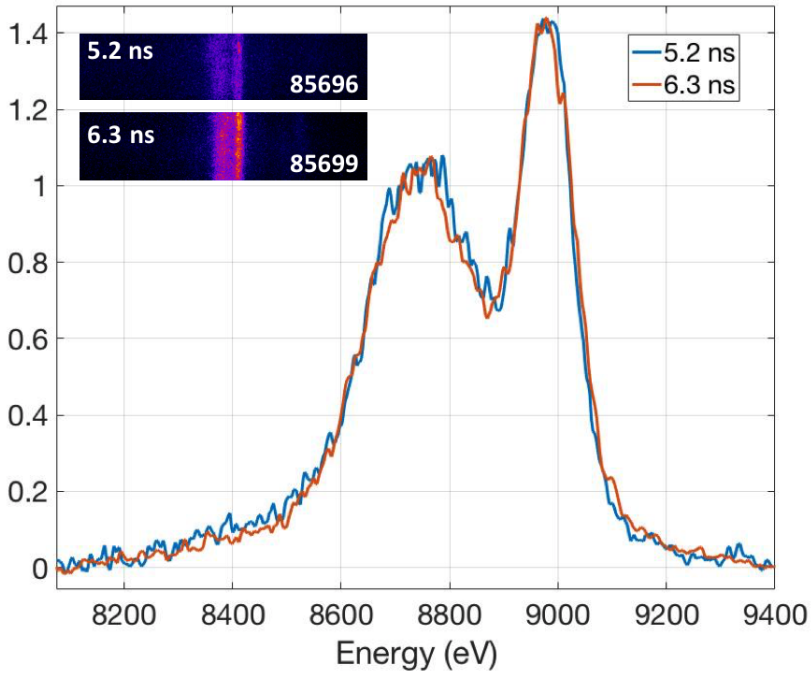

Figure 5.7: Line-outs of XRTS spectra from two different shots. Each spectrum integrates over 350 ps. The two spectra are qualitatively very similar.

is the result of summing spectra from two different strips of the detector together to account for potential HOPG crystal defects. Both spectra are qualitatively similar in shape and in the ratio of elastic to inelastic scattering, which implies they are probing similar plasma conditions. As described above, XRTS measures the mass-weighted average conditions of the sample as a first-order approximation. The simulations show that over the times we probed, the mass-weighted conditions change by less than 5%. Thus, we would expect the two spectra to appear similar.

The average conditions we measure are also expected to stay relatively constant if we account for the effects of opacity. Figure 5.8(a) shows a slice of a 3-D weighting map of scattering intensity from the diamond spheres, where the brighter regions indicate more scattering. The weighting is calculated by the method outlined in Reference [162], and the weight of any point i is calculated by the intensity of light at that point, I_i, multiplied by the density, ρ_i, to give: $W_i = I_i \rho_i$. The high density region of shocked material absorbs x-rays as they penetrate inwards. This causes most of the scattering to occur from a region behind the shock front. Absorption of the x-rays also casts a scattering "shadow" on the region of the far sides of the sphere from the detector and the x-ray source. In our samples, the large shielding cone blocks the spectrometer's line-of-sight to roughly half the sphere, which results in a weighting map as shown in Figure 5.8(b). The result of the cone is to limit scattering to one small region of the sphere, which limits the effects of k-vector blurring.

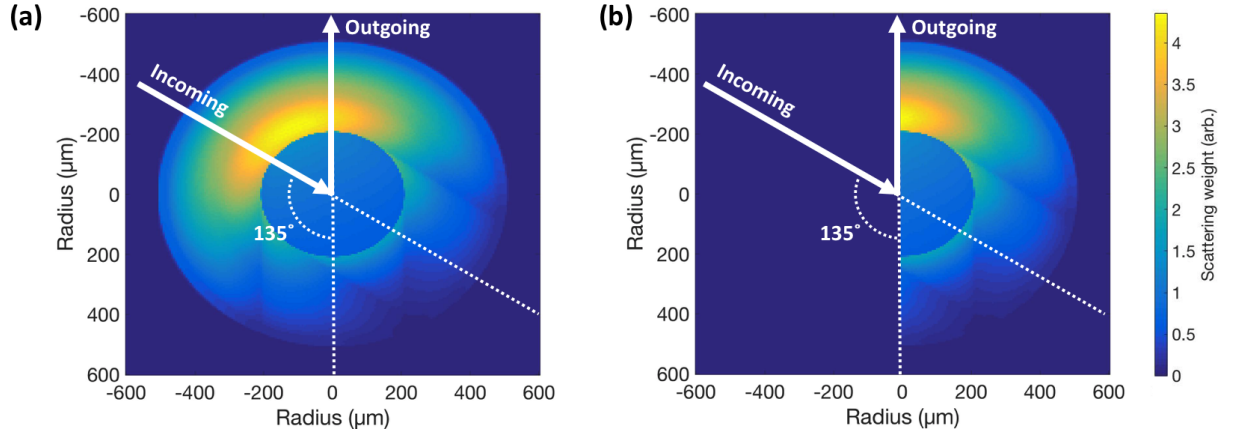

Figure 5.8: (a) A slice of a 3-D weighting map of scattering intensity at 6.0 ns, accounting for the opacity of compressed diamond. The brighter regions indicate a higher portion of scattering. The net effect of opacity is to shift the scattering weighting to regions at higher radii at one point in the sphere (b) The same slice of the opacity map, with the half of the sphere that the spectrometer does not see blocked out. The cone ensures that scattering happens from a small portion of the sphere, limiting the effects of geometric blurring.

Because the shielding cone slices the weighting map along a symmetric axis, the average plasma parameters we measure from the obstructed view of the sample are very similar to the conditions we would measure from the full sample.

We can now characterize scattering weights as a function of radius r by summing values of the 3-D weighting maps within $r + \Delta r$ for the whole sphere. However, it is important to keep in mind that the radial weighting maps are deceptive, as the majority of the scattering happens from a given radius at a specific azimuthal and polar angle due to the effects of opacity and the shielding cone. Nevertheless, it is useful to characterize the scattering by this method in order to understand the conditions from which the bulk of the scattering arises. Figure 5.9 shows the radial distribution of scattering weights and the respective radial distributions of mass density (a), electron temperature (b), and ionization state (b) at 6.3 ns, assuming half the sphere contributes to the scattering. The majority of scattering occurs from a radius of roughly 400 μm, which is in the moderately dense region behind the shock front. Scattering is expected to arise from the average conditions of: $\langle \rho \rangle = 4.0$ g cm^{-3}, $\langle T_e \rangle = 6$ eV, and $\langle Z_C \rangle = 2.2$. The ionization in the simulation was predicted by a Thomas-Fermi (TF) model, which assumes smooth ionization as a function of temperature and pressure and does not account for atomic shell effects [84]. TF predicts an unphysical average ionization state of $Z_C = 2.5$ for the cold, uncompressed diamond, which we replace with the much lower ionization state of $Z_C = 0.1$. However, very little scattering arises from the cold portion of the sphere, so any substituted ionization state of the cold mattering will not impact the results of the fitting.

We can now generate a full simulated scattering spectrum using the effects of opacity

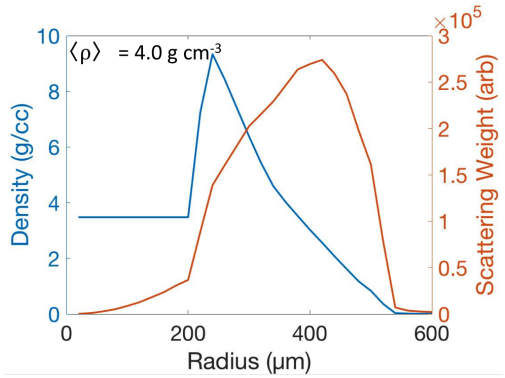

(a) Scattering weight of ρ.

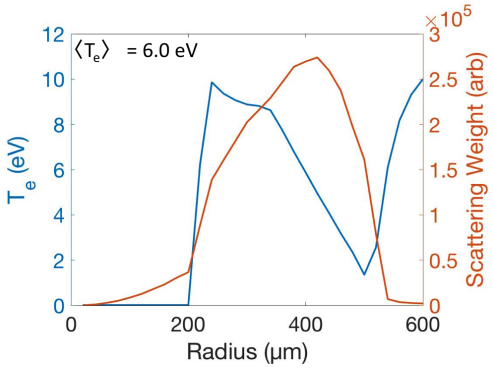

(b) Scattering weight of T_e.

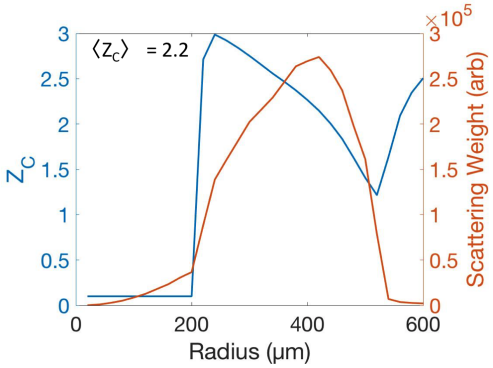

(c) Scattering weight of Z_C.

Figure 5.9: The radial weighting of scattering at 6.0 ns plotted with simulated radial profiles for density, temperature, and ionization state from HYDRA [53]. The majority of scattering occurs from a radius of roughly 400 μm, which is in the region behind the shock front. Scattering is expected to arise from the average conditions of: $\langle\rho\rangle = 4.0$ g cm^{-3}, $\langle T_e\rangle = 6$ eV, and $\langle Z_C\rangle = 2.2$.

weighting. We divide the radius into N bins, each of a small enough Δr such that the conditions are effectively uniform between r and $r + \Delta r$. We then generate single condition scattering spectra, S_i, using the average density, temperature, and ionization state of each radial bin, i. We sum the weighted single condition spectra to generate the full spectrum by:

$$S_{full} = \sum_{i}^{N} S_i W_i \tag{5.3}$$

where W_i is the relative weighting of the bin i, as seen in Figure 5.9.

Figure 5.10 shows a comparison of two simulated scattering spectra. Both spectra average over scattering angles of $118° \pm 5°$, which is the angular spread dictated by the geometry of the experiment, and use a measured Zn He-α source. The blue curve represents a single scattering spectrum from the opacity-weighted average conditions in the sample. The red

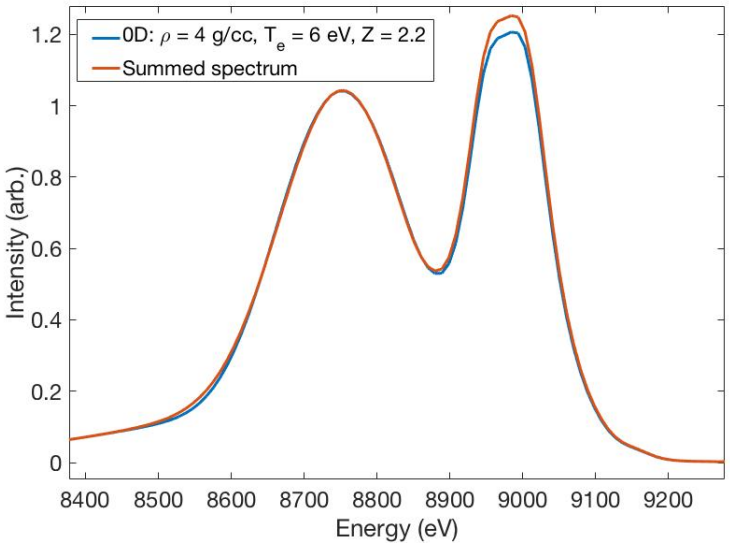

Figure 5.10: Comparison of two theoretical scattering spectra. The blue curve is a single scattering spectrum generated at the expected average conditions. The red curve is the summed scattering spectrum which accounts for the inhomogeneities of the plasma. The two spectra are very similar, except for a slight difference in the magnitude of elastic scattering. This is because most of the scattering arises from a single portion in the sphere.

curve is the summed spectrum that accounts for the inhomogeneities in the sample. Both spectra are qualitatively very similar, except for a slight discrepancy in the elastic peak; this arises from nonlinearity of S_{ii} with respect to the temperatures in the material.

We first analyze the inelastic feature of the scattering data using a 0-D approach as the inelastic feature of the opacity-weighted summed spectrum matches that of the 0-D approximation. The radiography data confirmed that the simulations predict the mass density profile of the spheres to within 20% accuracy, so we hold the mass density constant to the predicted average value of (4.0 ± 0.8) g cm^{-3} in our fitting; however, the lower bound of possible densities is set by the physical limitation that compressed diamond cannot have an average density lower than the ambient density of 3.5 g cm^{-3}, which means the range of possible average densities is limited to values between 3.5 and 4.8 g cm^{-3}.

With the average mass density set to the expected value of 4.0 g cm^{-3}, we vary the average electron temperature and ionization state to calculate χ^2 fits to the inelastic feature of the spectrum. Figure 5.11 shows the χ^2 fit with 1σ confidence intervals marked by the dashed white lines. The inelastic feature shows much more sensitivity to ionization state than temperature. This is to be expected, as our plasma is degenerate and the electron velocity distribution width depends more on electron density than on temperature; since we hold the mass density constant, varying the ionization state linearly changes the electron density. Figure 5.11 shows that at the predicted electron temperature of 6 eV, an average

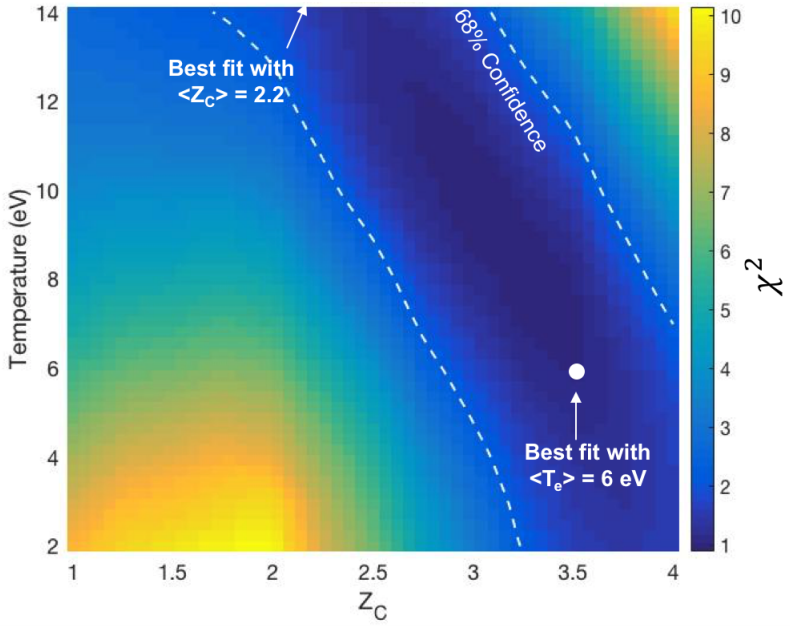

Figure 5.11: A χ^2 plot of fitting to the inelastic portion of the spectrum, varying electron temperature and carbon ionization (read: electron density). The white dashed lines represent the 1σ confidence intervals. In order to reproduce the width of the Compton feature at the predicted average temperature of 6.0 eV, an average carbon ionization of $\langle Z_C \rangle = 3.5 \pm 0.5$ is required, which amounts to an average electron density of $\langle n_e \rangle = (7.0 \pm 1.0) \times 10^{23}$ cm^{-3}.

ionization state of $\langle Z_C \rangle = 3.5 \pm 0.5$ is required to reproduce the data, which corresponds to an average electron density of $(7.0 \pm 1.0) \times 10^{23}$ cm^{-3}. This is significantly higher than the predicted average ionization of 2.2 and electron density of 4.4×10^{23} cm^{-3}.

If we repeat the same analysis with the mass density set to the extremes of the possible values of 3.5 and 4.8 g cm^{-3}, we again find that a fit with an average ionization state of $\langle Z_C \rangle = 2.2$ and average electron density of 4.4×10^{23} cm^{-3} is incapable of reproducing the data and the electron density must take a value of $(7.0 \pm 1.0) \times 10^{23}$ cm^{-3}. It is also worth noting that for all possible mass density values, in order to fit the data with the average electron density of 7.0×10^{23} cm^{-3}, an average temperature of (18 ± 4) eV would be required, which is three times higher than the simulations predict. Because this seems unphysical, the rest of the analysis assumes the predicted average temperature of 6 eV. However, as discussed in Chapter 4, the trade-off between density and temperature in fitting spectra increases uncertainty in the analysis. In this case, the increased sensitivity of spectral fits to electron density warrant holding temperature constant for the remainder of the fitting.

We now seek to understand the discrepancy between the average ionization required to fit the inelastic peak and the average ionization predicted by simulations. We calculate several opacity-weighted summed spectra, each with a different radial ionization profile. The radial

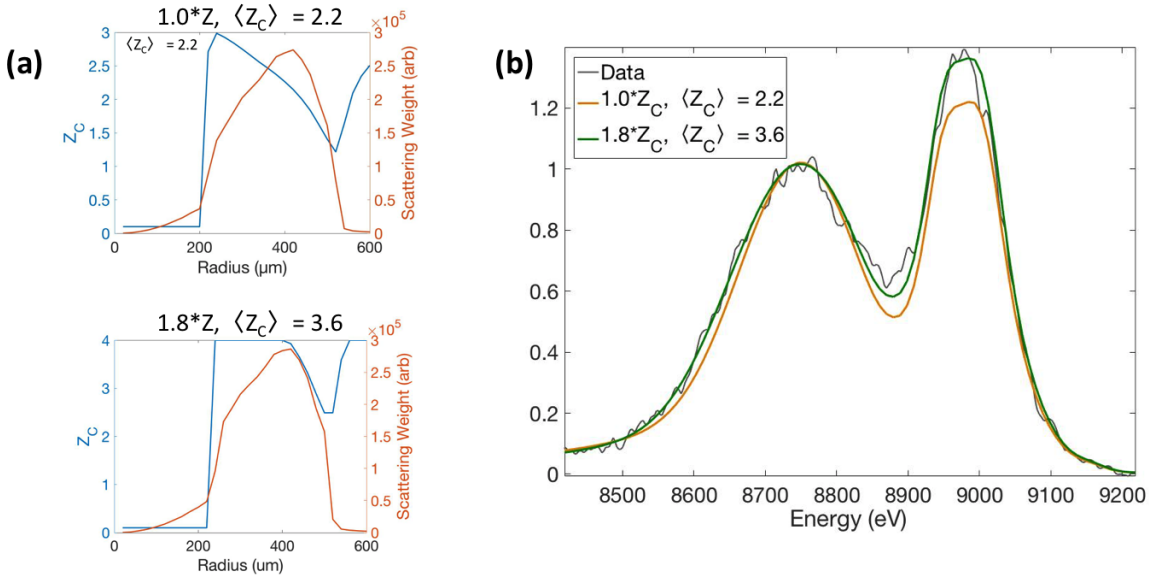

Figure 5.12: a) Radial ionization profiles and radial scattering weights for the ionizations predicted by the simulations (top) and the same ionizations artifically scaled by a factor of 1.8 (bottom). The simulations predict an average ionization state of $\langle Z_C \rangle = 2.2$, but by artificially increasing the ionization we obtain $\langle Z_C \rangle = 3.6$. b) A comparison of the data to two calculated spectra: one with $\langle Z_C \rangle = 2.2$ and one with $\langle Z_C \rangle = 3.6$. The best fit to the data occurs with an an average ionization state of 3.6, which is consistent with the fits to the inelastic portion of the spectrum.

ionization profiles differ by a factor of a constant, which raises the average ionization state. Figure 5.12(a) shows the radial ionization profiles as predicted by the simulations (top) and the same radial distribution of ionization with each point multiplied by 1.8, yielding an average ionization of $\langle Z_C \rangle = 3.6$ (bottom). Note that we account for the carbon shell structure by capping the ionization states at $Z_C = 4$, as no ionization into the K-shell is predicted to occur. By this method, the average ionization can increase to a maximum value of $\langle Z_C \rangle = 3.8$ for all reasonable values of the constant multiplier, as the cold, unshocked regime prevents the average from increasing all the way to $\langle Z_C \rangle = 4$.

Figure 5.12(b) shows the spectrum taken at 6.3 ns plotted with two different summed spectra: one using the simulated profiles for ionization and one with the ionization artificially increased from the simulated values by a factor of 1.8. The curve that best reproduces the shape of the inelastic feature and the strength of elastic scattering is the curve that increases the average ionization state to $\langle Z_C \rangle = 3.6$, which is consistent with our previous finding from analysis of the inelastic peak. It is worth noting that no appreciable difference is seen between a spectrum with $\langle Z_C \rangle = 3.6$ and a spectrum with average ionization increased up to the maximum of $\langle Z_C \rangle = 3.8$; both of these conditions correspond with the majority or all of the material behind the shock front ionization to $Z_C = 4$. We can repeat a similar

analysis with the spectrum at 5.1 ns, which similarly finds that ionization must increase to an average value of $\langle Z_C \rangle = 3.6$ to reproduce the data. The limitation in this method of fitting is an inability to determine the precise radial profiles of the ionization; we can ascertain the average conditions, but not the conditions at any one point. There are multiple possibilities for radial ionization profiles that generate the average ionization states required to reproduce the data. Of course, these can be bounded by the range of physicality, but we are unable to benchmark the radial ionization profiles any further.

The fact that the majority of carbon behind the shock front must ionize to $Z_C = 4$ in order for spectral fits to reproduce the data is consistent with a previous OMEGA experiment on carbon-based materials in a similar temperature and pressure regime; the experiment similarly found that the Thomas-Fermi model under-predicted ionization in warm dense carbon [5]. Thus, an ionization model that includes shell effects should be used in the EOS for future simulations in order to better predict the behavior of the compressed material.

5.6 Conclusions and Proposed Extensions

In this chapter, we used radiography data from imploding diamond spheres to generate post-shot simulations of the implosion. We then analyzed the transmission profiles to find that the simulations accurately predict the radial density profile of the compressing spheres. We fit the inelastic component of the XRTS spectrum with 0-D simulations to determine that the predicted average ionization state (and thus electron density) was too low to reproduce the elastic scattering width. An average ionization state of $Z_C = 3.5 \pm .5$ was required to match the data at 6 eV, which corresponds with an electron density of $n_e = (7.0 \pm 1.0) \times 10^{23}$ cm^{-1}. We then simulated scattering spectra from the full, inhomogenous sphere that varied the predicted ionization state. We found that the carbon in the shocked region needed to ionize up to the carbon K-shell, to produce an average ionization state of $Z_C = 3.6$, which was consistent with the analysis of the inelastic scattering feature. We thus concluded that the Thomas-Fermi model underpredicts the ionization of warm dense carbon.

The results from this experiment warrant further exploration. Firstly, more scattering and radiography data should be collected from earlier and later in the implosion time in order to benchmark the simulations more rigorously. Although we found the simulations accurately predicted the radial mass density profile over the times we measured, a more comprehensive measurement would increase our confidence in the modeling. Ionization affects the compressibility of the material and so could affect the progression of the shock, especially as the sphere becomes more and more compressed near the end of the implosion.

Furthermore, it is worth noting that in this case, we did not take full advantage of the spherically convergent geometry in order to probe multiple points in the shock Hugoniot.This is due to the slow time scale of the implosion and the fact that the shock wave decays over the times we measured. In order to measure different compression ratios, smaller samples could be used such that peak compression happens before the rarefaction wave reaches the shock front. Smaller samples would also amount to less k-vector blurring and less opacity effects,

which would reduce the complications in interpreting scattering data. In addition, more extreme conditions could be reached in the shocked material of smaller diamond spheres, potentially allowing us to measure the onset of K-shell ionization in carbon.

The combination of radiography and XRTS in convergent geometries offers experimenters the ability to probe the equation of state of materials at high pressures by measuring the ionization of the sample. The results from such experiments will help refine the models that predict the behavior of capsule implosions.

Chapter 6

Influence of Argon Impurities on the Elastic Scattering of X-Rays from Imploding Beryllium Capsules

Another example of a spherically convergent XRTS platform on the OMEGA laser is compressing spherical shells. Spherical shells have more homogeneous conditions than solid spheres but still reach extreme conditions, so can make ideal scattering targets. Several Livermore scientists collected scattering data from imploding beryllium shells and used the inelastic scattering peak to determine the temperature and density as a function of time [60]. We reanalyzed the elastic feature and determined that there was a trace argon impurity in the sample. The remainder of the chapter discusses the analysis.

6.1 Introduction

In this chapter, we assess the impact of a small (around one percent by number density) argon impurity fraction on the elastic scattering signal strength from beryllium plasmas. Our results demonstrate that careful impurity characterization is important for accurate ionization measurements using the elastic component of XRTS. Moreover, we show that intentional doping of mid- or high-Z elements into low-Z samples might provide a path towards studying ionization potential lowering of higher-Z elements, which might be not possible otherwise due to the high opacity of the pure mid-Z sample.

In an XRTS experiment, a collimated x-ray source impinges on a sample, and a spectrometer spectrally resolves the scattered photons at a desired scattering angle. XRTS spectra typically consist of two major components: elastically scattered photons with the frequency of the original x-ray source and inelastically scattered photons that are down-shifted in frequency. The Compton-shifted profile of inelastically scattered x-rays can be analyzed to return the sample's electron density and electron temperature. The ratio of elastically to inelastically scattered x-rays relates to the number of tightly bound versus free electrons,

and thus reflects the ionization state.

The use of inelastically scattered x-rays to infer electron temperature and density is well documented. Several experiments on beryllium samples used large scattering angles to probe the properties of individual electrons and to measure electron temperatures and densities through analysis of the shape of the Compton peak [99, 100, 60]. Forward-scattering geometries probe the collective behavior of the electrons, i.e. plasmons [6, 102, 163]. The elastic scattering component is often used to infer ion properties such as the static structure factor [104, 164, 5, 30] or the associated screening properties [105]. The Rayleigh weight, which reflects the integral of the elastic scattering peak, relates to the number of tightly bound electrons, which allows investigation of the ionization balance. Recent XRTS experiments found higher ionization states than predicted for a large range of conditions [4, 75].

The static structure factors, atomic form factors, screening properties, and ionization balance measured by XRTS are well suited for a comparison with theoretical modeling. While much progress has been achieved in recent years, there remains a significant need for additional experimental validation of theoretical predictions. In particular, experimental measurements of the properties of warm dense matter are needed for integrated modeling of inertial confinement fusion experiments [35, 165, 51] and astrophysical objects [15, 16, 17, 18]. A particularly interesting question is the behavior of elemental mixtures and how the different components interact with each other and affect x-ray scattering. The mutual interactions and arrangements of different species are predicted to yield signatures in the XRTS spectra. Moreover, one needs to ensure that impurities do not invalidate the results obtained.

In the following sections, we perform a reanalysis of in-flight XRTS data from beryllium capsule implosions that were driven by the OMEGA laser [60]. After reviewing the experiment, its data, and the description of XRTS spectra from multi-component systems, we apply our analysis with special focus on the elastic scattering feature. We find a significant contribution from the argon component to the elastic scattering amplitude, which allows us to determine the argon content of the samples. We also find a strong decrease of the ratio of elastic to inelastic scattering as the capsule implodes, indicating an increasing ionization during compression. Due to the large scattering angle, the data are much more sensitive to the beryllium ionization than to the ionization of the argon impurities. Finally, we give an outlook on possible ways to investigate the ionization of mid-Z ions in high energy density conditions, where highly compressed beryllium provides an environment of high free electron densities and moderate temperatures.

6.2 Overview of Experimental Setup and Data Collection

The experimental data discussed here were obtained from an XRTS experiment undertaken at the OMEGA laser [60]. In this campaign, several time-resolved XRTS spectra were collected from imploding beryllium shells. The previous analysis focused on the inelastic scattering feature, that is the Compton-shifted response of the free electrons and scattering by bound-free transitions. Fitting this feature allowed for the determination of the electron temperatures and free-electron densities at different times, as well as an ionization state of the beryllium from the long tail on the Compton-peak, which derives from scattering from loosely bound electrons [60]. Here, we consider the information contained in the elastic scattering feature to gain insights into the ion properties, mainly the ion charge state, and the contribution of the argon contamination in the beryllium.

Figure 6.1 summarizes the setup of the experiment. The part on the top-left shows a schematic of the cone-in-shell design used for the XRTS measurements: 36 laser beams impinged directly on a spherical beryllium shell for 2 ns. The strong laser-ablation accelerated the spherical sample symmetrically towards the center. Nine additional laser beams heated the zinc to create a pulse of He-α line radiation at 9.0 keV that was used as the probe. The x-rays scattered from the sample and were collected at a scattering angle of 135° by ZSPEC, the Bragg-crystal spectrometer that consists of a highly oriented pyrolitic graphite crystal connected to a gated multichannel plate detector. The zinc foil was glued on the inside of a gold half-cone that served to block the direct line of sight to the spectrometer. A photo of the beryllium target, the backlighter foil, and the gold shield is shown in the bottom-left of Fig. 6.1. The lower right of Fig. 6.1 contains results from radiation-hydrodynamics simulations for the implosion. Here, the density increase to the laser drive is shown together with the laser power and the probing times. All times refer to $t = 0$ being set by the beginning of the laser drive, and peak compression is predicted to occur around 5 ns.

The beryllium targets were 40 µm thick spherical shells with an outer diameter of 860 µm and a density of 1.85 g cm^{-3}. They were also glued directly onto the gold cone, as seen in Figure 6.1. The beryllium contained an argon impurity fraction, μ_{Ar}, as a result of the beryllium sputtering manufacturing process. Argon acts as the sputter gas and participates in the ion-assisted coating of the capsules, which breaks up the columnar structure of beryllium and results in leak-tight capsules. The sputtered capsules usually contain an atomic argon impurity fraction of $\mu_{Ar} = 0.5 - 2.0\%$. In this chapter, impurity concentrations are described by atomic percent (at.%), which describes the fractional ion density of a species. The exact percentage of argon was not characterized in the original experiment. Other impurities in the Be include oxygen, at less than 1 at.% from oxidation of the outer layers of the shells, and trace amounts of iron at roughly 60 parts per million. However, oxygen and iron at these concentrations do not contribute enough bound electrons to affect the elastic

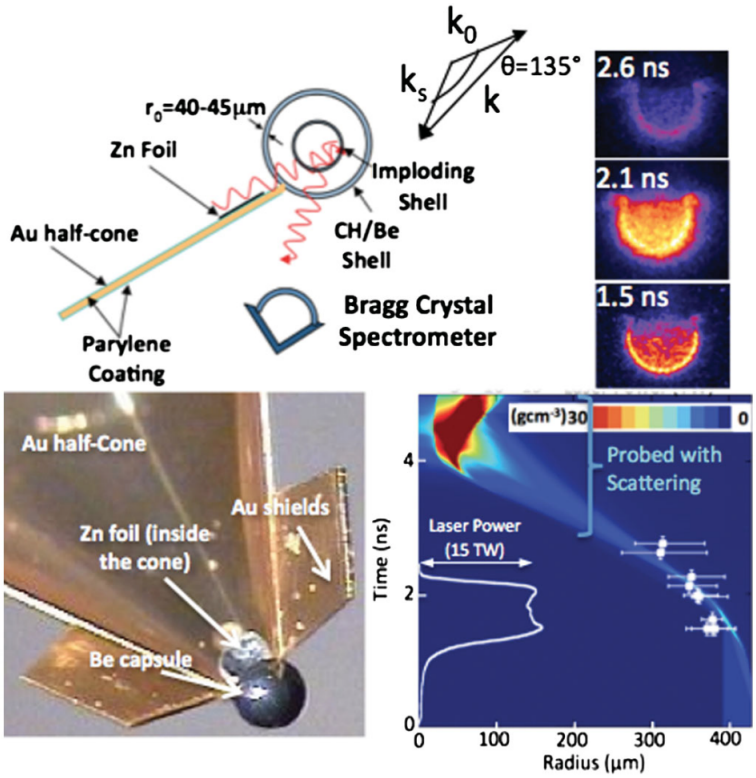

Figure 6.1: Experimental setup of the experiment as presented in Ref. [60]. The top shows the schematic of the experiment and images of the x-ray emission from the sample as it imploded. The bottom displays a photo of the cone-in-shell target as well as outputs from radiation-hydrodynamic modeling of the imploding beryllium capsule. Reprinted figure with permission from A. L. Kritcher, T. Döppner, C. Fortmann, T. Ma, O. L. Landen, R. Wallace, and S. H. Glenzer, Phys. Rev. Lett., **107**, 015002 (2011). Copyright 2011 by the American Physical Society. https://doi.org/10.1103/PhysRevLett.107.015002

scattering signal strength; the remainder of this chapter focuses on the dominating effects of the argon impurity.

XRTS spectra were taken at several times along the implosion trajectory of the beryllium shell [60]. Without accounting for the argon, the strength of the elastic feature could not be reproduced. Thus, only the inelastic component of each scattering profile was analyzed. Nevertheless, the electron temperatures and densities could be determined from the Compton feature at several times during the compression. Here, we will focus on two cases: the spectrum taken at $t = 3.1\,\mathrm{ns}$, yielding an electron temperature of $T_e = (14 \pm 3)\,\mathrm{eV}$ and a free electron density of $n_e = (1.1 \pm 0.3) \times 10^{24}\,\mathrm{cm}^{-3}$, and the spectrum recorded $t = 5.7\,\mathrm{ns}$ after the beginning of the laser drive where $T_e = (41 \pm 5)\,\mathrm{eV}$ and $n_e = (1.9 \pm 0.5) \times 10^{24}\,\mathrm{cm}^{-3}$ was determined [60]. While the first spectrum is one of the earliest, the second is close to peak compression. Based on the reported plasma parameters, we now extend the analysis to the

elastic features of the spectra by accounting for the argon impurity in the sample.

6.3 XRTS Theory for Multi-Component Systems

We give a brief summary of the relevant theory for XRTS with special emphasis on systems containing multiple ion species [140]. A full account of all mutual correlations is necessary here, as we expect strongly coupled ions and a significant difference between the charge states of beryllium and argon.

The total dynamic electron structure factor, $S(k,\omega)$, includes the properties of the correlated system. As the electrons interact with the ions, the structure factor contains information on the electron response and on the behavior of the ions as shown by the widely applied decomposition derived by Chihara [96, 97]

$$S(k,\omega) = W_R(k)\,\delta(\omega) + W_C^{ff}(k,\omega) + W_C^{bf}(k,\omega)\,. \tag{6.1}$$

Here, the first term denotes the near-elastic (Rayleigh) scattering that can be linked to the ion properties. The second and third terms are the inelastic (Compton-shifted) contributions due to the dynamic response of the free electrons and due to bound-free transitions, respectively. The latter two can be calculated on the basis of standard approximations [62]. On this basis, Kritcher *et al.* [60] obtained the basic plasma properties mentioned above that we will use here.

The elastic scattering contribution, i.e. the first term in Eq. (6.1), contains information about the ionic structure. In a system with multiple ion species, all mutual arrangements must be taken into account. Thus, it is necessary to use a multi-component description of the weight of the Rayleigh feature [140]

$$W_R(k) = \sum_{a,b} \sqrt{x_a x_b}\,[f_a(k) + q_a(k)]\,[f_b(k) + q_b(k)]\,S_{ab}(k)\,. \tag{6.2}$$

Here, the elastic scattering is determined by the individual form factors for each species, $f_a(k)$, the individual screening contributions, $q_a(k)$, the fractions of the different ions species, $x_a = n_a/\sum_a n_a$, the number densities, n_a, and all combinations of partial ionic structure factors, $S_{ab}(k)$. In this formula, the argon impurity μ_{Ar} is represented by the fractional number density of one of the species, i.e. x_a. Estimates of the partial structure factors may be obtained from, e.g., the multi-component hypernetted-chain (HNC) approach [139, 166].

6.4 Analysis of the Rayleigh Weights

To investigate the weight of the elastic scattering feature, we fit several raw line-outs of the spectral data with the sums of two Gaussians. One Gaussian fits the elastic feature and the other fits the inelastic feature; the heights and widths of the Gaussians are scaled relatively to each other until the sum of the two Gaussians minimizes the fitting residuals from the

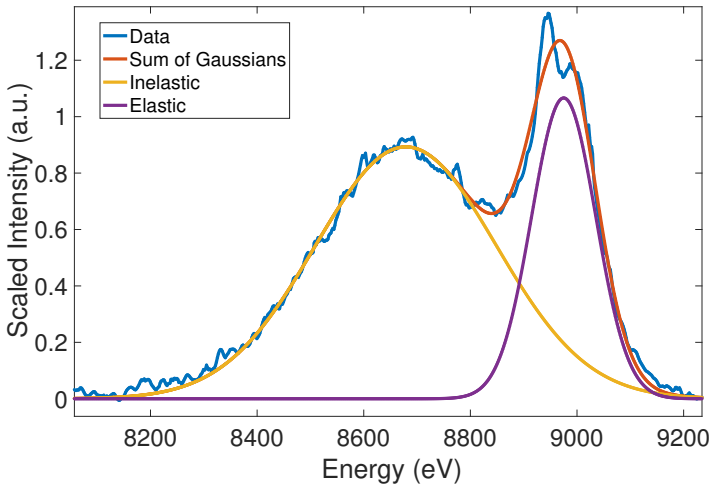

Figure 6.2: (Color online) XRTS spectrum taken at $t = 5.7\,\text{ns}$ after the start of the laser drive [60]. Both the elastic scattering feature on the right as well as the inelastic feature on the left were fitted by Gaussian functions. While the special shape of the zinc He-α line (see shape of the elastic feature in the experimental data) is not accounted for, this procedure generates the correct weights under the two features.

data. We chose to model the probe spectrum as a Gaussian due to the limited spectral resolution of the instrument, and to simplify the initial analysis. An example of the results is presented in Figure 6.2. The deviation at the top of the elastic feature is due to the double peak structure of the zinc He-α incident source, with lines at 8950 and 8999 eV. Besides this feature, fits with two Gaussians represents the data quite well.

The integrals of the Gaussians define the weight of the total inelastic scattering feature and the weight of the Rayleigh peak $W_R(k)$, respectively. The ratio of the two areas is a good measure of their relative strengths and, moreover, independent of absolute signal levels. We thus analyze the time-dependence of the implosion via the ratio of elastic to inelastic scatter.

Figure 6.3 shows the ratios of weights for the elastic and inelastic scattering features for a number of spectra taken at different times during the implosion [60]. The spread in ratios at a given time could be in part due to variations in crystal and framing camera flat fielding, but the trend stands out above the noise in the data; the elastic to inelastic ratio decreases with time by almost 40% as the capsule compresses. This cannot be explained by the heating and compression alone; either beryllium or argon ionization must also contribute to this drop in elastic scattering.

To quantify the effects of compression and ionization, we generated theoretical predictions for the scattering spectra of a sample consisting of beryllium and 0.75% argon. All the theoretical calculations of the scattered power spectra shown in this work are based on the MCSS code [138, 98]. The dynamic contributions, i.e. the free-free and bound-free terms, are

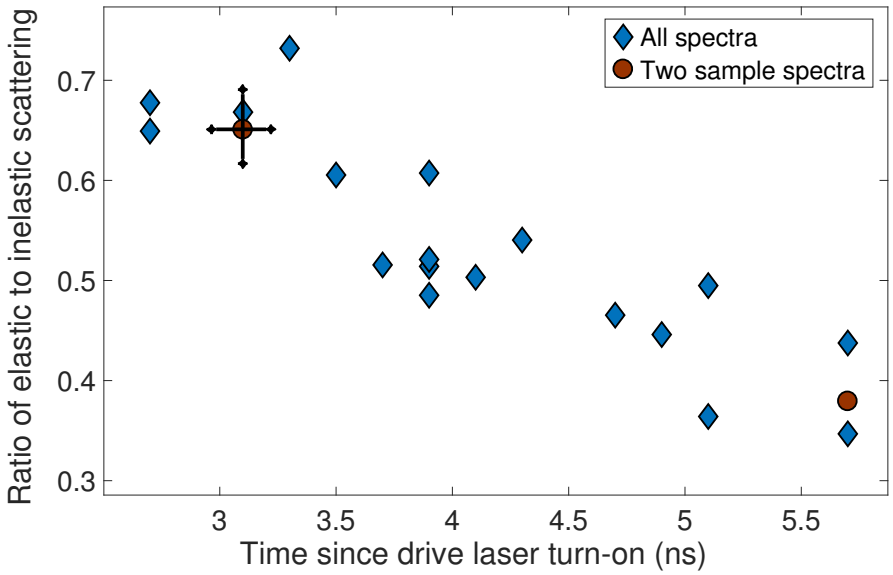

Figure 6.3: (Color online) Ratio of elastic to inelastic scattering strength versus time for spectra taken by Kritcher *et al.* [60]. Each diamond represents the ratio from one spectrum. The laser drive turns on at $t = 0$ and turns off after $t = 2\,\text{ns}$, with peak compression reached at 5.7 ns. Here, we focus on the two spectra marked by red circles (early during the implosion and near peak compression). The red data point at 3.1 ns shows representative 1σ error bars.

well documented in the literature. The elastic scattering contribution to the theoretical power spectra have also been calculated using various commonly-used simple models but, due to its central role in our present work, warrants additional explanation. For the structure of the bound electrons (ionic form factor), we use the usual screened hydrogenic approximation. Here, the effective nuclear charge for each occupied sub-shell is given by the well-known values tabulated by Pauling and Sherman [141]. The structure of the screening cloud has been treated in the finite-wavelength screening formalism [105], which accounts for the short-range Friedel-like density oscillations and also includes a strong coupling correction to the static screening function [167]. The electron-ion potential is considered to be Coulomb-like, with an effective ionic charge consistent with the mean ionization state for each species (Be or Ar). Finally, the spatial correlations of the ions modulating the amplitude of the Rayleigh signal is described using the multi-component HNC approach [139]. For this part of the calculation only the ions are considered (no explicit electron-ion correlations are used) and the inter-ion potential is treated with a statically screened Yukawa interaction; the effective charges of the ions are again assumed to be consistent with the mean ionization states of the components of the plasma. Improvements on these simple models are widely known, e.g. using a pseudo-potential for the electron-ion and ion-ion interactions, although these invariably require additional fitting constants and/or material-specific information which

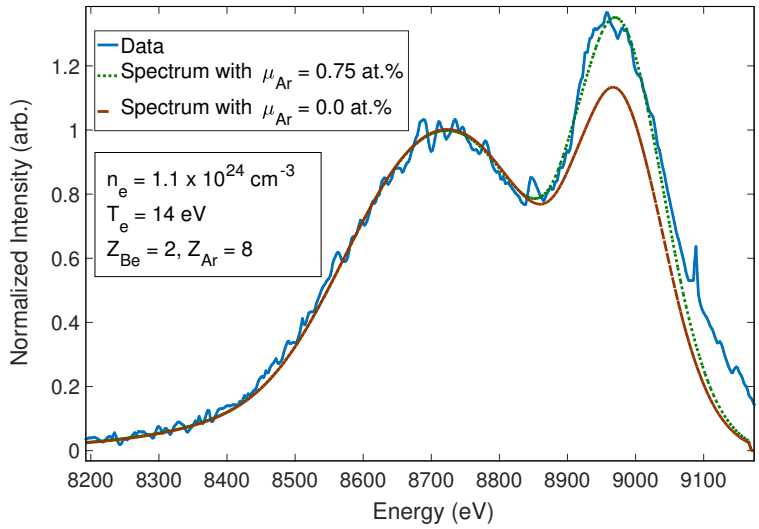

Figure 6.4: (Color online) An XRTS spectrum taken at 3.1 ns [60] compared to two theoretically generated spectra. Both predictions use a source-broadened Zn He-α source, a temperature of $T = 14\,\mathrm{eV}$, an electron density of $1.1 \times 10^{24}\,\mathrm{cm}^{-3}$, and a scattering angle of 135°. They differ only in the assumed argon content: the simulation represented by the solid line neglects the argon in the sample, while the dashed line is a simulation that assumes an argon impurity of 0.75 at.%.

would introduce undesirable extra model uncertainty. The suite of models used here offers a reasonable compromise between physical accuracy and numerical economy and enables the large parameter scans required to undertake the rigorous statistical analysis which underlines our present results.

To represent the x-ray source function, we used a measured Zn He-α spectrum, broadened by the scattering source size. Our theoretical predictions show that at a scattering angle of 135°, the change in plasma conditions from $T = 14\,\mathrm{eV}$ and $n_e = 1.1 \times 10^{24}\,\mathrm{cm}^{-3}$ to $T = 41\,\mathrm{eV}$ and $n_e = 1.9 \times 10^{24}\,\mathrm{cm}^{-3}$ accounts for a 20% decrease of the ratio of elastic to inelastic scattering if the ionization of both ion species is kept constant. Thus, it is reasonable to attribute the remainder of the observed decrease in elastic-inelastic signal strength to ionization. Specifically, the mean ionization of either the Be or the Ar may account for our observations. We now undertake a careful analysis of our experimental data to quantitatively understand the relative sensitivity of the spectra to ionization of either component.

Our theoretical predictions also demonstrate that the elastic scattering signal strength cannot be reproduced without accounting for the argon impurity fraction. Figure 6.4 shows an example for the experimental conditions at $t = 3.1$ ns. To set the ionization, we ran simulations in the atomic kinetics and radiation transport code Cretin; for all available continuum lowering models [83], the code predicted an ionization state of $Z_{Be} = 2.0$ and $Z_{Ar} = 8.0$ over

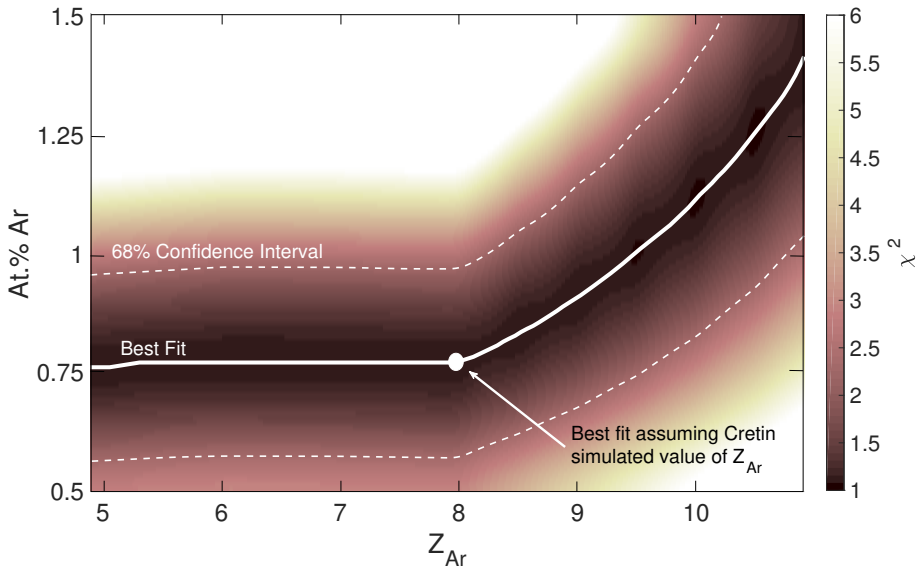

Figure 6.5: (Color online) (a) χ^2 analysis of the elastic scattering feature of the spectrum at 3.1 ns, varying argon impurity fraction and argon ionization. All fits assume $Z_{Be} = 2$, $T_e = 14\,\text{eV}$, and $n_e = 1.1 \times 10^{24}\,\text{cm}^{-3}$, as reported in Ref. [60]. Since the Ar ionization is reported to be $Z_{Ar} = 8$ by Cretin simulations at these plasma conditions, the best fit is obtained for an Ar impurity fraction of $0.75 \pm 0.20\%$.

all combinations of plasma conditions relevant to the spectrum at 3.1 ns [60]. Using the aforementioned values, the MCSS calculations show that adding only 0.75 at.% Ar to the sample increases the elastic scattering by 20% and enables us to match the experimental observation. Thus, it is of great importance to quantify carefully the argon content in the sample and the sensitivity of the elastic signal strength to argon and beryllium ionization. In the following, we will focus on the spectra taken at 3.1 ns and at 5.7 ns, which show a large difference in the ratio of elastic to inelastic scattering.

Figure 6.5 shows the deviation of model spectra to the measured elastic scattering feature of the spectrum taken at 3.1 ns (χ^2 analysis). Here, n_e, T_e, and Z_{Be} are kept fixed to the values reported in Ref. [60] and only the argon fraction and argon ionization state are varied. The χ^2 analysis reveals that the elastic scattering strength is not sensitive to argon ionization until the argon ionizes into to the L-shell, i.e. for $Z_{Ar} \geq 8$. The Compton energy (244 eV) is large enough such that all M-shell electrons scatter inelastically into the bound-free contribution. Only for smaller scattering angles of $\theta \leq 55°$ ($k \leq 4$ Å^{-1}), would we expect M-shell electrons to participate in the elastic scattering. Figure 6.5 also demonstrates that 0.75 ± 0.2 at.% of argon reproduces the measured elastic scattering signal strength if we assume argon does not ionize into the L-shell. This finding is consistent throughout the conditions probed (and also for different times - not shown) and agrees with our knowledge

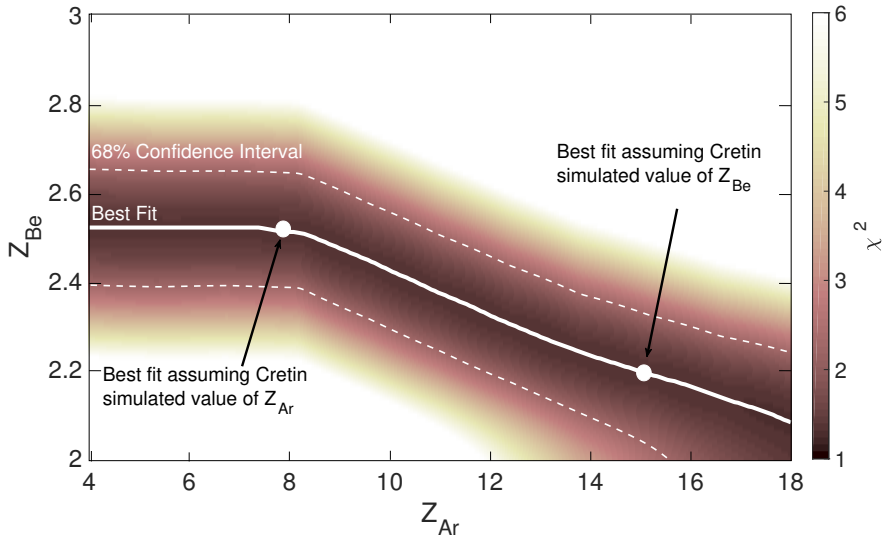

Figure 6.6: (Color online) χ^2 analysis of the elastic scattering strength in the spectrum at 5.7 ns, varying beryllium ionization and argon ionization. Best fits at each Ar ionization state are shown as the bold white line, with 1σ contours indicated by the dashed white lines. All fits assume 0.75 at.% argon, $T_e = 41$ eV, and $n_e = 1.9 \times 10^{24}$ cm^{-3}. The best fit is found for $Z_{Be} = 2.5 \pm 0.2$ when the Ar ionization is constrained to $Z_{Ar} \leq 8$. The white dots represent the positions of Cretin simulations for Z_{Be} and the required Z_{Ar} to match, and vice versa. $Z_{Ar} \geq 9.5$ is unphysical, for details see text.

about the capsules; the producer of the capsules, General Atomics, now regularly measures an argon impurity fraction of 0.5 to 2.0 at.% in the capsules they produce. At the time this experiment was performed, however, the regular reporting of argon impurities had not yet been implemented. We thus use our experimental finding and fix μ_{Ar} to 0.75 at.% for the following analysis and discussion of the XRTS spectrum at 5.7 ns.

The spectrum at 5.7 ns was taken very close to peak compression, when the sample was heated to $T = 41$ eV with a free electron density of $n_e = 1.9 \times 10^{24}$ cm^{-3}. Fig. 6.6 shows the χ^2 analysis of model spectra to the elastic feature of the spectrum at 5.7 ns that vary argon and beryllium ionization; the inelastic feature is again reproduced by using the previously inferred plasma parameters [60]. Similarly to Figure 6.5, the results show that the elastic scattering strength is sensitive to both beryllium and argon ionization if the argon ionizes into its L-shell, i.e. for $Z_{Ar} > 8$. The predictions for ionization balance vary more at these hotter and denser conditions than they do at the conditions at 3.1 ns.

Figure 6.7 shows Cretin simulations of both beryllium (a) and argon (b) ionization versus temperature with different models for ionization potential depression (IPD), assuming a constant electron density of 1.9×10^{24} cm^{-3} and $\mu_{Ar} = 0.75$ at.%. At the previously reported temperature of 41 eV, Cretin predicts that argon just begins to ionize into its L-shell, to an average charge state between $Z_{Ar} = 8.01$ and 8.15, depending on the model used for

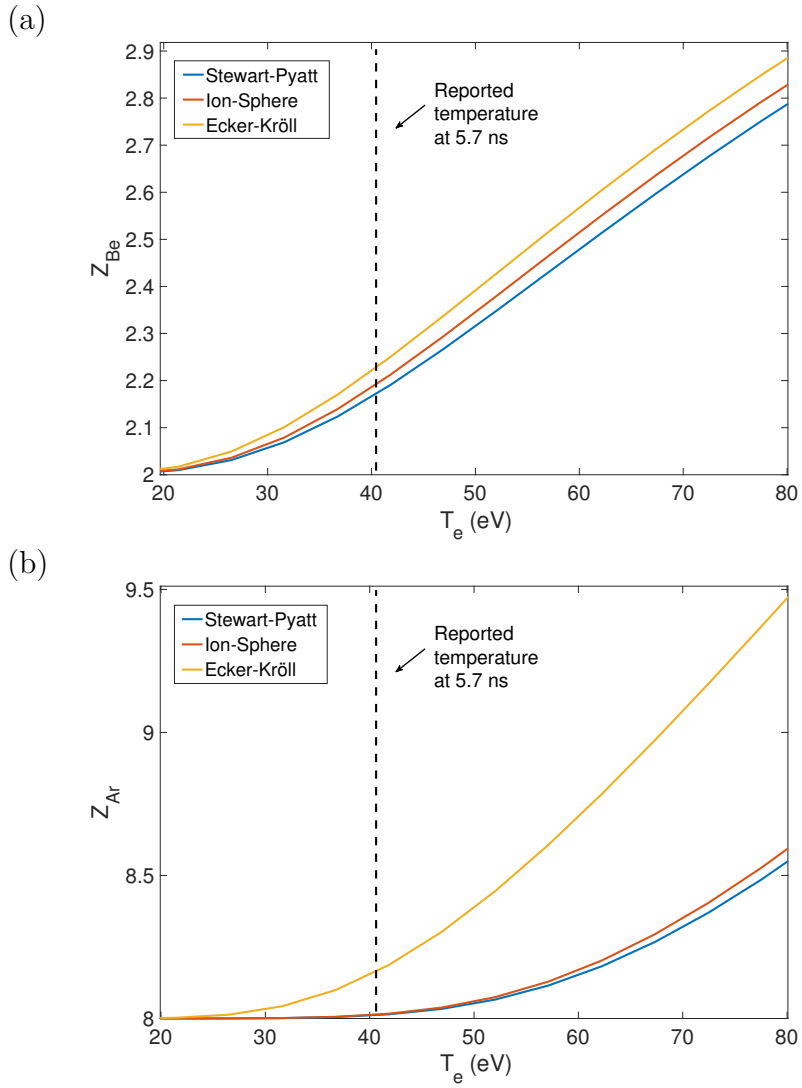

Figure 6.7: (Color online) Cretin simulations of Z_{Be} (a) and Z_{Ar} (b) vs. electron temperature for three different models of IPD, assuming a constant electron density of 1.9×10^{24} cm^{-3} and $\mu_{Ar} = 0.75$ at.%. The temperature of the spectrum at 5.7 ns, 41 eV, is noted by the vertical dashed line.

continuum lowering. If we constrain Z_{Ar} to these conditions, a beryllium ionization of $Z_{Be} = 2.5$ reproduces the elastic scattering strength, as indicated by the first white marker in Figure 6.6. This significant ionization into the K-shell of beryllium is higher than the Cretin predicted value of $Z_{Be} = 2.2$ (cf. Figure 6.6(a)). The original analysis of the inelastic feature also found $Z_{Be} = 2.5$ from fitting the red-shifted tail on the Compton peak caused by inelastic scattering from bound electrons [60].

The χ^2 plot in Figure 6.6 shows that the elastic scattering strength is much more sensitive

to beryllium K-shell ionization than to argon L-shell ionization. As discussed above, the elastic scattering does not change for Ar ionizations below $Z_{Ar} \leq 8$. Argon would have to ionize to $Z_{Ar} = 15$ if we fixed the beryllium ionization to the Cretin-predicted value of $Z_{Be} = 2.2$ (noted by the second marker in Figure 6.6). However, we consider values of $Z_{Ar} > 9.5$ to be unphysical; Figure 6.7 shows that the temperatures required to ionize argon beyond $Z_{Ar} = 9.5$ are over two times higher than the inferred temperature of 41 eV. This is true even for the most extreme IPD model considered: Ecker-Kröll. In order for the Cretin simulations to report a Be ionization of 2.5, the temperature would need to be increased by 50%, which is well beyond the experimental error. We thus conclude that we measure a higher Be charge state than is predicted by the widely used ionization models that we tested. However, more experiments are needed to discern a more precise temperature dependence of beryllium K-shell ionization.

6.5 Conclusions and Proposed Extensions

We have investigated the influence of argon impurities in samples of warm dense beryllium on the elastic scattering strength as measured by XRTS. We find that even small amounts of argon can have a significant effect on the elastic scattering strength in XRTS spectra. This influence arises from the larger number of bound electrons in argon as well as the tighter bounds of the electrons, which stretches the atomic form factor further out into k-space. It is therefore of high importance to characterize carefully targets with respect to mid- and high-Z impurities to interpret the elastic feature of XRTS spectra properly.

On the other hand, we have demonstrated that under suitable experimental geometries and plasma conditions the mid-Z impurity content can be inferred from the elastic scattering strength. The analysis of the elastic scattering contribution in the spectra taken by Kritcher et al. [60] allowed for a precise determination of the argon content as 0.75 ± 0.2 at.%, which is consistent with the capsule production process. Because of the large scattering angle used here, the elastic scattering only probes the K- and L-shell occupation of argon, and is therefore insensitive to the argon ionization states of $Z_{Ar} \leq 8$. For the plasma conditions present in this study we do not expect significant ionization into the L-shell. In principle, a combination of backward and forward scattering XRTS measurements could probe all atomic shells of argon and thus yield valuable data for its ionization in the warm dense environment created by the compressed beryllium.

Our analysis describes a potential method to study the ionization balance of mid- and high-Z elements at extreme conditions by doping a small well-characterized impurity fraction into a low-Z host material. Ideally, such experiments should first be conducted with pure beryllium capsules to determine the plasma parameters in the compressed sample. Then the experiment could be repeated with capsules containing a known mid- or high-Z impurity of interest and study its ionization balance under these conditions. A larger laser like, e.g., the National Ignition Facility (NIF) [57] could ionize the mid-Z element further into the L- or even the K-shell. Such experiments would avoid challenges arising from the high opacities

of such elements when being highly compressed in a pure state. Our results demonstrate that the elastic scattering strength in XRTS measurements of compressed, doped beryllium provides the opportunity to test theoretical models for the ionization balance in warm and hot dense matter.

Chapter 7

Using X-ray Thomson Scattering to Measure Temperature in Ion Stopping Power Experiments

In order to benchmark scattering simulations from complicated geometries and inhomogeneous conditions, it is important to measure spectra from homogeneous plasmas where some parameters are known *a priori*. One such example can be found in isochorically heated matter, where the mass density is known and only ionization and electron temperature are left to be fit from scattering spectra. This chapter outlines an experiment we performed in collaboration with the MIT Plasma and Fusion Center in which we used x-ray Thomson scattering to measure plasma conditions for material relevant ion stopping power experiments. These experiments also measured the temperatures of plasmas involved in stopping power experiments for the first time; previous efforts relied on simulations of the effects of radiative heating, in which there is much uncertainty.

7.1 Introduction to Ion Stopping Power

Understanding how charged particles deposit their energy into plasmas is paramount to achieving ignition through inertial confinement fusion (ICF) at facilities like the NIF [51, 57, 168]. In an ICF experiment, lasers compress a spherical shell of hydrogenic fuel. A central hot-spot forms as the capsule approaches peak compression, in which fusion reactions begin to occur and to generate α particles [35, 34]. The energetic α particles propagate outwards from the center into colder material, at which point they can redeposit their energy and cause more fusion reactions to occur; this concept is known as thermonuclear burn. In cold material, charged particles redeposit their energy through interactions with the bound electrons. Experimenters have studied energy loss in cold material in great detail [169]. However, the problem becomes more complicated in plasmas, in which charged particles lose energy due to Coulomb interactions with particles that are within a length-scale defined by

the plasma screening length [170]. Several experiments studied the stopping power in plasmas with densities of $n_e < 10^{22}$ g cm^{-3} and temperatures of $T_e < 60$ eV. The stopping power of warmer and denser material has also been extensively investigated through calculations and simulations [171]. However, there remains a dearth of experimental data to benchmark models for stopping power in high energy density plasmas.

In recent years, experimenters developed platforms for the OMEGA [56] laser that measure the energy lost by charged particles traveling through higher density plasmas [170, 172]. One OMEGA experiment measured the energy lost by 14 - 16 MeV protons traveling through radiatively heated solid-density material [170]. The experiment showed that stopping power could be measured to an accuracy that reduced uncertainties in modeling at these high densities. However, the experiment failed to measure the temperature of the radiatively heated material, and the interpretations of the stopping power data relied on simulations of the temperatures of radiatively heated material, in which there is much uncertainty. Indeed, a particular challenge of stopping power experiments is the accurate characterization of the plasma conditions, as electron temperature, density, and ionization all affect how charged particles redeposit their energy. Warm dense matter presents a particular challenge when modeling ion stopping power, as strong particle correlations and pressure ionization all affect the plasma conditions [170, 173].

The interpretation of XRTS spectra in the warm dense matter regime relies on accurate modeling of how x-rays scatter from plasmas. This includes modeling of atomic form factors, structure factors [103, 139], screening contributions [105], and the physics of the electrons that undero Raman-like transitions to the continuum [4]. However, not all scattering features scale linearly with plasma conditions, which means the resulting spectra may poorly reflect average conditions. There remains a dearth of experimental data from uniform conditions to validate the many models used in interpreting XRTS data. Indeed, recent XRTS work has come under criticism due to the inconsistent models used in conjunction for the inelastic and elastic scattering features to interpret plasma properties [107].

Thus, it is of interest to take XRTS spectra from materials at relatively uniform conditions, where some of the plasma properties are known *a priori*, in order to benchmark modeling of XRTS spectra. One such example of an experimental geometry that allows for probing of uniform conditions is a geometry that is also relevant to stopping power experiments: namely, a cylindrical plug of solid density material that is isochorically heated by x-rays from an x-ray converter foil backlighter that surrounds the radial portions of the cylinder. Stopping power experiments measure the energy lost by charged particles through the axis of the cylinder, which is also where the XRTS measurement can be made. Following the method of Reference [170], the sound speed of the solid density material can be estimated to be tens of μm/ns, whereas the radius of the cylinder is hundreds of μm/ns. By restricting the times of measurement to early after the laser drive turn-on, the material at the center of the cylinder can be assumed to be at solid density.

Initial XRTS measurements on sample-geometries relevant to stopping power experiments were made on the OMEGA laser in 2003 [99], in which experimenters determined the electron temperatures and ionization states of isochorically heated beryllium. Recent stopping

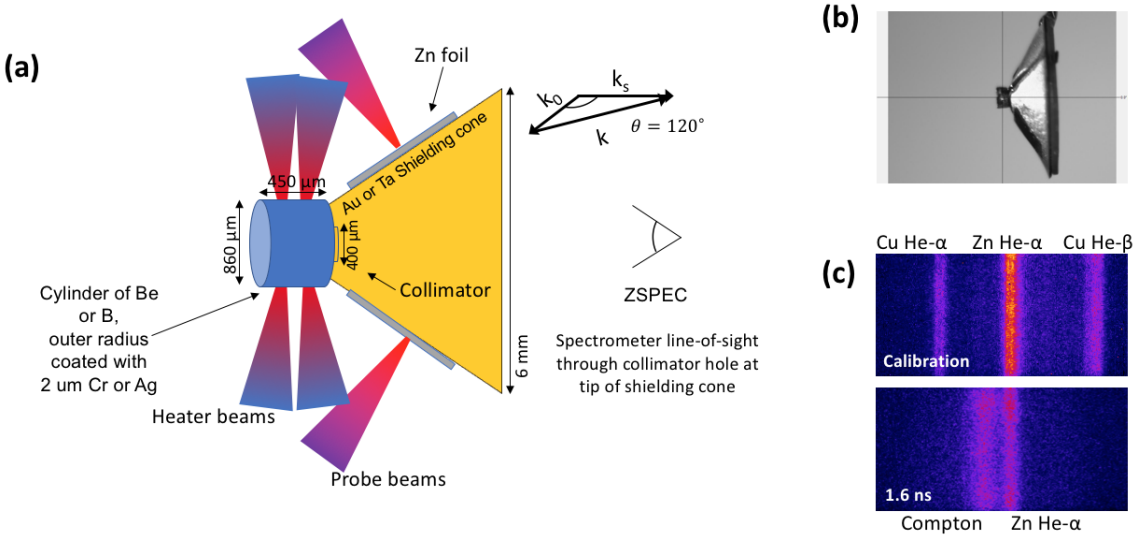

Figure 7.1: (a) A schematic of the target geometry, laser configurations, and scattering k-vectors. (b) A photograph of the B target. (c) The top image shows the spectrometer calibration spectrum from a brass foil, showing the Zn He-α doublet at 9 keV in the center of the strip, as well as Cu He-α and Cu K-α at 8.05 keV and Cu He-β at 9.87 keV. The bottom picture shows data from a B plug on the same scale as a the calibration shot.

power experiments on the OMEGA laser revived the need for accurate plasma characterization [170]. In the following sections, we present XRTS data taken from a new OMEGA platform on isochorically heated solid-density beryllium and boron, which was designed to work in series with stopping power measurements for the same materials. We analyze the results to obtain an electron temperature and beryllium and boron ionization states, and use to results to refine the modeling of XRTS spectra for future experiments on more complicated geometries.

7.2 Overview of Experimental Setup and Results

In this section, we present an overview of the experimental geometry used to collect data.

Figure 7.1(a) shows a schematic of the target geometry, along with the laser configurations and scattering k-vectors. The cylindrical sample is a 450 µm long cylinder with an 860 µm diameter. A 2 µm thick x-ray converter foil coats the outer radius of the cylinder. A high-Z material shielding cone with an opening angle of 120° abuts one end of the cylinder and serves to block the spectrometer's direct line-of-sight to the Zn backlighter foils that are glued to the sides of the cone. The cone contains a 400 µm diameter collimator hole at its tip to allow x-rays scattered by the sample through to the spectrometer, as seen in Figure 7.1. In the first experimental iteration, the shielding cone was made of 75 µm-thick Au, coated with

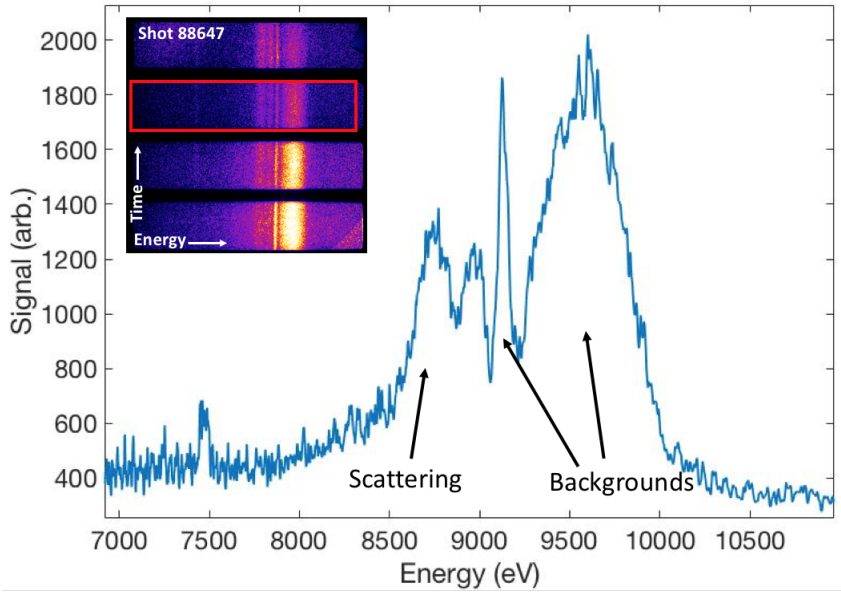

Figure 7.2: XRTS spectrum from Be cylinders with Au shielding cones. Line emission and thermal x-ray backgrounds appear at energies higher than the scattering signals.

10 μm of CH plastic in order to prevent the Au from becoming heated by hot electrons or direct laser irradiation. The second target design used a 3-D printed plastic cone, wrapped with 70 μm-thick Ta foils, which were also coated in CH plastic.

The sample consists either of solid density Be or solid density B. In both cases, the sample's density was characterized prior to the XRTS measurements. The Be was measured to be more than 99% pure, with a density of 1.858 g cm^{-3} on average; the measured density is slightly higher than the nominal Be solid density, as the outer layers of the Be are expected to oxidize. Oxygen exists at a concentration of less than 0.4 at.%, which will not affect interpretation of scattering data. Other trace metal impurities such as iron and magnesium are in concentrations well below 0.07 at.%. The B plugs were also measured to be more than 99% pure, with a mass density of 2.36 g cm^{-3}. There is again expected to be some oxidation of the outer layers and trace metal impurities which are not expected to affect scattering signals at such low concentrations.

14 beams heat the metal around the sample in a 1 ns square pulse. The heated metal radiates x-rays and isochorically heats the material in the inner cylinder. 6-10 beams heat the Zn foils, beginning at 1.2 ns, around the time the inner-cylinder is expected to reach its maximum temperature. The 9 keV Zn He-α x-rays that scatter from the sample are collected by the spectrometer, ZSPEC, as described in Chapter 4. The sample cylinder is aligned such that its axis aligns with the ZSPEC's line-of-sight.

We made the first measurements on solid density Be cylinders with Ag converter foils and an Au cone. Figure 7.2 shows an image of a spectrum from one strip along with an image of the raw data in the upper left hand corner. A high energy x-ray background signal appears

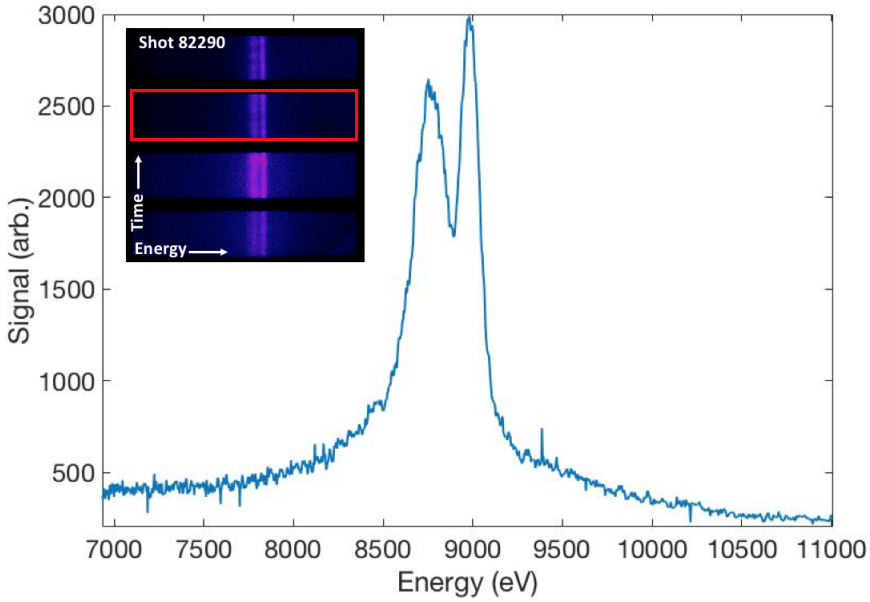

Figure 7.3: XRTS spectrum from B cylinders with Ta shielding cones. The Ta cones eliminated unwanted background signals.

above the elastic scattering, along with a Zn K-α line that appears shifted upward in energy. The Zn K-α line results from a small fraction of the Zn foil extending beyond the shielding cone, which fluoresced as a result of interaction from high energy x-rays. We attribute the broader, higher-energy background to Au L-shell emission from the shielding cone, but it remains unclear how the Au became heated. Current estimates suggest that the edge of the Au collimator in the shielding cone was heated by x-rays from the converter foil, which caused the Au to emit. The backgrounds present in the shot decreased the signal-to-noise ratio in the data and contributed more uncertainty to the final fitting.

In order to mitigate the x-ray background signals, we developed a new shielding cone that comprised a 3-D printed plastic cone surrounded by 70 μm thick Ta foils. We also ensured that no portion of the Zn foil was visible above the shielding cone. Figure 7.3 shows a spectrum taken from the Ta cone target, with the raw data in the upper left hand corner. In this case, the cylindrical sample was B with a Cr heating material layer. As seen in Figure 7.3 the new shielding cone design eliminated the higher energy background signals and improved the signal-to-noise ratio by a factor of 2. Thus, the highest quality data was achieved on B, and the Ta cone design will be used in the future.

The following sections outline the theory used to analyze the spectra, and perform a full analysis of the spectra.

7.3 Relevant XRTS Theory and Previous Work

As previously described, the use of inelastic scattering to determine electron properties such as temperature and density is well documented in the literature [99, 100, 60, 4]. Much recent work focuses on the information found in the elastic scattering feature; various authors use the strength of the elastic scattering feature to deduce plasma properties, such as the ion structure factor [103], the ionization state [4, 75, 104, 5, 30], or the screening properties [105]. The values of $f(k)$, $q(k)$, and $S_{ii}(k,\omega)$ all depend on the magnitude of the scattering vector, $k = \frac{2}{c}\omega_i \sin\theta/2$, which depends on the frequency of incident radiation, ω_i, and the scattering angle, θ. The ionic form factor, $f(k)$, provides the dominant contribution to elastic scattering, and is calculated by the Fourier transform of bound electrons around an ion species. The contribution from the electron screening cloud arises from the response of the free electrons to the ions, and is found to be best modeled by a finite wavelength screening method [5, 105]. The $S_{ii}(k)$ can be modeled with several different potentials, including Debye-Hückel, Coulomb, and finite wavelength. However, the Debye-Hückel potential is known to provide the best approximation in the case or partially ionized, moderate density and low-Z plasmas [98].

Because $f(k)$, $q(k)$, and S_{ii} all contribute to elastic scattering signal strength, inferring properties like ionization from elastic scattering relies on accurate modeling of these features. It is possible to take measurements at high k-values in which $q(k)$ and S_{ii} approach their limiting values of 0 and 1, respectively. In that case, the values of S_{ii} and q become insensitive to model choice, which increases certainty in the findings. It also means that the elastic scattering depends only on $f(k)$, and provides a reliable measurement of the ionization state.

Figure 7.4 shows both q and S_{ii} as calculated by different models for the screening cloud and the static structure factor for solid-density beryllium at 10 eV. It is worth noting that the results here are effectively temperature independent within the warm dense matter regime. The dashed vertical line marks the k-value of the experiment, 7.6 Å^{-1}. Figure 7.4 shows that the values of S_{ii} and q are model independent given the experimental geometry and energy of the probe source. By taking a measurement at a high k-value, we provide benchmarking measurements of ionization through the use of elastically scattered x-rays with high confidence.

7.4 Analysis of Spectra

We fit two XRTS spectra, one taken from beryllium and one from boron, by comparing the data with theoretically generated fits with a χ^2 fitting method. These spectra are unique compared to many previous XRTS measurement, as x-rays that reach the spectrometer scatter from an area of the sample with homogeneous plasma conditions and a known mass density. Only the electron temperature and the ionization states (and thus the electron density) remain to be fixed by the scattering spectra.

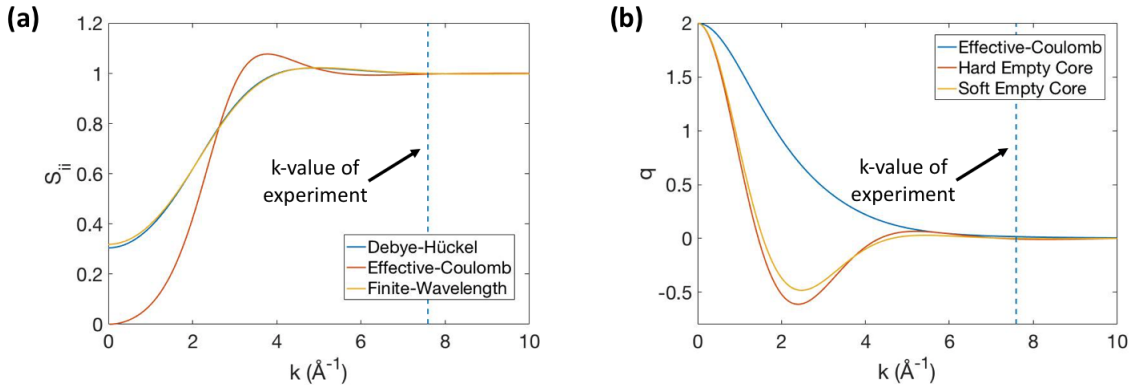

Figure 7.4: a) A plot of the ion structure factor as calculated by several different models available in the MCSS code [98, 138]: Debye-Hückel [174], Effective-Coulomb, and finite-wavelength [105]. b) A plot of the screening cloud contribution versus k as calculated by several different models available in the MCSS code [98, 138]: Effective-Coulomb, the Hard Empty Core, and the Soft Empty Core. In both cases, the k-value of the experiment (7.6 Å^{-1}) is noted by the dashed vertical line. The ion structure factor converges to 1 and the screening cloud converges to 0 at at the k-value probed for all possible models, increasing confidence in the ionization measurement.

The right side of Figure 7.5 shows the spectrum (smoothed by the resolution of the instrument), along with several theoretically-generated spectra that vary both electron temperature (top left) and beryllium ionization (bottom left). The best fits occurred with $T_e = 6 \pm 3$ eV and $Z_{Be} = 2.1 \pm 0.1$, and are also shown in Figure 7.5. All fits assumed a constant mass density of 1.86 g cm^{-3}, which was the measured mass-density of the beryllium sample. The left side of Figure 7.5 shows the chi-squared fitting of the spectrum, with 1σ confidence intervals denoted by the dashed white lines. No ionization states below $Z_{Be} = 2$ were considered, as the beryllium L-shell is low enough in energy such that no L-shell electrons could remain in bound states at solid mass density.

Figure 7.6 shows the best fit to the scattering spectrum of boron, along with a χ^2 plot that varies ionization and electron temperature. For the case of boron, the best fits were found to be $T_e = 10 \pm 2.5$ eV and $Z_B = 3.05 \pm 0.05$. The improved shielding cone reduced the experimental error from 50% to only 25% due to the improved signal-to-noise ratio and lack of x-ray background. The resulting fits of temperature and ionization show the effectiveness of this platform to measure plasma parameters in geometries relevant to stopping power experiments.

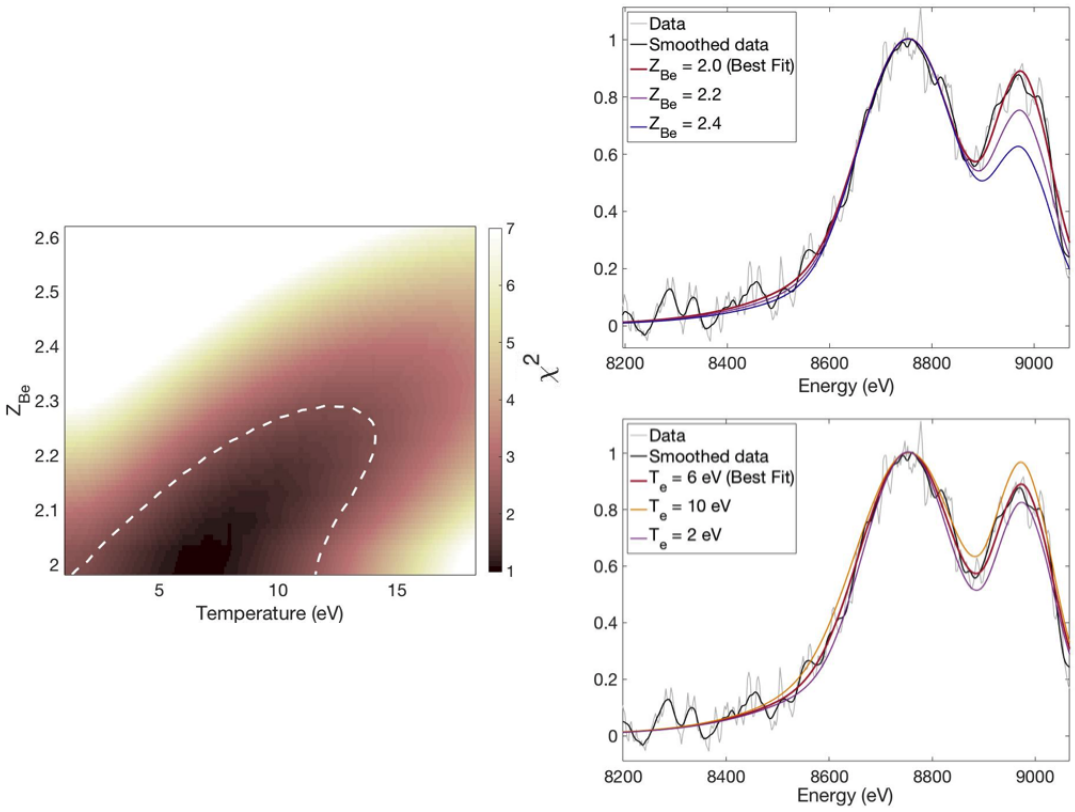

Figure 7.5: Left: A measured XRTS spectrum at 120° from pure beryllium at homogeneous conditions, showing the best fits for electron temperature and beryllium ionization state at 6 ± 3 eV and 2.1 ± 0.1. Other displayed fits vary electron temperature and ionization state to show the sensitivity to these parameters at the experimental conditions. Right: χ-squared fitting to the beryllium spectrum, altering electron temperature and ionization state. The 1σ confidence levels are marked by the dashed lines.

7.5 Conclusion and Proposed Extensions

In this chapter, we presented two measurements from a new XRTS platform designed to work in conjunction with stopping power experiments on the OMEGA laser. The measurements came from isochorically heated and Be and B at solid mass density, allowing us to deduce electron temperature and ionization from spectral fits. We found the temperature of the beryllium to be $T_e = 6 \pm 3$ eV and the ionization state to be $Z_{Be} = 2.1 \pm 0.1$, and the best fits for boron to be $T_e = 10 \pm 2.5$ eV and $Z_B = 3.05 \pm 0.5$. Future experiments could further improve the error bars on the returned plasma parameters by increasing the signal-to-noise ratio of the measurement, presumably by adding more lasers to heat the x-ray backlighter, or by summing repeated measurements. In addition, spectral sensitivity to temperature could be increased if the material were heated to higher temperatures, as

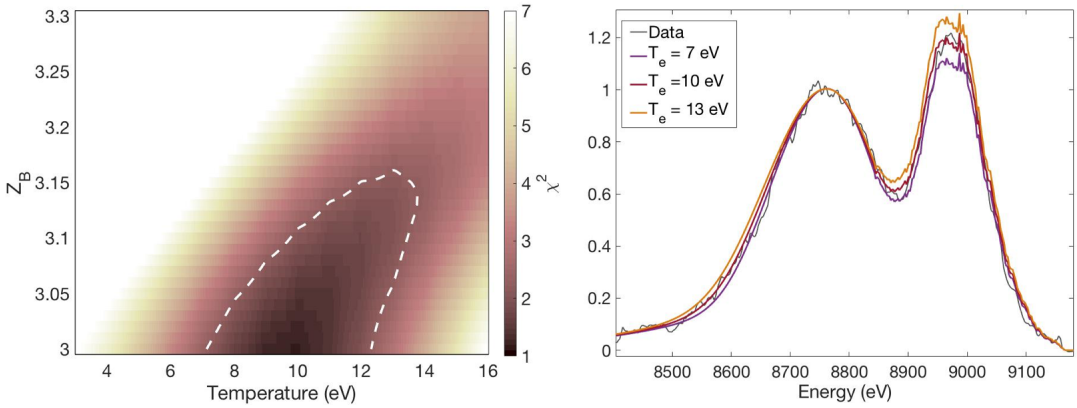

Figure 7.6: Left: a χ^2 plot of an XRTS spectrum from boron that varies electron temperature and boron ionization state. 1σ confidence intervals are marked by the white dashed lines. The best fit is found to be at 10.0 ± 2.5 eV with $Z_B = 3.05 \pm 0.05$. Right: an example of temperature sensitivity to fitting. The data is plotted with three different curves of different electron temperatures.

the electron velocity distribution, and thus the free-free scattering feature, becomes more sensitive to temperature and less to density as the plasma becomes less degenerate.

In principle, this platform offers the opportunity to make more XRTS measurements from uniform conditions on many different samples. The starting density of the sample could be systematically varied to probe a full area of phase space and to identify the effects of density both on ionization and on radiative heating rates. As it stands, this platform has been demonstrated to measure the temperature and ionization state of a sample used in stopping power experiments. These measurements allow refinement of models used in the stopping power community by providing a reliable way to measure the conditions in a sample.

Chapter 8

Conclusions and Future Directions

In this thesis, I presented the motivation behind studying high energy density physics and discussed the various applications of HEDP, including inertial confinement fusion, stockpile stewardship, and laboratory astrophysics. I also outlined the physics fundamentals of the diagnostics used to measure plasma parameters in shock physics experiments. X-rays penetrate deeply into dense low-Z material, which makes them ideal tools to measure plasma conditions in warm dense matter. X-ray Thomson scattering measures the electron distribution of a plasma, making it particularly well suited to measuring parameters relevant to the EOS. I discussed several experiments that used XRTS as a primary diagnostic. One experiment measured scattering spectra from imploding diamond spheres and found that the ionization state was higher than predicted by many commonly-applied ionization models. Another experiment analyzed the contributions to elastic scattering from an argon impurity in imploding beryllium shells; the experiment found that even a small percentage of argon has a significant effect on elastic scattering and quantified the effect and returned the beryllium ionization state. The final experiment used XRTS to measure the plasma temperature and ionization state of isochorically heated material used in stopping power experiments. All these studies showed the power of XRTS to measure equation of state variables in HEDP experiments.

I propose several extensions to the Gbar platform on OMEGA. Solid spheres reach unprecedented pressures and offer the ability to probe multiple points along the Hugoniot, which warrants their use despite the complications that arise in data analysis. I propose repeating the experiment with two goals in mind. The first would repeat the measurement on solid diamond spheres, but with 500 μm diameter targets. The smaller targets would reach more extreme conditions in the shocked material, and allow for exploration of the onset of K-shell ionization in carbon. The second proposed extension to the Gbar work would repeat the experiment with 1 mm and 500 μm spheres, but would include a layer of mid- or high-Z dopant at a given radius; the position of the radius would vary between 5 to 400 μm. X-ray radiography measurements would confirm the implosion time at which the shock passes over the radius of the dopant and assess the symmetry of the implosion. An x-ray fluorescence measurement could be taken at the time the shock front passed over

the doped region. The fluorescence measurement would arise from the extreme conditions of the shock front and allow for spatially-resolved temperature measurements. In the case that a non-spherically symmetric shock front causes inhomogeneities in the experiment, the dopant could be localized to a single point. The challenge in this experiment arises from target fabrication issues; doping a single layer or a single point in a solid sphere still requires development work. This proposed experiment would combine the knowledge from the solid diamond sphere scattering experiments and from the doped beryllium shell elastic scattering analysis to return more localized temperature measurements from imploding spheres.

We also propose to extend the work done on the effects of mid-Z impurities on elastic scattering from low-Z materials. The experiment described in Chapter 6 could be repeated with Be capsules for different mid- and high-Z dopants to measure inner-shell ionization of the dopants. In order to bring the materials to more extreme conditions such that inner-shell ionization occurs, smaller capsules ($\sim$ 500 μm diameter) or a larger laser (the NIF) could be used.

We can also use the XRTS stopping power platform to optimize future stopping power experiments. XRTS can measure the time-dependent temperatures of radiatively heated materials in order to characterize the optimal heater foil material and thickness. Another extension to this work involves exploiting the stopping power XRTS platform to measure the onset of pressure ionization in warm dense matter. In principle, the cylinders could be made with materials at different starting densities. Then, the different ion densities would be known *a priori* and XRTS could be used to measure the temperatures and the ionization states. This would allow for a full exploration of the onset of pressure ionization as a function of ion density. Such a measurement would help constrain the models that predict the strength of IPD. However, as discussed previously, there is a trade-off between understanding the effects of density and temperature on scattering spectra, so this extension is not as trivial as it may seem.

Overall, XRTS offers the unique ability to measure the conditions of plasmas in the warm dense matter state. A single XRTS spectrum can constrain mass density, electron density, ionization state, and electron temperature, which is capable of fully benchmarking equation of state models. Because of this, XRTS is a technique worth further development in the HEDP community. Of course, there are still limitations to XRTS as a diagnostic. For one, the small scattering cross section means that target development with regards to appropriate shielding is often difficult and can span several shot days. Secondly, XRTS is still a relatively new technique; there is an active discussion in the community as to the best methods to extract plasma parameters from scattering spectra. Hopefully, as more data is collected, the community will coalesce and agree upon interpretation of scattering spectra to push forward the use of x-ray scattering as a plasma diagnostic. For the present, experimenters continue to collect high-quality and precise XRTS measurements in order to obtain data capable of benchmaking ionization and EOS models in warm dense matter.

Bibliography

[1] National Research Council. *Frontiers in High Energy Density Physics: The X-Games of Contemporary Science*. The National Academies Press, 2003.

[2] R. P. Drake. *High-Energy-Density Physics: Fundamentals, Intertial Fustion, and Experimental Astrophysics*. Springer, 2006.

[3] P A Sterne et al. "Equations of State for Ablator Materials in Inertial Confinement Fusion Simulations". In: *Journal of Physics: Conference Series* 717 (2016), p. 012082.

[4] L. B. Fletcher et al. "Observations of Continuum Depression in Warm Dense Matter with X-Ray Thomson Scattering". In: *Phys. Rev. Lett.* 112 (2014), p. 145004.

[5] L. B. Fletcher et al. "Ultrabright X-ray laser scattering for dynamic warm dense matter physics". In: *Nat. Photonics* 9 (Apr. 2015), pp. 274–279.

[6] S. H. Glenzer et al. "Observations of Plasmons in Warm Dense Matter". In: *Phys. Rev. Lett.* 98 (2007), p. 065002.

[7] C. A. Iglesias. "Comment on "Free–free opacity in warm aluminum"". In: *High Ener. Dens. Phys.* 7 (2011), pp. 38–39.

[8] D. Kraus et al. "The complex ion structure of warm dense carbon measured by spectrally resolved x- ray scattering". In: *Phys. of Plasmas* 21 (2015), p. 056309.

[9] B. B. L. Witte et al. "Warm Dense Matter Demonstrating Non-Drude Conductivity from Observations of Nonlinear Plasmon Damping". In: *Phys. Rev. Lett.* 118 (2017), p. 225001.

[10] Shuai Zhang et al. "First-principles equation of state and shock compression predictions of warm dense hydrocarbons". In: *Phys. Rev. E* 96 (2017), p. 013204.

[11] R. W. Lee et al. "Plasma-based studies with intense X-ray and particle beam sources Plasma-based studies with intense X-ray and particle beam sources Plasma-based studies with intense X-ray and particle beam sources". In: *Laser and Part. Beams* 20 (2002), pp. 527–536.

[12] J. Colvin and J. Larsen. *Extreme Physics: Properties and Behavior of Matter at Extreme Conditions*. Cambridge University Press, 2014.

[13] F. F. Chen. *Introduction to Plasma Physics and Controlled Fusion*. Third. Springer, 2016.

[14] S. H. Glenzer et al. "X-ray scattering from solid density plasmas". In: *Phys. Plasmas* 10 (2003), p. 2433.

[15] Tristan Guillot. "Interiors of Giant Planets Inside and Outside the Solar System". In: *Science* 286 (1999), pp. 72–77. ISSN: 0036-8075.

[16] B. Militzer et al. "A Massive Core in Jupiter Predicted from First-Principles Simulations". In: *The Astrophysical Journal Letters* 688 (2008), p. L45.

[17] N. Nettelmann et al. "Uranus evolution models with simple thermal boundary layers". In: *Icarus* 275 (2016), pp. 107–116.

[18] Robert Püstow et al. "H/He demixing and the cooling behavior of Saturn". In: *Icarus* 267 (2016), pp. 323–333.

[19] W. B. Hubbard et al. "Liquid metallic hydrogen and the structure of brown dwarfs and giant planets". In: *Physics of Plasmas* 4 (1997), pp. 2011–2015.

[20] A. Burrows et al. "A Nongray Theory of Extrasolar Giant Planets and Brown Dwarfs". In: *The Astrophysical Journal* 491.2 (1997), p. 856.

[21] G. Chabrier et al. "The molecular-metallic transition of hydrogen and the structure of jupiter and saturn". In: *Astrophys. J.* 391 (1992), pp. 817–826.

[22] R. SMOLUCHOWSKI. "Internal Structure and Energy Emission of Jupiter". In: *Nature* 215 (1967), p. 691.

[23] D. Saumon and S. B. Jacobson. "Pure Hydrogen Model Atmospheres for Very Cool White Dwarfs". In: *The Astrophysical Journal Letters* 511 (1999), p. L107.

[24] S. Chandrasekhar. "The maximum mass of ideal white dwarfs". In: *Astrophys. J.* 74 (1931), pp. 81–82.

[25] G. Chabrier. "Quantum effects in dense Coulombic matter: application to the cooling of white dwarfs". In: *Astrophys. J.* 414 (1993), pp. 695–700.

[26] N. K. Glendenning, Ch. Kettner, and F. Weber. "Possible New Class of Dense White Dwarfs". In: *Phys. Rev. Lett.* 74 (1995), pp. 3519–3522.

[27] M. S. Murillo. "Strongly coupled plasma physics and high energy-density matter". In: *Physics of Plasmas* 11 (2004), pp. 2964–2971.

[28] Marvin Ross. "The ice layer in Uranus and Neptune—diamonds in the sky?" In: *Nature* 292 (1981), p. 435.

[29] L. R. Benedetti et al. "Dissociation of CH4 at High Pressures and Temperatures: Diamond Formation in Giant Planet Interiors? REPORT Dissociation of CH4 at High Pressures and Temperatures: Diamond Formation in Giant Planet Interiors?" In: *Science* 286 (1999), pp. 100–102.

[30] D. Kraus et al. "Probing the Complex Ion Structure in Liquid Carbon at 100 GPa". In: *Phys. Rev. Lett.* 111 (2013), p. 255501.

[31] *Basic research needs for high energy density laboratory physics*. U.S. Department of Energy, Office of Science and National Nuclear Security Administration. Nov. 2009.

[32] J. D. Lawson. *Some Criteria for a power producing thermonuclear reactor*. Tech. rep. U.K.A.E.R.E. GP/R 1807. Atomic Energy Research Establishment, Harwell Bershire, Dec. 1955.

[33] R. E. Tipton. *Generalized Lawson Critera for Inertial Confinement Fusion*. Tech. rep. LLNL-TR-676592. Lawrence Livermore National Laboratory, Aug. 2016.

[34] Mordecai D. Rosen. "The physics issues that determine inertial confinement fusion target gain and driver requirements: A tutorial". In: *Physics of Plasmas* 6 (1999), pp. 1690–1699.

[35] John D. Lindl et al. "The physics basis for ignition using indirect-drive targets on the National Ignition Facility". In: *Physics of Plasmas* 11 (2004), pp. 339–491.

[36] John Sheffield. "The physics of magnetic fusion reactors". In: *Rev. Mod. Phys.* 66 (1994), pp. 1015–1103.

[37] Charles C. Baker, Gustav A. Carlson, and Robert A. Krakowski. "Trends and Developments in Magnetic Confinement Fusion Reactor Concepts". In: *Nuclear Technology - Fusion* 1 (1981), pp. 5–78.

[38] R. Betti and O. A. Hurricane. "Inertial-confinement fusion with lasers". In: *Nat. Phys.* 12 (2016), pp. 435–448.

[39] J. T. Larson. "Why crogenic intertial confinement fusion targets?" In: *J. Vac. Sci. Technol. A* 7 (1989), p. 1150.

[40] D. E. T. F. Ashby. "Laser-induced compression of thin shells and uniform spheres: a theoretical comparison". In: *Nucl. Fusion* 16 (1976), p. 231.

[41] S. Atenzi and J. Meyer-ter-Vehn. *The Physics of Inertial Fusion*. Oxford Science Publications, 2004.

[42] T.C. Sangster et al. "Overview of inertial fusion research in the United States". In: *Nuclear Fusion* 47 (2007), S686.

[43] J. S. Ross et al. "Lead (Pb) Hohlraum: Target for Inertial Fusion Energy". In: *Sci. Reports* 3 (2013), p. 1453.

[44] E. L. Dewald et al. "X-ray conversion efficiency of high-Z hohlraum wall materials for indirect drive ignition". In: *Physics of Plasmas* 15 (2008), p. 072706.

[45] D. T. Casey et al. "Improved Performance of High Areal Density Indirect Drive Implosions at the National Ignition Facility using a Four-Shock Adiabat Shaped Drive". In: *Phys. Rev. Lett.* 115 (2015), p. 055001.

[46] R. S. Craxton et al. "Direct-drive inertial confinement fusion: A review". In: *Physics of Plasmas* 22 (2015), p. 110501.

[47] D. J. Hoarty et al. "Fluorescence spectroscopy as a diagnostic of the radiation environment in high energy density experiments (invited)". In: *Review of Scientific Instruments* 75 (2004), pp. 3655–3659.

[48] D. E. Hinkel et al. "Progress toward ignition at the National Ignition Facility". In: *Plasma Physics and Controlled Fusion* 55 (2013), p. 124015.

[49] J.D. Lindl et al. "Progress towards ignition on the National Ignition Facility". In: *Nuclear Fusion* 51 (2011), p. 094024.

[50] N. B. Meezan et al. "Indirect drive ignition at the National Ignition Facility". In: *Plasma Physics and Controlled Fusion* 59 (2017), p. 014021.

[51] O. A. Hurricane et al. "Fuel gain exceeding unity in an inertially confined fusion implosion". In: *Nature* 506 (2014), p. 343.

[52] R. Betti et al. "Alpha Heating and Burning Plasmas in Inertial Confinement Fusion". In: *Phys. Rev. Lett.* 114 (2015), p. 255003.

[53] M. M. Marinak et al. "A comparison of three-dimensional multimode hydrodynamic instability growth on various National Ignition Facility capsule designs with HYDRA simulations". In: *Physics of Plasmas* 5 (1998), pp. 1125–1132.

[54] J. S. Ross et al. "High-density carbon capsule experiments on the national ignition facility". In: *Phys. Rev. E* 91 (2015), p. 021101.

[55] A. J. MacKinnon et al. "High-density carbon ablator experiments on the National Ignition Facility". In: *Physics of Plasmas* 21 (2014), p. 056318.

[56] T.R Boehly et al. "Inertial confinement fusion experiments with OMEGA-A 30-kJ, 60-beam UV laser". In: *Fusion Engineering and Design* 44 (1999), pp. 35–42.

[57] E. I. Moses et al. "The National Ignition Facility: Ushering in a new age for high energy density science". In: *Physics of Plasmas* 16 (2009), p. 041006.

[58] M. C. Jones et al. "X-ray power and yield measurements at the refurbished Z machine". In: *Review of Scientific Instruments* 85 (2014), p. 083501.

[59] M. Keith Matzen et al. "Pulsed-power-driven high energy density physics and inertial confinement fusion research". In: *Physics of Plasmas* 12 (2005), p. 055503.

[60] A. Kritcher et al. "In-Flight Measurements of Capsule Shell Adiabats in Laser-Driven Implosions". In: *Phys. Rev. Lett.* 107 (2011), p. 015002.

[61] A.M. Saunders et al. "Influence of argon impurities on the elastic scattering of x-rays from imploding beryllium capsules". In: *High Energy Density Physics* 26 (2018), pp. 86–92.

[62] S. H. Glenzer and R. Redmer. "X-ray Thomson scattering in high energy density plasmas". In: *Rev. Mod. Phys.* 81 (2009), p. 1625.

[63] F.Douglas Swesty. "Thermodynamically Consistent Interpolation for Equation of State Tables". In: *Journal of Computational Physics* 127 (1996), pp. 118–127.

[64] Kathleen S. Trainor. "Construction of a wide-range tabular equation of state for copper". In: *Journal of Applied Physics* 54 (1983), pp. 2372–2379.

[65] R. M. More et al. "A new quotidian equation of state (QEOS) for hot dense matter". In: *The Physics of Fluids* 31 (1988), pp. 3059–3078.

[66] James M. Lattimer and F. Douglas Swesty. "A generalized equation of state for hot, dense matter". In: *Nuclear Physics A* 535 (1991), pp. 331–376.

[67] R. Cauble et al. "Absolute Equation-of-State Data in the 10-40 Mbar (1-4 TPa) Regime". In: *Phys. Rev. Lett.* 80 (1998).

[68] S. Atzeni, A. Caruso, and V. A. Pais. "Model equation-of-state for any material in conditions relevant to ICF and to stellar interiors". In: *Laser and Particle Beams* 4 (1986), pp. 393–402.

[69] M. A. Barrios et al. "High-precision measurements of the equation of state of hydrocarbons at 1–10 Mbar using laser-driven shock waves". In: *Physics of Plasmas* 17 (2010), p. 056307.

[70] M. A. Barrios et al. "Precision equation-of-state measurements on National Ignition Facility ablator materials from 1 to 12 Mbar using laser-driven shock waves". In: *Journal of Applied Physics* 111 (2012), p. 093515.

[71] L. B. Da Silva et al. "Absolute Equation of State Measurements on Shocked Liquid Deuterium up to 200 GPa (2 Mbar)". In: *Phys. Rev. Lett.* 78 (1997), pp. 483–486.

[72] G. W. Collins et al. "Measurements of the Equation of State of Deuterium at the Fluid Insulator-Metal Transition". In: *Science* 281 (1998), pp. 1178–1181.

[73] K. Falk et al. "Equation of State Measurements of Warm Dense Carbon Using Laser-Driven Shock and Release Technique". In: *Phys. Rev. Lett.* 112 (2014), p. 155003.

[74] D. E. Fratanduono et al. "Equation of state, adiabatic sound speed, and Grüneisen coefficient of boron carbide along the principal Hugoniot to 700 GPa". In: *Phys. Rev. B* (2016), p. 184107.

[75] D. Kraus et al. "X-ray scattering measurements on imploding CH spheres at the National Ignition Facility". In: *Phys. Rev. E* 94 (2016), p. 011202.

[76] C. A. Iglesias and P. A. Sterne. "Fluctuations and the ionization potential in dense plasmas". In: *High Energy Density Physics* 9 (2013), pp. 103–107.

[77] O. Circosta et al. "Measurements of continuum lowering in solid-density plasmas created from elements and compounds Measurements of continuum lowering in solid-density plasmas created from elements and compounds". In: *Nat. Commun.* 7 (2016), p. 11713.

[78] S. M. Vinko et al. "Investigation of femtosecond collisional ionization rates in a solid-density aluminium plasma". In: *Nat. Commun.* 6 (2015), p. 6397.

[79] O. Ciricosta et al. "Direct Measurements of the Ionization Potential Depression in a Dense Plasma". In: *Phys. Rev. Lett.* 109 (2012), p. 065002.

[80] C. A. Iglesias. "A plea for a reexamination of ionization potential depression measurements". In: *High Ener. Dens. Phys.* 12 (2014), pp. 5–11.

[81] Megh Nad Saha D.Sc. "LIII. Ionization in the solar chromosphere". In: *The London, Edinburgh, and Dublin Philosophical Magazine and Journal of Science* 40 (1920), pp. 472–488.

[82] D. Umstadter. "Viewpoint: Extreme X-Rays Probe Extreme Matter". In: *Physics* 5 (2012), p. 88.

[83] J. C. Stewart and K. D. Pyatt. "Lowering of Ionization Potentials in Plasmas". In: *Astrophys. J.* 144 (1966), p. 1203.

[84] R. P. Feynman, N. Metropolis, and E. Teller. "Equations of State of Elements Based on the Generalized Fermi-Thomas Theory". In: *Phys. Rev.* 75 (1949), pp. 1561–1573.

[85] H. Mayer. *Methods of opacity calculations*. Tech. rep. LA-647. Los Alamos National Laboratory, 1948.

[86] W. A. Lokke and W. H. Grasberger. *XSNQ-U: a non LTE emission and absorption coefficient subroutine*. Tech. rep. 77-017045. Lawrence Livermore National Laboratory, 1977.

[87] N. K. Gupta and B. K. Godwal. "Effects of non-local thermodynamic equilibrium conditions on numerical simulations of inertial confinement fusion plasmas". In: *Pramana* 59 (2002), p. 33.

[88] S. H. Glenzer et al. "Demonstration of Ignition Radiation Temperatures in Indirect-Drive Inertial Confinement Fusion Hohlraums". In: *Phys. Rev. Lett.* 106 (2011), p. 085004.

[89] A. P. French. *Newtonian Mechanics*. Norton, 1971.

[90] D. Clark. *Approaches to ICF: Overview and Parameter Space - Part 1*. ICF Program Lecture Series. Feb. 2017.

[91] Ya. B. Zel'dovich and Yu. P. Raizer. *Physics of Shock Waves and High-Temperature Hydrodynamic Phenomena*. Ed. by Wallace D. Hayes and Ronald F. Probstein. Dover, 2002.

[92] P.A. Sterne et al. "Equation of state, occupation probabilities and conductivities in the average atom Purgatorio code". In: *High Energy Density Physics* 3 (2007), pp. 278–282.

[93] George B. Rybicki and Alan P. Lightman. *Radiative Processes in Astrophysics*. Wiley-VCH, 2004.

[94] *Soft X-rays and Extreme Ultraviolet Radiation*. Cambridge University Press, 2007.

[95] D. H. Froula et al. *Plasma Scattering of Electromagnetic Radiation*. 2nd. Academic Press, 2011.

[96] J. Chihara. "Difference in x-ray scattering between metallic and non-metallic liquids due to conduction electrons". In: *J. Phys. F: Met. Phys.* 17 (1987), pp. 295–304.

[97] G. Gregori et al. "Theoretical model of x-ray scattering as a dense matter probe". In: *Phys. Rev. E.* 67 (2003), p. 026412.

[98] D. A. Chapman. *User guide and theoretical basis for the Multi-Component Scattering Spectra (MCSS) Thomson scattering analysis code (O)*. AWE. Mar. 2017.

[99] S. H. Glenzer et al. "Demonstration of Spectrally Resolved X-Ray Scattering in Dense Plasmas". In: *Phys. Rev. Lett.* 90 (2003), p. 175002.

[100] H. J. Lee et al. "X-Ray Thomson-Scattering Measurements of Density and Temperature in Shock-Compressed Beryllium". In: *Phys. Rev. Lett.* 102 (2009), p. 115001.

[101] G. Gregori et al. "X-Ray Scattering Measurements of Radiative Heating and Cooling Dynamics". In: *Phys. Rev. Lett.* 101 (2008), p. 045003.

[102] P. Neumayer et al. "Plasmons in Strongly Coupled Shock-Compressed Matter". In: *Phys. Rev. Lett.* 105 (2010), p. 075003.

[103] T. Ma et al. "Observations of strong ion-ion correlations in dense plasmas". In: *Phys. of Plasmas* 21 (2014), p. 056302.

[104] D. Riley et al. "X-Ray Diffraction from a Dense Plasma". In: *Phys. Rev. Lett.* 84 (2000), pp. 1704–1707.

[105] D. A. Chapman et al. "Observation of finite-wavelength screening in high-energy-density matter". In: *Nat. Commun.* 6 (2015), p. 6839.

[106] E. García Saiz et al. "Evidence of Short-Range Screening in Shock-Compressed Aluminum Plasma". In: *Phys. Rev. Lett.* 101 (2008), p. 075003.

[107] A. N. Souza et al. "Predictions of x-ray scattering spectra for warm dense matter". In: *Phys. Rev. E* 89 (2014), p. 023108.

[108] C. E. Starrett and D. Saumon. "Models of the elastic x-ray scattering feature for warm dense aluminum". In: *Phys. Rev. E* 92 (2015), p. 033101.

[109] A. D. Baczewski et al. "X-ray Thomson Scattering in Warm Dense Matter without the Chihara Decomposition". In: *Phys. Rev. Lett.* 116 (2016), p. 115004.

[110] Anne P. Thorne. *Spectrophysics*. Chapman and Hall, 1988.

[111] G. Gregori et al. "Experimental Characterization of a Strongly Coupled Solid Density Plasma Generated in a Short-pulse Laser Target Interaction". In: *Contributions to Plasma Physics* 45 (2005), pp. 284–292.

[112] K. U. Akli et al. "Temperature sensitivity of Cu K-α imaging efficiency using a spherical Bragg reflecting crystal". In: *Physics of Plasmas* 14 (2007), p. 023102.

[113] W. Theobald et al. "Hot surface ionic line emission and cold K-inner shell emission from petawatt-laser-irradiated Cu foil targets". In: *Physics of Plasmas* 13 (2006), p. 043102.

[114] S. B. Hansen et al. "Changes in the electronic structure of highly compressed iron revealed by x-ray fluorescence lines and absorption edges". In: *High Energ. Dens. Phys.* 24 (2017), pp. 39–43.

[115] D. J. Hoarty et al. "Observations of the Effect of Ionization-Potential Depression in Hot Dense Plasma". In: *Phys. Rev. Lett.* 110 (2013), p. 265003.

[116] *Introduction to Quantum Mechanics*. Pearson Prentice Hall, 2005.

[117] H. A. Scott. "Cretin—a radiative transfer capability for laboratory plasmas". In: *J. Quant. Spectrosc. Radiat. Transfer* 71 (2001), pp. 689–701.

[118] H.-K. Chung et al. "FLYCHK: Generalized population kinetics and spectral model for rapid spectroscopic analysis for all elements". In: *High Energy Density Physics* 1 (2005), pp. 3–12. ISSN: 1574-1818.

[119] H. A. Scott and S. B. Hansen. "Advances in NLTE modeling for integrated simulations". In: *High Energ. Dens. Phys.* 6 (2010), pp. 39–47.

[120] H. A. Scott. "Cretin- a radiative transfer capability for laboratory plasmas". In: *Journal of Quantitative Spectroscopy & Radiative Transfer* 71 (2001), pp. 689–701.

[121] J. Nilsen et al. "Using neutrons to measure keV temperatures in highly compressed plastic at multi-Gbar pressures". In: *High Energy Density Physics* 21 (2016), pp. 20–26.

[122] H Brysk. "Fusion neutron energies and spectra". In: *Plasma Physics* 15.7 (1973), p. 611.

[123] Z. Chen et al. "Ion temperature measurements of indirect-drive implosions with the neutron time-of-flight detector on SG-III laser facility". In: *Review of Scientific Instruments* 89 (2018), p. 023504.

[124] A. L. Kritcher et al. "Shock Hugoniot measurements of CH at Gbar pressures at the NIF". In: *J. Phys.: Conf. Ser.* 688 (2016), p. 012055.

[125] A. L. Kritcher et al. "Probing matter at Gbar pressures at the NIF". In: *High Energ. Dens. Phys.* 10 (2014), pp. 27–34.

[126] T. Döppner et al. "X-Ray Thomson scattering as a temperature probe for Gbar shock experiments". In: *J. Phys.: Conf. Ser.* 500 (2014), p. 192019.

[127] T. Döppner et al. "Qualification of a high-efficiency, gated spectrometer for x-ray Thomson scattering on the National Ignition Facility". In: *Review of Scientific Instruments* 85 (2014), p. 11D617.

[128] T. Döppner et al. "Improving a high-efficiency, gated spectrometer for x-ray Thomson scattering experiments at the National Ignition Facility". In: *Review of Scientific Instruments* 87 (2016), 11E515.

[129] B. Bachmann et al. "Using penumbral imaging to measure micrometer size plasma hot spots in Gbar equation of state experiments on the National Ignition Facility". In: *Review of Scientific Instruments* 85 (2014), p. 11D614.

[130] B. Bachmann et al. "Resolving hot spot microstructure using x-ray penumbral imaging (invited)". In: *Review of Scientific Instruments* 87 (2016), 11E201.

[131] M. A. Barrios et al. "Backlighter development at the National Ignition Facility (NIF): Zinc to zirconium". In: *High Energ. Dens. Phys.* 9 (2013), pp. 626–634.

[132] J. R. P. Angel and M. C. Weisskopf. "Use of Highly Reflecting Crystals for Spectroscopy and Polarimetry in X-Ray Astronomy". In: *Astronom. J.* 75 (1970), p. 231.

[133] H. Legall et al. "High spectral resolution x-ray optics with highly oriented pyrolytic graphite". In: *Opt. Express* 14 (2006), pp. 4570–4576.

[134] A. Pak et al. "X-ray line measurements with high efficiency Bragg crystals". In: *Review of Scientific Instruments* 75 (2004), pp. 3747–3749.

[135] J. MacFarlane. "VISRAD- a 3-D view factor code and design tool for high energy density physics experiments". In: *J. Quant. Spectrosc. Radiat. Transfer* 81 (2003), p. 287.

[136] A. M. Saunders et al. "X-ray Thomson scattering measurements from hohlraum-driven spheres on the OMEGA laser". In: *Review of Scientific Instruments* 87 (2016), 11E724.

[137] John R. Taylor. *An Introduction to Error Analysis*. University Science Books, 1997.

[138] D. A. Chapman. "Probing the Dynamic Structure of Dense Matter Using X-Ray Scattering". PhD thesis. University of Warwick, 2015.

[139] K. Wünsch et al. "Structure of strongly coupled multicomponent plasmas". In: *Phys. Rev. E* 77 (2008), p. 056404.

[140] K. Wünsch et al. "X-ray scattering as a probe for warm dense mixtures and high-pressure miscibility". In: *EPL* 94 (2011), p. 25001.

[141] L. Pauling and J. Sherman. "Screening constants for many-electron atoms. The calculation and interpretation of x-ray term values and and the calculation of atomic scattering factors." In: *Zeitschr. Kristallogr.* 1 (1932), p. 81.

[142] W. R. Johnson, J. Nilsen, and K. T. Cheng. "Thomson scattering in the average atom approximation." In: *Phys. Rev. E* 86 (2012), p. 036410.

[143] M. S. Murillo et al. "Partial ionization in dense plasmas: Comparisons among average-atom density functional models". In: *Phys. Rev. E* 87 (2013), p. 063113.

[144] Evgenii N Avrorin, Vadim A Simonenko, and Leonid I Shibarshov. "Physics research during nuclear explosions". In: *Physics-Uspekhi* 49 (2006), p. 432.

[145] Evgenii N Avrorin et al. "Intense shock waves and extreme states of matter". In: *Physics-Uspekhi* 36 (1993), p. 337.

[146] Ryurik F Trunin. "Shock compressibility of condensed materials in strong shock waves generated by underground nuclear explosions". In: *Physics-Uspekhi* 37 (1994), p. 1123.

[147] Ken-ichi Kondo and Thomas J. Ahrens. "Shock compression of diamond crystal". In: *Geophysical Research Letters* 10 (), pp. 281–284.

[148] M. C. Gregor et al. "Hugoniot and release measurements in diamond shocked up to 26 Mbar". In: *Phys. Rev. B* 95 (2017), p. 144114.

[149] R. S. McWilliams et al. "Strength effects in diamond under shock compression from 0.1 to 1 TPa". In: *Phys. Rev. B* 81 (2010), p. 014111.

[150] D. Batani et al. "Hugoniot Data for Carbon at Megabar Pressures". In: *Phys. Rev. Lett.* 92 (2004), p. 065503.

[151] Stéphanie Brygoo et al. "Laser-shock compression of diamond and evidence of a negative-slope melting curve". In: *Nature Materials* 6 (2007), 274 EP.

[152] D. G. Hicks et al. "High-precision measurements of the diamond Hugoniot in and above the melt region". In: *Phys. Rev. B* 78 (2008), p. 174102.

[153] H. Nagao et al. "Hugoniot measurement of diamond under laser shock compression up to 2TPa". In: *Physics of Plasmas* 13 (2006), p. 052705.

[154] R. F. Smith et al. "Ramp compression of diamond to five terapascals". In: *Nature* 511 (2014), 330 EP.

[155] Shuai Zhang et al. "Path integral Monte Carlo simulations of dense carbon-hydrogen plasmas". In: *The Journal of Chemical Physics* 148 (2018), p. 102318.

[156] R. Nora et al. "Gigabar Spherical Shock General on the OMEGA Laser". In: *Phys. Rev. Lett.* 114 (2015), p. 045001.

[157] A. Morace et al. "Development of x-ray radiography for high energy density physics". In: *Physics of Plasmas* 21 (2014), p. 102712.

[158] J. D. Kilkenny et al. "A review of the ablative stabilization of the Rayleigh–Taylor instability in regimes relevant to inertial confinement fusion". In: *Physics of Plasmas* 1 (1994), pp. 1379–1389.

[159] F. J. Marshall et al. "Plasma-Density Determination from X-Ray Radiography of Laser-Driven Spherical Implosions". In: *Phys. Rev. Lett.* 102 (2009), p. 185004.

[160] N. R. Badnell et al. "Updated opacities from the Opacity Project". In: *Monthly Notices of the Royal Astronomical Society* 360 (2005), pp. 458–464.

[161] C. A. Iglesias and F. J. Rogers. "Updated Opal Opacities". In: *Astrophys. J.* 464 (1996), p. 943.

[162] D. Chapman et al. "Simulating x-ray Thomson scattering signals from high-density, millimeter-scale plasmas at the National Ignition Facility". In: *Phys. Plasmas* 21 (2014), p. 082709.

[163] T. Döppner et al. "Temperature measurement through detailed balance in x-ray Thomson scattering". In: *High Ener. Dens. Phys.* 5 (2009), pp. 182–186. ISSN: 1574-1818.

[164] T. Ma et al. "X-Ray Scattering Measurements of Strong Ion-Ion Correlations in Shock-Compressed Aluminum". In: *Phys. Rev. Lett.* 110 (2013), p. 065001.

[165] V. E. Fortov. *Extreme State of Matter on Earth and in the Cosmos*. Springer, 2011.

[166] R. Bredow et al. "Hypernetted Chain Calculations for Multi-Component and NonEquilibrium Plasmas". In: *Contrib. Plasma Phys.* 53 (May 2013), pp. 276–284.

[167] G. E. Engel and B. Farid. "Generalized plasmon-pole model and plasmon band structures of crystals". In: *Phys. Rev. B* 47 (1993), p. 15931.

[168] G. H. Miller, E. I. Moses, and C. R. West. "The National Ignition Facility: enabling fusion ignition for the 21st century". In: *Nucl. Fusion* 44 (2004), S228–S238.

[169] N. Bohr. "On the decrease of velocity of swiftly moving electrified particles in passing through matter". In: *Philos. Mag.* 30 (1915), p. 581.

[170] A. B. Zylstra et al. "Measurement of Charged-Particle Stopping in Warm Dense Plasma". In: *Phys. Rev. Lett.* 114 (2015), p. 215002.

[171] C. K. Li and R. D. Petrasso. "Charged-particle stopping powers in inertial confinement fusion plasmas". In: *Phys. Rev. Lett.* 70 (1993), p. 3059.

[172] J. A. Frenje et al. "Measurements of Ion Stopping Around the Bragg Peak in High-Energy-Density Plasmas". In: *Phys. Rev. Lett.* 115 (2015), p. 205001.

[173] F. Graziani et al. "Large-scale molecular dynamics simulations of dense plasmas: The Cimarron Project". In: *High Ener. Dens. Phys.* 8 (2012), pp. 105–131.

[174] P. Debye and E. Hückel. "The theory of electrolytes: I. lowering of freezing point and related phenomena". In: *Phys. Z* 24 (1923), pp. 185–206.